Band-Structure-Engineered Materials Synthesis

Nanocrystals and Hierarchical Superstructures

Current Status and Future Trend

S. Ahmad

KP Engineering College, Technical Campus, Agra, India

drsahmad@email.com

Abstract

Various aspects of preparing band-structure-engineered materials involving nanostructured building blocks are examined in this review. In continuation with enjoying great success in controlling the charge carrier transport propertiesof crystalline semiconductors, it was found better to choose a periodic structure comprising of monodisperse nanocrystals, where the adjustment of the wave function overlaps between nearest neighbors provided sufficient delocalization of the electron states necessary for charge carrier transport with adequate mobility. Of course, for maximum advantage from such a situation, it was necessary to employ monodisperse nanostructured building blocks with uniform inter-dot coupling, which turned out to be rather difficult to achieve in practice. For instance, nanocrystals size variations within 5% are currently considered monodisperse. For achieving higher degree of monodispersity, it is necessary to understand the phenomenon of nucleation and particle formation in more detail by examining the existing models and introducing more refinements, if possible. In case of adjusting inter-dot spacing, molecular linkers are adequately appropriate for this purpose. Moreover, the solution processing of nanostructured species possesses the unique feature of self-assembly, which is currently being explored for hierarchical superstructures ranging from nm to cm scales in dimension. This kind of material growth, being more close to biomimetic processes, when combined with conventional lithography and patterning, would certainly offer opportunities to use these hierarchical superstructures in numerous unprecedented applications.

Keywords

Energy Band Structure; Nanocrystals; Self-Assembly; Hierarchical Superstructures; Nanomaterials

Introduction

Theoretical study of size and shape dependent quantization of electron states in nanocrystals (NCs) [1,2]followed by the experimental verification of their associatedphysico-chemical properties [1,3], sets the ground for exploring their applications insynthesizing band-structure-engineered nanomaterialsin various forms including colloidal nanoclusters [4], close packed assemblies [5]), nanocrystals andtheir random dispersions in glass and polymeric matrices [6]; thin film coatings [7];2/3-dimensional periodic structures (superlattices) [8], and numerous other possiblehierarchical superstructures [1,9].In smaller nanoclusters, close-packed assemblies and nanocrystals, the electronic energy states resemble those of molecules defined in terms of highest occupied and lowest unoccupied molecular orbitals (HOMO and LUMO) separated by a finite band gap. In presence of significant wave-function, overlap between the nearest neighborof building block arising fromcloser proximities introducesextended electronic states causing collective behavior of electrons/holesthat are useful in realizing a whole variety ofnewer device applications.Hopping charge carrier transport is in general prevalent in random arrangements of the nanoclusters, close packed assemblies and nanocrystals embedded in a background matrix. For systematic exploration of their electronic properties on the same line as it has been possible in case of bulk crystalline materials, it is necessary to attachthe right kind ofmolecular linkers of uniform length to each of themonodisperse and well passivatednanocrystals,so that they try to self-assemble automatically, when dispersed in a suitable medium [1, 10,11]. In solution grown syntheses ofthesenanosize building blocks, eitherthey aresynthesized first and then passivated or made to undergo for simultaneous chemical reductionas well as surface passivationtogether. For linker applications, polymeric chain molecules are used, where not only precise length is possible to selectbut also choose right kind of chemical moietyhavingdifferent kinds of end radicalspossessingthe

2226-4523/16/01 001-34

doi:10.12783/ijmsci.2016.0601.01

required chemical affinity to the surface of the nanosize building blockdepending upon the specific requirement [1,10].

It has been a common observation that most of the nanostructured species try to self-assemble, when dispersed in a suitable medium andusing this characteristic feature of theirs, it has been possible to fabricate not only superlattices involving periodic arrangements but also an extremely large variety of hierarchical superstructures for further characterizations and applications [1,11]. It is significantly important to note that by choosing the right kind of surface passivation and attaching with proper length of inter-particle linkers, it has been possible to modify the process of electronic conduction in the resultant superlattice that changed its conductivity from that ofan insulator to that of a metal like state by adjusting the length of inter-particle molecular linkers [12]. Band structure engineering concept has not only been helpful in explaining the possibilities of such transitions but also indicated towards the possibility of intelligent material designs as examined from different angles in this review.

Having noted the importance of linkers in controlling the electronic conduction in NC-superlattices, it is equally feasible to explore using the capabilities of organic as well as inorganic polymersfor influencing the electronic conduction due to delocalization of electron states along with the interfaces present there between NCs and polymers in different possible forms [13]. In addition, there are numerous phytochemicals derived from the natural plants, which offer very attractive physico-chemical properties for considering themto modify the electronic and optoelectronic characteristics of NC superlattices in several ways[14,15]. This unique possibility of combining thegreen phytochemicals based surface passivation and functionalizations of NCs will ultimately result into a completely green design of NCs,their superlattices and hierarchical superstructures may open the opportunity of fabricating completely novelcategories of nanomaterials with altogether unique applications in diverse fields. How far it is possible to go in this direction of preparing green NCs, superlattices and hierarchical superstructures can be seen only after going through the developments already made in this context using conventional chemical species given below in brief.

Synthesis of Band-Structure-Engineered Nanosizebuilding Blocks

Electronic energy-band structure of a conventional crystalline material is in principle determined by the electronic structure of the constituent species, overlap between electronic wave functions of the two nearest neighboring units and the existing crystal symmetry [16]. For modifyingthe energy band-structure of any crystalline lattice, it is therefore necessary to have access to, if possible, independent control of all the three lattice parameters as mentioned above. However, in conventional crystallinesolids employing atomic species, there is neither any freedom to modify the electronegativity of the constituent atoms to change the strength of the inter-atomic interactions nor the crystal structures [17]. On the contrary, in NC based synthetic lattices, all these parameters are easilypossible to adjust providing a powerful tool to design the energy-band-structure of the synthetic lattice accordingly. The experimental observation of reversible metal-insulator transitions observed in case of a two-dimensional hexagonal superlattice of surface stabilized silver NCs, fabricated by Langmuir method, proved the viability of the band structure-engineering concept.The metal-insulator transition was possible to induce reversibly for an appropriate combination of electronic structure and inter-dot separation roughly adjustedby choosing appropriate surface passivating ligands followed by still finer adjustmentprovided by the compression of the monolayer during synthesis [17].

Surface functionalized metallic and semiconducting NCs with very weak inter-particle interactions have extensively been examinedfor preparing a variety of hierarchical structures. Better solubility of these NCs in organic solvents has been helpful in precipitating them size-selectively with better than 10% dispersion using solvent/antisolvent combinations [17]. The inter-particle interaction, in such cases,has been possible to controlwith the help of adjusting the particle size and the passivating ligand. For example,in case of smaller than 2 nm NCs, passivated with octadecane-thiol ligands,their overall aggregationis possible to decide by the existing ligand-ligand interactions. However, in case of larger than 3nm NCs, passivated by dodecanethiol,the process of aggregation primarily depends on the interactions between the metal cores,which increases with either increasing the core diameters or decreasing ligand lengths [17].

Besides surface passivation by organic ligands, as mentioned above, inherent structural stabilization arising due to their closely packed assemblyhas also been noted in a systematic study of n-alkylthiol(ate) stabilized Au NC synthesis.Significantly enhanced stability is observed in case of core masses of 15, 23 and 29x10^3AMUs, corresponding to compact metal NCs of 1.4 - 1.7 nm diameter with decahedral close-packed morphology during structural analyses. These small size monodisperse NCs synthesized and isolated help in verifying their physico-chemical characteristics in a precise manner [18]. This characteristic feature of closed packed structures of Au NCswas employed in having highly monodisperse samples for their characterization and further applications [5].

For synthesizing colloidal NCs, it is quite helpful to know about the process of nucleation and crystal growth in a saturated solution of the precursors maintained at an appropriate temperature. According to the classical theory of crystallization, the necessary conditions for producing monodisperse NC-colloids involve a process of faster nucleation followed by relatively slower growth on the existing nuclei [5]. This is possible to realize in practice by quickly adding the precursor solution to the reaction container to raise the concentration above the nucleation threshold to produce a burst of nuclei relieving the supersaturation. After this nucleation bursts, no new nuclei form as long as the consumption of feedstock during the slow growth of colloidal NCs does not exceed the rate of precursor in addition to the solution. The initial nuclei size distribution is determined by the time during which they are formed before starting to grow. In case the nuclei do not grow enough during the nucleation period as compared withtheir total growth subsequently, the resultant NCs are found more uniform in size [5].

In many cases, a second growth phase of Ostwald ripeninghas also been observed during which the high surface energy associated with the smaller size NCs promotes their dissolution, leading to re-deposition of the material on the larger NCs [5,19]. This phenomenon causes increase in size over time with a corresponding decrease in NC populations. Ostwald ripening has, thus, been used to simplify the size control of NCs. Even portions of the reaction mixture can be removed at certain times to modify the growth conditions for the desired changes [5].

Following the general guidelines regarding NC synthesis, described in brief above, it is in order to examine some specific examples of metallic and semiconducting NC-syntheses to illustrate the relevance of the basic concepts involved.

Widely used protocols for preparing gold NCs following as some variant of the basic citrate reduction method are studied long back [5, 20]. Most of the hydrophobic and hydrophilic nanocrystals are synthesized using borohydride reduction process in an organic solvent with thiol surface ligands using either one or two-stepprocedure [20]. In one of the recentlyreported one-stepmethods of preparing highly monodisperse Au NCs, an aqueous hydrogen tetrachloroaurate solution was mixed with freshly prepared sodium borohydride solution in the presence of a water-soluble alkyl thioether end-functionalized poly (methacrylic acid) stabilizer. The polymer concentration varied from 0.006 to 3.6 mM resulting in the particle sizes from 4.0 to 1.5 nm.The detailed analysis of these samples confirmed very narrow size distributions not observed earlier in the sub-5 nm size range. For example, the typical sizes measured were reported as 4.0 ± 0.1, 3 ± 0.1, 2 ± 0.2 and 1.5 ± 0.2, which are near-monodisperse [20].

While synthesizing semiconducting NCs, it is possible to initiate the processes of supersaturation resulting in a nucleation burst by rapidly adding the metal organic precursors into a vigorously stirred reaction container maintained at a constant temperature in the range of 150-350^{0}C. Common solvents used are mixtures of alkylphosphines, alkylphosphine oxides or alkylamines [5]. For example, in synthesizing chalcogenide NCs involving sulphides, selenides and tellurides of zinc, cadmium and mercury, precursors like dimethylcadmium, diethylcadmium, diethyl-zinc, and dibenzylmercury which provide cadmium, zinc and mercury components,respectively; whereas the corresponding sulphide, selenide and telluride components are taken care of by using organophosphine or bistrimethylsilyl-chalcogenides. Injection of reagents into hot alkylphosphites, alkylphosphates, pyridines, alkylamines, and furans are also used for producing NCs [5].

Some families of semiconducting NCs are currently attracting major attention because of their physico chemical properties that are highly relevant for biomedical applications [21]. For example, 1-10 nm NCsare excellent fluorescent labels with size tunable energy band gaps offering distinct advantages over fluorescent dyes. These

NC-labels are more stable during photo oxidation,exhibit continuous excitation spectra above the threshold of absorption together with a size selective strong, narrow, and symmetric emission peak, and allow simultaneous excitation of many colors by a single narrow-band excitation source. Easier synthesis of monodisperse NCs with characteristic emission properties using controlled growth conditions makes them exceptionally valuable in realizing light-emitting diodes and photovoltaics, besides their applications in biomolecular imaging [21].

Cadmium selenide (CdSe) is specificallyan excellentbio-label as compared withmany other semiconducting NCswith its emission peak possible to locate anywhere in the visible region, offering numerous applications ranging from solar-light sensitizers to multicolor fluorescent bio-markers. The commonest route for preparing CdSe NCs employs hot organic solvents based synthesis. Water-based synthesis has also been reported, offering a greener, simpler, faster, and often room-temperature method. However, the organometallic syntheses produce higher-quality NCs in terms of controlled dispersity, size, shape, and quantum yield of emission [22].

For preparing CdSe NCs, the most popular method involves the chemical reaction of $(CH_3)_2Cd$ with a selenium reagent in the presence of trioctylphosphine oxide (TOPO) surfactant at a temperature of 300°C. By controlling the reaction conditions, it is possible to prepare almost monodisperse (<5%) CdSe NCs in the range of 2.0 to 8.0 nm diameters [21]. However, the $(CH_3)_2Cd$ precursor is not preferred especially in large-scale syntheses because of itshighly toxic, pyrophoric, and explode nature at elevated temperatures. However, in a recent development, cadmium oxide (CdO) complexed with hexylphosphonic acid (HPA) or tetradecylphosphonic acid (TDPA)was reported as an alternative with more benign features in TOPO syntheses of CdS, CdSe and CdTe[21].

In another alternate approach, two solutions, out of which, one was prepared by dissolving cadmium acetate + oleic acid in a solvent under constant stirring followed by cooling, andthe other was prepared by ultrasonically dissolvingselenium powder in TOP, were further mixed with DMF/NMP/PE into a flask kept at 140°C under constant stirring [21]. For a desired size of the NCs, the reaction time was set somewhere in the range of 5-60 minutes, followed by rapid cooling, while still stirring to terminate the reaction. Finally, these NCs were allowed to precipitate by adding methanol and centrifuging followed by dispersing in organic solvents like *n*-hexane/chloroform/toluene for further storage. For aqueous phase hydrosol, the CdSe NCs stock solutions were mixed with aqueous TGA solution, and allowed to react for 8 hours under room temperature [21].

It is relevant to note from the above description that the different solvents possess different polarity, boiling point, and functional group; hence, affect the surface interactions between the solvents and the NCs differently affecting theirultimate sizes. In addition, the surface states of the NCs affect their optical properties. For instance, a long-chain fatty acid stabilizes and modifies through chelation between the carboxyl group and the surface of the NCs as well as the steric effect of the long aliphatic chain. Thus, using different solventsresults in different adsorption and desorption rates on the surfaces of the NCs, causing variations in their ultimate sizes as well as their characteristic properties [21].

In recent past, growing awareness of the environmental pollution concerns hasbeen encouraging various research groups to develop nanoparticles and nanocrystals synthesis protocols without using the organic solvents for controlling the resultant toxicity. In this context, supercritical fluid based processes offer better and greener options to design and prepare nanoparticles and nanocrystals without the limitations faced in the traditional methods in terms of unavoidable residual contaminations arising from the uses of toxic solvents [22-28]. Working on these lines of exploring the properties of supercritical fluids (SCFs) in the present context, two main procedures have been developed for nanoparticles and nanocrystals preparations using SCFs. The first one employs a rapid expansion of a supercritical solution (RESS) and the second one is some kind of an extension of the first one, where rapid expansion of a supercritical solution is put into liquid solvent (RESSLS). In a RESS process, especially the organic macromolecules are dissolved in an appropriate SCF solvent, and subsequently allowed to undergo a very rapid expansion through a nozzle spray into the ambient air. Well-dispersed particles are formed resulting from a homogeneous nucleation caused by the high supersaturation conditions combined with the rapid pressure reduction [29]. Generally, SC-CO_2 is used in majority of the cases, where the basic equipment comprises of a high-pressure stainless steel mixing cell, a syringe pump and a pre-expansion unit. In the actual process, the polymer is

first dissolved in a CO_2 solution at ambient temperature in the mixing cell. Subsequently, the solution is allowed to move in the pre-expansion unit with the help of the syringe pump and is isobarically heated to the pre-expansion temperature until it expands through the nozzle at ambient pressure. Using this procedure,poly(hepta-deca-fluoro-decyl-acrylate) and poly(L-lactic acid) nanoparticles were prepared, wherein, factors like concentration and degree of saturation of the polymer, the processing conditions, the molecular mass and the melting point of the polymer were noted to be important to know for their influences for better control of the final product [30,31]. Although the method did perform without organic solvents and produced a majority of nano-sized particles, but the main drawback was the generation of micron sized particles or agglomerates as well, which was due to severe aggregation involved during the jet spray.

In order to overcome the problem of agglomeration encountered in RESS process mentioned above, another process was developed, where the supercritical solution was made to expand into a liquid solvent instead of ambient air [32]. This liquid solvent used in this methodwas found effective in suppressing the agglomeration of primary NPs. For instance, in case of synthesizing poly(heptadecafluorodecylacrylate) (PHDFDA)NPs,the supercritical solution expanded and precipitated the polymer in water as the solvent [33]. It was further shown in this study that the particle formationsbasically resulted from the aggregation of initially formed nanoparticles. In addition, the presence of NaCl in the water phase helped in stabilizing the NPs due to an increase in the ionic strength. Poly(methylmethacrylate) (PMMA) and poly(L-lactic acid) nanomaterials were also synthesized by this method using a CO_2-cosolvent as the supercritical fluid. Using a co-solvent alloweda better dissolution of the polymers in the supercritical solution and the presence of NaCl in the water solution generated only NPs [33]. Despite the availability of a number of fluids like carbon dioxide, n-pentane, ammonia and many others, the poor solubility of polymers in these SCFs remains a major weakness of this process.

Alternately,spray-drying process was also used for the past several years for the preparation of micron-sized organic particles or to convert NP suspensions in dry powder mainly for biomedical and pharmaceutical applications especially with reference to drug delivery [34-36]. A typical spray-drying consists of first atomizing a liquid into a spray of fine droplets, which is subsequently brought in contact with a hot gas to remove the moisture and help in forming the solid product that is further recovered via a cyclone unit. Spray-drying technology after passing through continuous improvements in the recent past has been able to produce polymeric NPs in one-step from a polymer solution. For example, NPs of Arabic gum, whey protein, polyvinyl alcohol, modified starch and maltodextrin wereprepared successfully using a ''nano spray dryer'' [37].

Another similar technique was extended to produce bovine serum albumin nanoparticles, where the ''nano spray dryer'' was modified to a vibrating mesh spray technology creating still finer droplets. The generation of droplets was primarily based on using a 60 KHz piezoelectric actuator fed perforated membrane with micron-sized holes, varying from 4 to 7 μm in diameter. The membrane vibration caused ejection of millions of nanodroplets each second with a very narrow size distribution. The final sizes and their standard deviations of the NPs were found to depend on several parameters like the nature and concentration of the polymer, the spray mesh size, the operating conditions including drying temperature, feed rate, drying gas flow rate, and the concentration of the surfactant, in case used in the formulation. Finally, the main advantage of this novel technology was very high yield of NPs production in 70–95 % range [15].

Besides conducting experiments for improving upon the control of NC size and dispersity, attempts were also made to develop novel methods of synthesizing these fundamental building blocks for preparing unique meso-materials as reported in the following by taking few typical examples to illustrate such unprecedented possibilities of material synthesis.

In one example, an in situ synthesis was reported for synthesizingmonodisperse PbS NCs on the sites of Pb^{2+} ions loaded in nanoporous SnO_2 thin film employing an oil phase source of S^{2-}ions.Immersion of Pb^{2+} ions loaded SnO_2 thin film in an aqueous phase causedthe transfer of S^{2-} ions through oil/water interfaces. The diffusion of Pb^{2+} ions across the oil phase comprising of different ratios of ethylene glycol and water ultimately controlled the particle sizes and their dispersions. Such SnO_2 thin films loaded with PbS NCs were used in fabricating NC-

sensitized solar cells exhibiting PCE of 1.05% under standard illumination demonstrating the viability of an environment-friendly approach of fabricating monodisperse PbS NCs on the nanoporous SnO_2 thin films [38].

A recent reportdescribed the encapsulation of NCs appropriate for bio labeling and imaging into 100 nm spherical and monodisperse chitosan NPs exhibiting more than 10% higher quantum yield of fluorescence than bare NCs. It also offered the additional possibility of bio-conjugation through amines and hydroxyl groups present on the surface of chitosan NPs for their targeted delivery in case needed [39].

Microwave assisted green synthesis of monodisperse CdSe NCs over coated with $Cd_{0.5}Zn_{0.5}S$/ZnS multi-shells exhibiting narrow photoluminescence bandwidth and 80% quantum yield was reported recently. These CdSe/$Cd_{0.5}Zn_{0.5}S$/ZnS core/multi shell NCs were found very useful in labeling and imaging of breast cancer cells [40].

In another green synthesis of highly crystalline monodisperse, colloidal PbS NCs with controllable sizes and narrow dispersions werereportedusing laser irradiation of a suspension of larger size polydisperse PbS NCs. These colloidal NCs exhibited size-tunable near-infrared photoluminescence, and self-assembled into well-ordered two-dimensional or three-dimensional superlattices due to the small degree of poly dispersity and surface capping of 1-dodecanethiol [41].

A rational design of NC synthesis protocol was reported for optimizing the reaction parameters followed by the application of the optimized procedure to produce gram scale material, maintaining monodispersity and maximum reaction yield by adapting a Taguchi table based procedure. In this approach, the number of experiments required for optimization was reduced significantly compared with the trial-and-error methods. Using 2-L reactor with a peristaltic pump, 2-3 g samples of different size CdSe NCs were produced with narrow size distribution. Extending a similar approach for gram-scale synthesis of CdSe/CdS/ZnS core/shell/shell NCs exhibited a fluorescence quantum yield of 81% with excellently resistant photoluminescence in presence of a quencher [42].

For optimal utilization of band-structure-engineered features of nanosize building blocks in synthesizing a whole variety of meso-structures, it is necessary to look into the experimental results reportedon hierarchical structures synthesized having dimensions starting from nm and going up to cm-scales. Incidentally, the characteristic features of self-assembly associated with nanostructured entities have been found very helpful in this context. Thus, templates assisted growth combined with self-assembly are found to produce superstructures involving large range of dimensionalvariations mentioned above. Some of these results reported recently, are included in the followings to highlight the difference between nanocrystalsgrowths as comparedwith the conventional bulk monocrystalline growths experienced in case of classical condensed state materials.

Incorporating structural hierarchy into nanostructures is of great practical relevance as a result of enhanced mass transport, reduced resistance to diffusion, and high surface areas for adsorption and reaction. The general strategies for the synthesis of hierarchical structures assembled from nanosize building blocks were reviewed in a recent publication. The well-defined hierarchical structures are noted to provide new opportunities for optimizing, tuning, and/or enhancing the properties and performance of these materials and have found applications in photo-degradation, photo-catalytic H_2 production, photo-catalytic CO_2conversion, and sensitized solar cells with added advantages [11].

Hierarchically organized ZnO nanocrystals are currently being seriously examined for their potential applications in fabricating nano detectors, optoelectronic, vacuum microelectronic, and spintronic nano devices. The realization of novel nanostructures including arrays of nano candles, wine-bottle-shaped nanorods, nano-rivets, periodic diamond-string and needle like configurations, nano-fern and needles, tooth-shaped nano- belt, spinal-shaped nanostructures and bamboo-shaped nano-rodsemploying atmosphere pressure physical vapor deposition was reported sometime back. The unique feature of this method lies in using atmospheric pressure phenomenon to induce chaos and fluctuation of source vapor facilitating multiple growth mechanisms to have competing dominating effects on the crystal growth of ZnO structures, possessing satisfactory structural and optical qualities

[43].

Though, block copolymers have been known since long for their uses in preparing nanoporous inorganic material, but the process involved has a serious limitation that the materials deposited are generally amorphous in nature and it is not possible to transform them into crystalline form without disturbing their structural porosity. This serious limitation was overcome by using charge-stabilized colloidsafter stripping the organic ligands from their surfaces. Subjecting this kind of NC-colloids to evaporation-induced co-assembly with di-block copolymers enabled the formation of a nanocomposite, which after thermal degradation, resulted into a NC-based mesoporous structure. The mesoporous material prepared by this general method, equally applicable to a large number of other families of NCs and copolymer combinations as well, possesses homogenously disordered porosity, which is possible to modify by selecting the copolymer combinations finding numerous useful applications [44].

It is significantly relevant to explore preparing nanowires and nanotubes arrays patterned on multiple length scales for their applications in integrated electronic and photonic devices. In a recent publication, an efficient solution-based method was reported for controlled hierarchical organization of nanowire-based structures over large areas. In this method, nanowires are aligned in the Langmuir−Blodgett trough with features varying from nanometer to micrometer scales and layer by layer transferred to a substrate with various combinations of parallel and crossed nanowire structures. Further, using conventional photolithography, it is possible to pattern the parallel and crossed nanowires based structures into repeated arrays of controlled dimensions to produce hierarchical structures with dimensions varying from nanometer to centimeter length scales. Detailed study of the electrical transport exhibited the feasibility of reliable electrical contacts prepared by this method. This solution-based bottom-up assembly process provides a highly flexible method for preparing hierarchically integrated nano devices needed for a broad range of system applications in future [45].

Hierarchical assembly of hollow microstructures was reported in another paper describing one-pot synthesis of Cu_2O microspheres with multilayered and porous shells, which were organized by NCs. In this process, hollow microspheres of $Cu_2(OH)_3NO_3$ were first formed by Ostwald ripening and then reduced by glutamic acid. The Cu_2O NCs were deposited on the hollow intermediate microspheres and organized into finally multi-shell structures. The Cu_2O microspheres prepared by this method were put into use in fabricating a gas sensor, which showed much higher sensitivity than solid Cu_2O microspheres [46].

Self-assembly of monodisperse colloidal octapod-shaped nanocrystals was realized in a solution involving two distinct phases. In phase I, the linear chains of octapods were formed in interlinked manner. Subsequently, in phase II, the chains spontaneously self-assembled into three-dimensional super-structures primarily were decided by the octapod shapes. The mechanical strength of these superstructures was improved by welding the constituent nanocrystals together [47].

Monocrystalline rutile TiO_2 nanorods were grown on electro spun polycrystalline anatase TiO_2 nanofibers using a surfactant free hydrothermal growth route. Spectroscopic measurements confirmed better dye-loading capability resulting in enhanced light harvesting in a dye sensitized solar cell, where dye molecules sandwiched between semiconducting TiO_2 and hole- transporting layer of spiro-OMeTAD enhanced the open circuit voltage (V_{OC}). Because of improved light harvesting, dye loading, and reduced recombination losses, the hierarchical nanofibers exhibited 2.14% conversion efficiency, which was 50% higher than the efficiency obtained by plain nanofibers [48].

Wurtzite ZnS based hierarchical structures like branched flowers were assembled from nanosheets and nanorods, using a template-less and low-temperature solution route. The growth of wurtzite ZnS nanostructures at 4^0C without any organic additives was realized by the slow reaction between $Zn(NH_3)_4^{2+}$ and thioacetamide in aqueous $(NH_4)_2SO_4$–NH_4OH solutions. Branched ZnS flowers were realized from 6-10 nm nanosheets at 4^0C, and fluffy ZnS spheres comprising of radially oriented nanorods were fabricated at 60^0C. Prolonged ageing of the fluffy spheres at 60^0C resulted in the formation of unique fluffy hollow ZnS spheres through Ostwald ripening [49].

Thiol radical containing glutathione combined with a lead-ion source was used for synthesizing hierarchical PbS structures using hydrothermal route producing flower-shaped microcrystals, submicron-sized spherical particles

and dendritic PbS by adjusting pH of the solutions, in which, glutathione acted as template as well as sulfur source. A pesticide biosensor fabricated using AChE-CHIT/dendritic PbS/GCE exhibited a linear response over the concentration range of 0.05 μM to1.0 μM with a detection limit of 0.02 μM [50].

Pt-Cu superstructures, comprising of highly branched and dendritic tetragonal nanostructures, were reported using a facile template-free hydrothermal route. These hierarchical superstructures exhibited comparatively better electrocatalytic properties compared withcommercially available Pt/C and Pt black because of their interconnected arms, sufficient absorption sites, and larger area exposed surfaces for the purpose of electro-oxidation of methanol and ethanol [51].

Optical Properties NCs

Before deploying metallic and semiconducting NCs in specific applications based on their physicochemical properties, it is better to characterize them by measuring and analyzing their optical absorption spectra, which will definitely help in understanding various types of optical transitions involved according to their electron energy states at atomic levels.

The general nature of optical absorption in most of the metal NCs has been assigned to a strong broadband absorption arising due to collective oscillation of the electrons known as surface plasmon resonance. Though, according to the earlier theory, this optical absorption should be size independent having a constant absorption bandwidth and position for all metal NPs having diameters smaller than certain limiting value but experimentally a clear shift of the absorption band to lower energy with wider bandwidth was invariably observed with reduction in size. More refined considerations including the free electron scattering with surface were found better to explain the spectra of Au NPs larger than 3 nm but failed in case of smaller size NPs due to still some more invalid assumptions. However, most of these problems which encountered in explaining the optical spectra of smaller size Au NPs were over with the availability of alkyl-thiolate (SR) stabilized Au NPs, wherein it was possible to have uniform surface protection without modification of structural and electronic properties. For example, n-alkyl-thiolates (SR) and their derivatives were observed to form thiolates or dialkyldisulfides (RSSR) monolayers attached to Au surfaces in a reversible manner [52].

Following SR/RSSR passivation routes, it became possible to prepare Au NPs in the range of 1.4-3.5 nm as charge-neutral entities comprising of a crystalline core of close-packed metal atoms and a dense mantle of straight-chain groups. Methyl group terminated surfactant molecules present on Au NP surfaces made these NPs highly stabilized resulting in very weak interacting with solvents, strong acids, or bases as well as with each other. Further observation of mass spectra peaks corresponding to some typical magic numbers clearly indicated the validity of filled structural shells of Au-atoms. Considerable insight into the structure of these NPs and their interactions wasobtainedfrom the comparison of simulation and actual measurement of X-ray diffraction patterns that matched with the calculated patterns from theoretically assumed structures [18, 52].

Out of a number of chalcogenides examined, PbSe attractedspecial considerationsdue to its relevance in optoelectronic devices as it not only possesses valence and conduction band maximum/minimum coinciding at the same L-point in the Brillouin zone but also has very light charge carriers possessing very high mobilities. Further, the confinement of charge carriers is fairly strong in PbSe NCs as the exciton Bohr radius in bulk is around 46 nm. It is also possible to tune the energy band gap from 0.3 eV up to 1.1 eV in PbSe NCs by changing their diameters. Because of these features, PbSe based NCs show great promise as building blocks for a wide range of band-structure-engineered materials for their optoelectronic applications in the near infrared region. For instance, PbSe NCs are currently being explored for higher efficiency PVSCs because of multiple exciton generation (MEG) observed recently [53].

In order to verify these attractive features of PbSe NCs, optical absorption was studied in detail by comparing the experimental observations with the theoretical models in highly monodisperse nanocrystals synthesized for this purpose. The analysis of size dependent transition energies measured for NCs ranging from 3.4 to 10.9nm helped in identifying higher and lower energy optical transitions at a different point in the Brillouin zone under effective

mass approximation. The measured spectra of these PbSe NCs exhibited sharp peaks due to distinct optical transitions and the plots of the corresponding transition energies as a function of NC diameter (d) showed a variation of ~$d^{-1.5}$ for the lower energy transitions extrapolating to 0.3 eV, which coincided with the L-point band gap of the bulk PbSe. Similarly, high-energy transitions extrapolated to 1.6 eV coincided with S-point band gap of the bulk PbSe [53].

Surface Functionalization

Keeping in view the structure and physico-chemical properties of NCs, it is anticipated that just synthesized bare nanoparticles would be highly unstable due to enhanced chemical reactivity of the atomic species residing on the surface that are immediately exposed to the solvent in the dispersion medium employed in their preparations. The morphology and the size of such NCs during synthesis are dynamically varying features decided by the two ongoing competing processes namely - arrival and departure of the active species on the surface of the nanocrystals due to the relatively favorable conditions for growth and dissolution of the deposited species arising out of interaction with the solvent medium occurring simultaneously. NC surface stabilization should, therefore, be intentionally introduced to affect desirable changes at different stages of the synthesis like nucleation, growth and storage. Such stabilizing modifications are bound to influence the overall growth and stability of the NCs against aggregations in aqueous and non-aqueous media besides creating additional sites that are appropriate for functionalizations for chemical conjugations at later stages. Inter-particle repulsions, arising out of electrostatic charges; steric exclusion and hydration layers;are primarily responsible for arresting continuous growth of particle size caused by aggregation in general [54].

Surface Stabilization

There are a number of methods alreadyin use for achieving a reasonable level of surface stabilization in NCs [55-57]. It is possible to attach appropriate types of molecular ligands capable of providing stabilization involving processes like chemisorption; electrostatic attraction due to oppositely charged species, or hydrophobic features acquired from head-group of the ligands. Alternately, functional groups that possess some significant affinity to the inorganic NC surfaces may also be added during synthesis itself for adequate stability. The nanocrystals having polar, nonpolar - particularly hydrocarbon chains and charged ligands on their surface, are known to dissolve easily in polar, nonpolar especially organic solvents like hexane, toluene and chloroform and aqueous solvents, respectively. Similarly, the presence of amphiphilic ligands including polyethylene glycol on the NC surface makes them soluble in a number of solvents with intermediate polarity. In another option, it is preferred to cover the NC surface by a hydrophobic ligand to prevent aggregation leading to enhance stabilization. It is also useful to know that bond forming processes are there between inorganic nanocrystals and an electron-donating end-group of a ligand like thiol, amine or phosphine, undergo dynamic attachment and detachment processes. Though, this dynamic process permits ligands removal by excessive washing or mass action by another type of incoming ligands, but otherwise, it adversely affects the NC stability due to increased possibility of aggregation and precipitation. It has also been observed that optical irradiation of the fluorescent NCscausedsurface oxidation leading to desorption of stabilizing ligands that ultimately enhance aggregation. Depending upon the basic requirement of stability enforced by the targeted application of the nanocrystals, any one of the schemes or a combination of few from those listed above can be implemented and the protocolprovided is not too difficult to be implemented besides cost[55-57].

It will be useful to examine in brief the practical implementations of different propositions for improving the NC stability in aqueous and organic media as described below.

1) NCs in Aqueous Solutions

Hydrophilic NCs are fairly stable in aqueous solutions, where electrostatic repulsion is created by equally charged ligands on their surfaces. However, the electric field responsible for such mutual repulsions gets shielded in the presence of higher salt concentrations and as a result, these NCs start moving closer until the attractive forces due to induced dipole interactions in form of van der Waal force or hydrogen bonds, finally

step in and encourage them to aggregate. Further, the solution pH may also affect the NCs to lose or change the sign of their charges leading to reduction in stability due to induced agglomerations. The stability of Au-NCs prepared by citrate reduction is an example, where negatively charged citrate ions adsorbed on the surfaces provide adequate repulsions. Though, such colloids are stable for years, but it is rather difficult to concentrate and aggregate them irreversibly in the presence of salts. However, it was subsequently shown that the replacement of citrate layer by sulphonated phosphines, mercapto-carboxylic acids, mercapto-acetic acid (MAA), and mercaptoundecanoic acid (MUA) ligands provides relatively stronger bonding. For example, it was found feasible to increase the NC-concentration in presence of the phosphine layers and make them precipitate the phosphine-coated NCs by salt-induced aggregation and dissolve them again as single particles in low-salt buffers. Thiol ligands exchange with phosphines is very often used for attaching thiol-modified DNA to NCs [56].

2) NCs in Organic Solutions

A practical situation of Au-NCs in organic solvent uses tetraoctylammonium bromide and dodecanethiol as stabilizing and size controlling ligands in Brust synthesis. In addition, quaternary ammonium ions are also used for capping separately. For changing nanocrystals surface properties and their functionalization, dodecanethiol ligands are substituted by a variety of other ligands. For instance, chemisorbed thiol-ligands show the highest affinity to noble metal surfaces, particularly to Au. However, in some other experiments, the same was identified as covalent bond. The exact process involved and the bond nature - both are still not clearly understood. This may be quite possible that varying affinities associated with crystal facets, edges, terraces and vertices on the NC surfaces play a significant role in making situation quite complex during ligand shell formations. Besides, the ligands that are prone to surface migrations after their attachment may cause still more complications. Trioctylphosphine (TOP) and its oxide TOPO that binds preferentially to Cd and Zn atoms have been successfully employed in CdSe and CdSe/ZnS QD stabilization. In addition, hexadecylamine and other amines were also found as useful ligands for CdSe quantum dots that were, later on, replaced by one or more thiol-groups. However, it is important to know that the ligand shell may influence the quantum yield of fluorescent quantum dots. Recent experiments using dendrimers and thiol-containing peptides for Au nanocrystals and protein binding to quantum dots by replacing MAA on the surface have opened newer ways for nanocrystal stabilizations [56].

Phase Transfer – From Aqueous to Organic and Reverse

In some applications of NCs that are synthesized in organic solvents, it may be necessary to transfer theminto aqueous medium to make them compatible with biological systems or it may be just the reverse in some other applications. In such cases, phase transfer process becomes handy especially in case the desired NCs are not possible to synthesize with the corresponding ligands on their surfaces. For phase transfer in both the directions, three strategies are there involving - ligand exchange, ligand modification and preparing additional layer of molecules that stabilize the NCs in the final phase. In addition, silanization is also used for surface modification and phase transfer, representing a case in-between [56].

In ligand-exchange, the stabilizing molecules are replaced by stronger binding ligands that are transferred to the second phase and provide stability by converting hydrophobic to hydrophilic ligands. For example, in case of TOP/TOPO-coated CdSe/ZnS NCs, their replacement by phosphine-based ligands with a hydrophilic thiol group like mercaptocarboxylic acids – (MPA and MUA) converted them into aqueous phase. Sometimes, a mixture of different ligands is preferred to introduce additional functional groups to the nanocrystals surface as well. The hydrophobic ligands on NCs are known to provide adequate stability in organic solvents. A similar situation can be created during replacement, where a strong binding ligand is chosen to have hydrophobic free ends. This kind of phase transfer is possible with linear hydrocarbons having a single thiol or amino-group or molecules with more than one hydrocarbon chains and also with multiple anchor groups such as dihydrolipoic acid and other ligands [56].

Though, transfer of NCs from aqueous to organic phase is generally difficult because the organic phases are poorly soluble in aqueous ones,but mercaptocarboxylic acids that are used to stabilize NCs in aqueous phase are readily

soluble in organic solvents like toluene and tetrahydrofuran. Therefore, in such cases, the transfer from organic to aqueous phase occurs spontaneously. Moreover,ligand exchange protocols with amphiphilic molecules have also been reported that allow the dissolution of the same NCs in both polar and nonpolar solvents [56].

Polyethylene imine and polyacrylic acid have been used to change ligand orientations, where positive or negative charged moieties can be boundto the inorganic NCs and change the same to polar form. Similarly, hydrophobic NCs have been transferred to the organic phase by introducing polyelectrolytes stabilized by electrostatic repulsion or ligand exchange with a PEI–PEG copolymer [56].

Ligand modification was also used for phase transfer, wherein the stabilizing ligand in the original phase was rendered hydrophilic or hydrophobic to facilitate the transfer in the second phase. For example, mercaptocarboxylic acid stabilized hydrophilic NCs were modified to a hydrophobic form that was bound to its carboxylic groups like dicyclohexylamine to MAA. Changing polarity by stripping off cyclodextrin rings and complexing with octadecanethiol or by cyclodextrin complexing with oleic acid present on the NC surface or by covalent attachment of amphiphilic ligand were some of the methods explored in this context [56].

The third strategy for phase transfer involves coating of an additional molecular layer on the NCs that adsorbs on the original ligands and changes the surface properties as required. In this scheme, a ligand bilayer is formed that allows transferring hydrophilic entities from aqueous phase to organic one and hydrophobic-NCs to water. Quaternary ammonium salts are very effective surfactants for the transfer from aqueous to organic phase. Such additional layers may be used in preventing sensitive core materials from oxidation. Owing to the additional layer bound by hydrophobic interactions, this coating strategy is possible to useirrespective of the inorganic NC core. Variations may include the embedding of hydrophobic-NCs into the lipid bilayer of vesicles and liposomes and paramagnetic lipids that yield fluorescent nanocrystals with additional magnetic properties [56].

Surface Modifications

On the basis of detailed experimental investigations, the NC assemblies are found to be far more complex with attributes that are entirely different from the features derived from simpler theoretical models studied in this context. The discrepancies arepossibly due to the actual nature of the NCs that are not rigid spheres besides having a soft organic ligand shell that may possess completely different charge distributions. It is quite likely that such heterogeneous charge distributions may create some significant numbers of hydrophobic patches on the surface or the ligand shell may undergo changes affected by other external factors. For example, NC-bridging by electrostatic attraction caused due to multi-valent and oppositely charged ions or polyelectrolytes may aggravate agglomerations significantly. It is further proven experimentally that strong binding ligands form a denser layer that stabilizes NCs better than weak binding ligands. In aqueous solutions, charged ligands, having carboxylic or sulphonic acid groups, stabilize the NCs for longer durations and even in presence of higher salt concentrations. Ligands providing steric stabilization are more resistant to high salt concentrations than electrostatically stabilized NCs [56].

Polymer Coated Phase Transfers

There are a number of variants of phase transfer protocols using ligand exchange but this approach still suffers from several drawbacks including desorption of smaller ligands with one head group that can impair the particle stabilization, especially, where excess free unbound ligands are lacking and the specific influence of the core materials on thiol ligands shows relatively stronger bonding to various metal nanoparticles and NCs.

In contrast, coating of an additional amphiphilic layer that adsorbs by hydrophobic interaction to the hydrophobic ligands of the nanocrystals has the advantage that it is independent of the inorganic core and even the exact type of ligands since the adsorption is predominantly based on hydrophobic interaction of hydrocarbon chains and van der Waals forces between the molecules. In case of amphiphilic polymers, many contact points between the ligand molecules and the polymer prevent facile desorption of the polymer molecule from the nanocrystals by thermal fluctuations. These coated nanocrystals have therefore the same physical and chemical surface properties independent of their core. One common example includes a polyacrylic acid-based polymer with hydrophobic side

chains, where its carboxylic groups are modified with aliphatic amines via an amide bond. This comb-like polymer is soluble in organic solvent and can be attached to the hydrophobic nanocrystals with TOP/TOPO ligands. After evaporation of the solvent, the solid can be dissolved in an aqueous buffer, yielding stable, single nanocrystals. Similar kinds of polymers were employed to disperse quantum dots in ethanol [56].

CdTe/CdSe quantum dots were prepared in presence of polyacrylic acid with dodecylamine modification, yielding amphiphilic nanocrystals that were soluble in a number of organic solvents and in water. Another class of amphiphilic polymers was synthesized by co-polymerization of maleic anhydride with olefins, resulting in alternating copolymers. The maleic anhydride rings hydrolyze and open, forming two carboxylic groups each as soon as come into contact with water. Compared withmodified polyacrylic acid, the hydrophobic side chains are not randomly grafted and the density of carboxylic groups is higher [56].

Another amphiphilic polymer design was reported recently by combining the advantage of maleic anhydride moieties for pre-modification and custom modification with side chains. Hydrophobic side chains, consisting of dodecylamine, are grafted to a polymaleic anhydride backbone, leaving a part of the anhydride rings intact. In case needed, additional functional molecules like fluorescent dyes, sugars, biotin or PEG can be covalently grafted to the polymer. These comb-like amphiphilic polymers used in nanocrystals synthesis are made up of alternating or random sequence of building blocks of aliphatic chains as hydrophobic elements and charged groups as hydrophilic. Hydrophobic side chains intercalate the hydrophobic ligand molecules of the nanocrystals, while the hydrophilic part is exposed to the outside aqueous environment. Even though the attraction between the polymer and the particle is due to rather weak van der Waals force between the aliphatic chains, the hydrophobic interaction and the large number of contact points by the several side chains of the polymer result in a very stable coating. Owing to the nature of the interaction,this coating approach works in principle for any hydrophobic nanocrystals, regardless of the inorganic core material [56].

A variety of polymers are coated on the nanocrystals by direct binding to the inorganic particle surface: hydrophilic and hydrophobic oligomers with phosphine anchor groups and a PEG-modified polymer with phosphine oxide that can be used for phase transfer of different cores to an aqueous solution. Alternative to coating particles with amphiphilic or other polymers, nanocrystals with a polymer shell can be prepared by lateral crosslinking or polymerization of the small ligand shell or in an alternative approach by growing a polymer off the particle surface from the attached ligands [56].

Block copolymers constitute another class of appropriate amphiphilic polymers that are used for coating of nanocrystals comprising of hydrophobic and hydrophilic parts[56]. These polymers form micellar structures with their hydrophilic or hydrophobic part inside, in contrast to the respective solvent in which they are dispersed. Such structures are used for preparing nanocrystals, coating and phase transfer. Certain copolymers have also been laterally cross-linked. The thickness of the polymer shell can be adjusted by using polymers with appropriate block lengths.

Nanocrystals with different core have been modified with a silica shell - an inorganic polymer where using ligand exchange protocol, a first layer of silanes is attached to the nanoparticle surface. Next, using the first layer, a polymeric, cross-linked inorganic silica shell is deposited on the nanocrystals, which can be further modified. Nanocrystals of different materials including noble metals like Au, Ag; fluorescent CdSe/ZnS; phosphorescent and magnetic Fe, Co and $CoFe_2O_4$; and of different morphologies have been successfully coated with silica shells.

It has also been observed that ligand based nanocrystal functionalization primarily depends on the ligand shell or surface coating, not on the actual inorganic core. Therefore, common functionalization routes,having been developed so far, are easily extended to all types of nanocrystals; QDs, magnetic nanocrystals and silica nanoparticles provided the nanocrystals which are stable under the reaction condition and purification[56].

The number of functional groups per nanocrystal is only a few and therefore difficult to access by any analytical method as the nanocrystal surface is predominantly covered by ligands. For numerous applications, monovalent nanocrystals or nanocrystals with a defined number of functional groups are needed for which some efforts were

made in recent past. Here, the main problem is due to competing processes of conjugations at equivalent sites available on the surface facets. Introducing stoichiometric control by adjusting the experimental conditions such that only a fraction of nanocrystals reacts to a certain group of molecules with desired function, leaving the other nanocrystals unmodified which is one possibility. Finally, these modified nanocrystals are to be separated from the rest. This method was demonstrated in case ofAu-nanocrystal functionalization with peptide where functionalized particles were immobilized on an affinity column by an oligohistidine domain present in the peptide. Later on, adding imidazole particles modified with a single peptide with a single amino group at its terminal end eluted such immobilized particles [56].

Phytochemical Stabilizations

While discussing about the applications of phytochemicals in stabilizing nanoparticles and nanocrystals, chitosan is one example often referred to in this context.Chitosan of chitin family without N-acetyl groups possesses improved solubility and primary amines present therein help in immobilizing the metal nanocrystals. For instance, carboxymethyl chitosan (CMC) has been considered as a good matrix for Pt, Au and Ag nanocrystals [58]. Chitosan-stabilized Au nanocrystals, as reported in many publications, acquire morphologies and size distribution based on the chitosan and precursor concentrations. The electrostatic attraction between the positively charged chitosan amino groups and the negatively charged $AuCl_4^-$ ions drives the nanocrystal formation leading to higher stability [59,60].

Polysaccharides form another useful group of phytochemicals that are very effective in reducing salts into metallic nanocrystals due to the oxidation of hydroxyl and introduction of amino groups by hemiacetal reducing end present there [61]. Such amino-groups facilitate complex formation and stabilizing the metal nanocrystals as they bind to them and make a hydrophilic surface [62,63]. For instance, polysaccharide heparin, when modified to 2,6-diaminopyridinyl heparin (DAPHP), serves as reducing and stabilizing agent because of stronger binding with Ag and Au nanocrystals [63]. A narrow size distribution of 10 ± 3 nm and 7 ± 3 nm for Au and Ag-DAPHP conjugates were realized primarily due to the tight binding of the diaminopyridine moiety of DAPHP to the surface of the nanocrystals. Heparin - without reducing end modification was used for preparing Ag nanocrystals using thermal treatment at 70^0C where heparin and Ag^+ ion concentrations decided the morphology and size distribution. The nanocrystal size increased while shifting the surface plasmon resonance (SPR) towards red-end with increasing concentrations of heparin and Ag^+ ions [58]. Hyaluronic acid (HA) has been used for synthesizing 5-30 nm Au and Ag nanocrystals by thermal treatment where HA acted as reducing and stabilizing agent. These HA composites have a larger particle size distribution than Au-DAPHP and Ag-DAPHP nanocrystals [63].

Nanoporous cellulose gels were prepared from an aqueous alkali hydroxide-urea solution, when immersed in precursor salt solutions like $AgNO_3$, $HAuCl_4.3H_2O$ or $PtCl_4$ resulting in synthesis of metal nanocrystals. These metal nanocrystals carrying gels are converted into very effective nano-catalyst when dried by supercritical CO_2 that imparts higher transmittance, porosity, surface area along with moderate thermal stability and good mechanical strength [64].

In another example, glucose reduced and starch stabilized Ag nanocrystals were prepared by incubating Ag salt with starch and glucose at 40^0C for 20 hours wherefrom a mean size of 5.3 nm nanocrystals demonstrated a solution stability of more than 2 months of storage. Alternately, autoclaving of water-soluble starch with Ag salt @ 15 psi, 121^0C and for 5 minutes reduced and stabilized 10–34 nm size Ag nanocrystals for several applications[64].

For the purpose of preparing Ag and Au nanocrystals based nano catalysts, algal photochemical reaction was used where calcium alginate served as reducing agent and stabilizer for producing sub-10 nm size spherical nanocrystals [65].

Microorganisms have also been explored for synthesizing Au and Ag nanocrystals. For example, fusarium oxysporum was used in synthesizing both Auand Ag nanocrystalswherein the precursor salts were added to the broth that caused extra-cellular reduction resulting in extremely stable nanocrystals owing to the presence of NADH-dependent reductasesand the nanocrystals were stable even after a month [66-68]. Cyanobacteria

plectonema boryanum was used in synthesizing Ag nanocrystalswhere intra and extra-cellular reductions occurred involving metabolic processes as well as the extracts from dead cyanobacteria [68]. Though the nanocrystals and platelets inside the cells were sub-10 nm in size but those outside the cells were much larger (1–200nm) and also variedin compositions. Intracellular synthesis of much larger Ag nanocrystals up to 200 nm diameters and a variety of shapes, including triangles and hexagons,were also reported in pseudomonas stutzeri [69]. The reducing microbes namely morganella sp. was used in preparing 20 nm spherical Ag nanocrystals that were highly stable over a period exceeding six months [70].

Several compounds isolated from plants like glycosides from cape aloe (Aloe ferox Miller), aloin A and aloesin are reported as stabilizers in the preparation of Au and Ag nanocrystalswhere morphology changes by varying reaction conditions such as temperature, reaction time and reducing agents [71]. In another experiment, the cellular uptake by macrophages and HeLa cells was investigated using aloin A-stabilised and aloesin-stabilised 50 nm Au nanocrystals. Flavonoid glycoside named Apiin (apigenin-7-O-apioglucoside), which is abundant in parsley and celery, was successfully isolated from henna leaves and used for the synthesis of anisotropic Au nanocrystals and quasi-spherical Ag nanocrystals with an average size of 21–30 nm [72]. Guavanoic acid from apple and guava (Psidium guajava) was used in preparing Au-nanocrystals with protein tyrosine phosphatase 1B inhibitory activity having in-vitro stability in various medium including 10% saline, 0.2 M histidine, 0.2 M cysteine, 0.5% bovine serum albumin, 0.5% human serum albumin and phosphate buffers (pH 5, 7, and 9) [73].

Food sources of plant origin like soybean extract containing water-soluble proteins, carbohydrates, fat and dietary fiber, saponins, isoflavons and amino acids were used extensively for synthesis and stabilization of Au nanocrystals [74]. The anti-oxidant compounds present in soybean extracts were found effective in reducing Au salts and stabilizing the nanocrystals exhibiting in-vitro stability in various buffers and were found non-toxic. Soybean leaf extract was also found useful for the synthesis of Ag-nanocrystals with a size range of 25-100 nm [75]. Honey, made from flower nectar, was used as the reducing and capping agent for Au nanocrystals, producing either anisotropic or spherical shapes [76]. The same author reported the use of edible mushroom extract for the synthesis of Au, Ag and Au-Ag nanocrystals, which were found to be photo-luminescent [76]. Oat (Avena sativa) biomass was used for Au nanocrystal formations with tetrahedral, decahedral, hexagonal, icosahedral, multi-twinned and irregular shapes in which the pH of the reaction influenced the size of particles [77]. Size changes were noted from smaller to larger nanocrystals with pH reducing from 4 to 2. Au-nanocrystals were synthesized using oat and wheat biomass in aqueous solutions @ pH=4followed by their extraction using sodium citrate or cetyltrimethylammonium bromide as capping agent that facilitated their isolation from the biomass [77]. Using pear fruit extract, high purity triangular and hexagonal Au nano plates of 200-500 nm edge lengths were prepared under alkaline conditions [78]. Biomass of the edible brown alga fucus vesiculosus is known to reduce Au in an optimum pH of 4–9 [61]. It has been proposed that the hydroxyl groups in algal polysaccharides contribute to Au reduction through the oxidation of hydroxyl groups to carbonyl groups as mentioned already.

Nanocrystal Bioconjugation

Surface stabilization followed by chemical conjugation with various kinds of organic ligands has been developed extensively for better utility of nanocrystals in various ways in recent past. However, a similar concept could have been followed for conjugating nanocrystals with biomolecules. A brief description is presented here in the followings to highlight the utility of the concept by extending it to many newer areas of applications in life sciences.

Nanoparticles Partnering Biomolecules

Molecular recognition features of biomolecules combined with their addressable signatures and manipulations through biochemical procedures involving enzymes provide a strong basis for developing novel routes to design and synthesize advanced nanomaterials. In this context, integration of biotechnology and material science has been facilitated through extensive use of organic and inorganic biochemistry. Bioorganic tools for probing biological mechanisms have been helping in developing chemical ways to handle and manipulate biological components. In

such cases, chemical conjugations of organic ligands and inorganic nanoparticle provide ways of embedding biomolecular recognition systems to generate novel materials synthesis [79]. Citrate, phosphanes and thiols-group based stabilizations of the nanoparticles prevent uncontrolled growths and aggregations. Stronger binding ligands replace weaker ones by exchange reactions. This scheme was demonstrated in colloidal gold with thiol-containing proteins like immune-globulins (IgG) and serum albumins. It has been possible to synthesize DNA molecules with alkyl-thiol groups located at 39 or 59-ends by using appropriate phosphoramidite precursors. Such DNAs have been extensively used in preparing DNA-functionalized gold and semiconductor nanoparticles. Similarly, cyclic disulfide linkers provide stable capping, which are more appropriate for ligand exchange than the corresponding conjugates prepared using reagents containing a single thiol group or acyclic disulfide units [79].

Citrate stabilized gold and silver nanocrystals have been successfully conjugated to IgG molecules using sufficient binding between positively charged amino acid side chains and negatively charged citrate groups through non-covalent electrostatic interactions [79]. Protein adsorption stabilizes the metal nanocrystals and the steric repulsion among themselves prevents flocculation. The minimum amount of stabilizer needed for preventing flocculation corresponds to a single monolayer of proteins attached to the surface of the nanocrystal. Other examples of protein coating through electrostatic interactions include the directed adsorption of heme-containing redox enzymes at citrate-stabilized silver nanoparticles [79]- [82].

Another approach is based on thiols, disulfides and phosphane-ligands containing carboxy, amino, or maleimide-groups for coupling of biological components by esterification and amidation or reaction with thiol groups. To prepare gold conjugates as probes for histological applications, this strategy is commonly employed to conjugate proteins with well-defined 0.8-nm undecagold nanocrystals, stabilized with arylphosphanes and ligand [83]. Furthermore, gold nanocrystals have been conjugated with thiolated DNA oligomers to synthesize probes for homogeneous nucleic acid analyses and to prepare nanocrystal molecules [84,85].

A variety of thiol stabilized semiconductor quantum dot-colloids like cysteine or gluthathione-protected CdS and ZnS, or the efficient gram-quantity water-soluble ZnS powderswere studied in detail [86]-[88]. Mercaptoacetic acid stabilized CdTe nanocrystals were attached with e-amino groups of biotin-binding protein streptavidin through covalent amide bonding. In case of silica-coated Cd/chalcogen nanoparticles, the hydroxyl-groups at the surface were employed for covalent biomolecular coupling using a variety of silane molecules. This was also used in bio functionalizing larger SiO_2 microspheres that are used for conjugating SiO_2-coated core (CdSe)/shell (CdS) nanocrystals to biomolecules [89]. When the inorganic nanocrystals are covered with a bioorganic matrix, such as polypeptide core in ferritin, the whole protein-modification chemistry is open for further functionalization and coupling applications. In spite of several attempts already made as briefly mentioned above, there is still a great demand for alternative methods to overcome the typical problems that arise in the biofunctionalization of the inorganic nanoparticles. Harsh reaction conditions, for example, often lead to the degradation and inactivation of sensitive biological compounds and ligand-exchange reactions that occur at the colloid surface often hinder the formation of stable bioconjugates. Moreover, the synthesis of nanoparticles with well-defined stoichiometryinvolved in biomolecular complexes is still a challenge and is particularly important from a molecular engineering point of view to generate well-defined nanoarchitectures.

DNA-Based Nanocrystal Aggregates

The exploration of biomolecules as components of nanostructured systems for developing active devices was envisioned quite early [90-92]. DNAsare particularly well recognized as a building material in nanoscience [93,94].The enormous amount of specificity inherent in adenine - thymine (A-T) and guanine - cytosine (G-C) bonding allows a versatile programing of artificial DNA structures. Possibility of synthesizing a large variety of DNA structure using automated methods, amplifying any DNA sequence from microscopic to macroscopic quantities by means of polymerase chain reaction (PCR) enhances the capabilities of DNAs as molecular tools. Another special feature of DNA is its mechanical strength in short double helices to the extent that they can be easily employed as rigid rod spacer between two tethered functional molecular components besides displaying a relatively higher physicochemical stability. Finally, a complete toolbox of specific biomolecular reagents, such as

endonucleases, ligases, and other DNA-modifying enzymes, is available for processing of DNA-materials with atomic precision and accuracy. No other polymeric material offers these advantages that are well suited for molecular constructions in the range of about 5 nm up to a few micrometers [94].

Nanocrystal bioconjugation is the 'natural' extension of the concepts of ligand exchange and chemical functionalization to the biomolecules. Mother Nature offers a large variety of organic molecules of different compositions, sizes and complexities that serve to provide structures and functions to the biological processes and related organisms. Numerous examples include lipids, vitamins, peptides, sugars as well as natural polymers including proteins, enzymes, DNAs and RNAs. In addition, it is also possible to synthesize hybrid materials by attaching inorganic nanocrystals to biomolecules to let them interact with biological systems. On the other hand, biomolecules are considered as polymers that can be exploited for functionalization or in preparing spatial assembly of nanocrystals. Nanocrystal–biomolecule conjugates bring together the unique properties and functionalities of both the material components in a synergistic manner.

There are four major categories of bio-conjugated nanocrystals that are listed below:

1. Ligand-like attachment of biomolecules to the surface of the inorganic nanocrystal core, commonly through the process of chemisorption,
2. Electrostatic adsorption of positively charged biomolecules to negatively charged nanocrystals or vice versa,
3. Covalent binding using functional groups on both nanocrystals and biomolecules, and lastly,
4. Non-covalent and affinity-based receptor-ligand systems.

Affinity-based systems, quite prevalent in Nature, have, of late, attracted considerable attention [56]. Well-known example of avidin–biotin based system exploits the phenomena of molecular recognition in which biotin molecules conjugate with avidin proteins [95]. Such a bond is extremely stable, resisting harsh chemical environment and even elevated temperatures. Monomeric streptavidin has relatively reduced affinity to biotin. Bond strength and specificity of biotin–avidin conjugation has been extended to a large number of applications in nanobiotechnology. As a result of these developments, a large variety of biotinylated reagents and biomolecules like DNA oligomers, peptides, antibodies and fluorescent dyes are commercially available today.

The stronger attachment of polyhistidine-containing proteins to CdSe/ZnS nanocrystals with a dihydrolipid acid ligand layer was studied as a robust self-assembly protocol, where polyhistidine binds directly to Zn atoms in ZnS as demonstrated in the control experiments with different target molecules and ligands without free carboxylic groups [96]. This protocol involves only purification steps, which promote the conjugation of QDs with a number of different proteins for a variety of applications.

Nanocrystals with Biotin, Avidin and Derivatives

Biotin with free carboxylic group binds covalently to the nanocrystals by conjugation or even directly to the inorganic particles by ligands modifications [95]. For conjugation, only solubility and charge or functional groups of the biotin are of importance. Avidin, streptavidin and other variants are practically characterized by their molecular weight, isoelectric points, degree of hydrophobicity and available functional amino acid residues commonly consisting of carboxylic acids, amino and thiol groups. Proteins are generally positively charged at pH values below their isoelectric points and negatively charged for values that are above. This gives rise to electrostatic adsorption of avidin to negatively charged nanoparticles, while streptavidin and neutravidin at a lower pH get loosely attached to the nanocrystals non-specifically[95]. To improve the stability of these nanocrystal–protein complexes, an additional covalent crosslinking needs to be introduced on a similar system. The availability of functional groups on the protein surface, streptavidin has been covalently linked to QDs with carboxylic groups or primary amines. Alternatively, streptavidin has been attached to the inorganic QD surface via a polyhistidine tag by direct adsorption [95].

Nanocrystals, modified with larger numbers of biotin molecules, form large aggregates with streptavidin by inter-

particle crosslinking, owing to the multi-valent nature of both the nanocrystals and streptavidin. This effect is not only observed in case of nanocrystals attachment with biotin–avidin. It is rather a general problem in the case of two or more multi-valent binding partners and covalent conjugations, where both nanocrystals and target molecules have a larger number of reactive functional groups[95].

DNA and RNA Attachments

DNAs and RNAs are generic polymeric molecules showing prominent features of self-assembly with a complementary strand presenting specific example of molecular recognition [97]. DNAs can be used as a 'programmable' molecules with a very large number of possible sequences and conformations and are therefore used as a building blocks and structural elements for the assembly of artificial structures. Synthetic DNA molecules of arbitrary sequences and with a variety of functional end groups are commercially available now and can be conveniently attached to Au-nanocrystals by a thiol-Au bond in an aqueous medium where oligomers are added in excess to the Au nanocrystals and spontaneously bind to the nanocrystal surface [98].

The strategy of ligand exchange has also been applied to structures like Au-nanorods, Ag nanocrystals, MPA-stabilized CdSe/ZnS QDs and Pt nanocrystals decorated with amino-modified DNA. Even under optimized conditions, the binding of DNAs to the nanocrystals does not occur quantitatively; however, the DNA density can be influenced by adjusting the excess ratio or by dilution with other ligands. In case of rather long DNA strands, attachment of a single DNA molecule increases the size of the Au–DNA conjugate sufficiently to separate discrete bands by gel electrophoresis, consisting of nanocrystals with integral numbers of DNA molecules per particle [98].

Owing to the possibility of realizing a large number of different sequences for a DNA or RNA strand of given length, there also exists an even larger variety of possible conformations in terms of secondary and tertiary structure of these molecules[98]. It has been found that certain sequences can strongly bind to a target molecule by molecular recognition, determined by geometric matching of the surfaces of the two molecules. This kind of interaction may be due to electrostatic, hydrophobic, van der Waals forces and hydrogen bonds. This can be employed to generate aptamer sequences to a given target molecule by molecular evolution, technically realized by multiple randomization, selection and amplification of strongly binding sequences. Aptamers have been attached to the Au nanocrystals via a thiol group, to QDs or silica-coated Au nanocrystals by covalent conjugation, to avidin-modified magnetic nanocrystals and biotinylated DNA aptamers to QDs with streptavidin[98].

DNA is a negatively charged polyelectrolyte molecule causing electrostatic adsorption of DNAs to the positively charged surfaces of nanocrystals with quaternary amines and of RNAs to the nanocrystals with tertiary amines.

Besides, the ligand-like direct binding of DNAs to the nanocrystal surface; conjugation chemistry has also been employed to covalently attach the DNAs to functional groups available on the nanocrystals surface. This has been carried out to bind amino-functionalized DNAs to nanocrystals with carboxylic groups and thiol-modified DNAs to the maleimide groups. Apart from covalent conjugation, avidin–biotin has also been used as the non-covalent receptor-ligand system for the attaching DNAs to the nanocrystals, both with biotin-modified DNAs and biotin-modified nanocrystals[98].

Peptide, Protein, Enzyme and Antibody Conjugations

Peptides and proteins are amino acids, linked to linear sequences by amide bonds. Smaller number of 50–100 amino acid sequences containing peptides is commercially available today, while larger poly-amino acids proteins exhibit tertiary and quaternary structures. Enzymes are molecules with reactive centers that catalyze biochemical reactions and are responsible for metabolism in living organisms. Antibodies are proteins with important functions in the immune system wherein they have the ability to specifically bind to the antigens, in principle arbitrary target molecules, mediated by molecular recognition. Proteins are generally made up of a sequence of 20 different standard amino acids in addition to other naturally occurring or synthetic amino acids that are linked together by amide bonds and possess different side-chain residues. Each peptide has one carboxylic and one primary amino group at its ends, while the amino acid side chains introduce additional functional groups. The amino acid sequence determines the unique properties of each of a large number of possible structures and these, in turn,

determine the secondary and tertiary structure that a protein is folding into and that ultimately results in a functional biomolecule. The specific function of a protein is determined by geometric and physicochemical properties of the outer surface, given by the almost arbitrary motifs of the folded amino acid sequences. Protein inside is often hydrophobic, while hydrophilic amino acid side chains are pointed outwards into the solution. The thiol group of a terminal cysteine residue can also be used as the anchor for attachment of a peptide to the surface of nanocrystals. These properties clearly make peptides and proteins particularly very interesting molecules to be combined with inorganic nanocrystals, both for basic research and applications that make use of the specific functions of these biomolecules.

Peptides are smaller molecules with 'programmable' sequence of amino acids that allow the rational design of molecules capable of stabilizing nanocrystals or introducing various functional groups. In addition, particle synthesis and phase transfer protocols with the help of peptides have also been developed successfully. Making use of the biological functionality of certain peptides, the specific uptake of nanocrystals by cells can be optimized by nanocrystal conjugation with the corresponding peptide, as reported for Au nanocrystals or QDs by ligand exchange with cysteine-containing peptides. The peptide coating may be used for modulating reaction of the immune system towards nanocrystals. Covalent conjugation may be used for peptide modification as demonstrated in case of quantum dots with amino groups or magnetic iron oxide nanocrystals. In addition, streptavidin modified quantum dots have been conjugated to different biotinylated peptides.

Several strategies have been proposed for conjugation of proteins to nanocrystals, including enzymes and antibodies. First, 'non-specific' adsorption was employed where the nanocrystals were incubated with the protein, which was adsorbed to the particles by electrostatic attraction in case both the partners were oppositely charged, by van der Waals forces, hydrogen bridges, gold–thiol bonds from cysteine residues or by hydrophobic interaction especially when the pH was close to the pH of the protein or the nanocrystal so that the electrostatic repulsion was reduced. After adsorption, any one of these forces or a combination of few of them together, might cause irreversible immobilization of the proteins. Potentially, the protein could get into intimate contact with the particle surface by partial or complete denaturation giving rise to hydrophobic interaction of the inner part of the protein and/or an increased contact area between the binding partners. Electrostatic binding wasdemonstrated for protease to MPA-modified quantum dots and desorption of proteins could be triggered by increasing the electrolyte concentration that effectively shielded the attractive electrostatic interactions.

The examples of protein modification of the nanocrystals by covalent conjugation included QDs, rods and magnetic nanocrystals possessing amino groups that were modified by enzymes. By click-chemistry, lipase was conjugated to Au nanocrystals as well as peptides to gold nanorods.

Antibodies are possible to conjugate to QDs covalently as well as to magnetic-fluorescent composites and by bi-functional cross-linkers to the thiol-containing, silanized CdTe quantum dots [99]. Antibody fragments possessing free thiol-groups were also attached to the free amino groups of QDs by means of a hetero-bi-functional cross-linker and biotinylated antibodies to streptavidin-modified QDs.

Silica-coated nanocrystals of different cores with amino functional groups are possible to modify with antibodies by bis-NHS reagents. Dextran-coated magnetic iron oxide nanoparticles were covalently conjugated with peptides, oligonucleotides, proteins and antibodies as demonstrated experimentally. Further examples are found in a number of very useful reviews detailing bio-conjugation of Au nanocrystals [80], QDs [100] and nanocrystal-enzyme conjugates [101].

Fluorescent Dyes and Multi-Functional Particles

Besides functional groups or biomolecules based functionalization, nanocrystals have also been modified with a number of other functionalities including fluorescent dyes or fluorescent proteins that were put to use in fluorescence labeling of non-fluorescent particles or to generate systems exhibiting energy transfers. Common examples included fluorescent dyes that were quenched by Au-nanocrystals or could be excited by fluorescence resonant energy transfer via a QD serving as donor for biosensor applications.

Nanocrystals synthesis, phase transfer, functionalization and bioconjugation, all of which have some common features with sufficient overlaps, in terms of the binding of organic ligands to the inorganic nanocrystal surface and they depend on each other since those ligands introduce chemical functionality, as finally do complex molecules, which ultimately will determine the physicochemical properties of the resulting nanocrystals.

The motivation for particle modification is to have control over the interaction of the particles with the environment, which naturally starts taking place at the nanocrystals surfaces. By appropriate modification, phase transfer, specific and non-specific binding to target molecules or surfaces, biomolecules or cells could be tuned for the controlled targeting or assembly of nanocrystals. Furthermore, additional functionality could be provided to the nanocrystal properties inherently coming from its core for biological impact or fluorescence emission for non-luminescent materials.

For multi-functional particles, three approaches were identified namely - composite materials generated *in-situ* during synthesis by growing nanocrystals with domains of different functional materials; post-modification of particles with functional molecules like fluorescent QDs with paramagnetic organic molecules or non-fluorescent NCs with fluorescent dyes, and assembly of composite materials by combining different nanocrystals with different functionality.

Biomimetic Applications

Of late, several intelligent features of pathogens were put into use for their applications as drug carriers, sensors and catalysts [102]. However, using pathogens in any form has not been free from hazards including safety, special handling facility besides time and cost. It was, therefore, considered necessary to try some alternatives where biologically useful material in benign form was employed for this purpose. Biomimetic nanocrystals are currently emerging as an active part of a biomolecule with better stability having no harmful component. Surface modifications using multiple functional groups are offering better options in NCs to use them as a platform[102]. Nanocrystals are comparatively easier to modify for mimicking an antigen or marker than growing cell cultures or working with live animals, which are time consuming as well as cost intensive. Conjugation chemistry to attach functional ligands and macromolecules to nanocrystals is well developed for its use in a large number of systems including antigen/antibody interactions via different synthetic routes. Methods of preparing core-shell type nanocrystals are available, as discussed elsewhere to render them in aqueous or organic media. Metallic as well as nonmetallic materials are used in preparing nanocrystals including monolayer protected nanocrystals (MPNC), organic polymers, virus-like particles, protein particles, colloidal particles, and semiconductor QDs. Thiol-capped MPNCs are getting well recognized for their effective uses because of their easier syntheses, significant water and air stability, electrochemical and optical properties and their surface functionalizations by adding biologically relevant ligands, such as peptide sequences of epitopes [102].

A number of routes were, thus, developed to functionalize MPNCs to mimic certain biological features out of which only few important ones are very briefly described here. In a place-exchange reaction, an incoming ligand was made to replace one of the existing capping. In one of the early attempts, alkane thiolate clusters with ω-functionalized thiols in toluene were used but this was extended to aqueous/aqueous buffer solutions as well. The rate of ligand exchange was found to depend upon both the concentration of incoming and exiting ligands. While the exact nature of place-exchange reactions appeared complicated as investigated in detail by many, the utility of place-exchange for functionalizing MPNCs was still there because of inherent simplicity. The reaction rate was found to increase with smaller size entering ligands and shorter length of the protecting ligand chains. Consequently, place-exchange of a large biomolecule was favoredinvolving a peptide or protein fragment, with a small protecting ligand such as tiopronin [102].

Various unique features of NCs provide some predictability or control in anchoring of the place-exchanged functional groups. The reaction, in this context, improved with increasing concentration of the incoming ligands, but it was rarely complete due to the exchange difficulty at the terrace sites. All the recent findings, in this context, clearly showed the importance of surface structures that were responsible for explaining the nature of the place-

exchange mechanism [102].

In another alternative to the solution-phase place-exchange, mentioned above, solid-phase place-exchange reactions were explored by using a polystyrene Wang resin with acetyl-protected 6-mercapto-hexanoic-acid attached via an ester bond. Here, thiol groups were de-protected and allowed to undergo place-exchange with butane thiolate-protected Au nanocrystals, followed by washing away of un-exchanged product and cleaving of the exchanged particles. It confirmed place-exchange of one ligand on to a particle surface [102].

Macromolecules like cysteine residues in proteins or adenosyl phosphothioate residues in DNA oligonucleotides contain thiols that make biomolecules amenable to place-exchange reactions. It is also possible to introduce ligands into the MPNC monolayer, which undergoes electrostatic interactions with biomolecules like biotin–streptavidin interaction or biotin–anti-biotin interaction. All these routes provide straight ways to prepare a group for place-exchange and create functional NCs [102].

Other strategies included simple organic reactions with ligands bound to the MPNCs like triazole cycloaddition to a bromine functionality, direct functionalization of a hydroxyl group, amide coupling and ester coupling. All these methods enabled post-exchange reactions to take place, allowing the surface to be modified in a controlled fashion [102].

Protein-A coated nanocrystals were functionalized with proteins, while still participating in the same biomolecular recognition events as the free proteins [102]. It was possible to detect anti-protein-A in serum by aggregating protein A-coated Au NCs and observing an absorption change at 620 nm. In another study, a single-chain Fv (scFv) antibody fragments were conjugated to glutathione Au-MPNCs with strong coupling that exhibited binding specificity to the antigen protein. Elimination of the flexible regions in the whole antibody led to improved rigidity. Conjugation was accomplished by attaching a cysteine-terminated C-terminalaffinity tag (FLAG) to the scFv. Using special type of cryo-electron microscopy, it was possible to verify the antibody activity by observing the attachment of four Au71–scFv–glutathione units to single tetrameric influenza N9 neuraminidase units. In both these cases, the NC was used to aid in the detection of antibody–antigen binding, without actually using it as a biomimetic building block. Similarly, peptide-functionalized NCswere surface-functionalized by peptide or by place-exchange with the ligands after nanocrystal assembly. The first example involved synthesis of NCs with a protecting peptide from the histidine-rich protein II of *Plasmodium falciparum.* Using standard procedures, peptide from HRP II were used as stabilizing ligand on different metal cores: ZnS, Au^0, Ag^0, TiO_2, and AgS. The biological significance came from the recognition of the particle by a monoclonal antibody specific for *P. falciparum*[102]. They were able to detect the peptide-encapsulated particles, as they would do with the whole protein. This antibody–nanoparticle recognition showed that their particle mimicked the native epitope [102].

Another MPNCs group was synthesized containing an epitope from influenza protein, termed as HA-MPNC. The 10-amino acid peptide was again synthesized with a terminating cysteine residue to promote place-exchange reaction. This peptide which was selected, as it was a neutralizing site for influenza and a monoclonal antibody, specific for this epitope on HA, was available commercially. It was shown that the HA-MPNC was more efficient in presenting the peptide to the antibody, resulting in a higher ratio of antibody to peptide binding when compared to the 2-D surface [102].

Biomimetic NCs have shown significant promise as a tool for targeted cell entry that was fairly complex, but the small size of gold nanocrystals and the functionality available from synthetic peptides made this quite possible. Inspired by viruses, efforts were made to conjugate peptides to bovine serum albumin via an ester linker and then conjugated the BSA to gold NCs. The four peptides used were from viral cell entry/targeting proteins and it became possible to achieve targeted entry of the gold NCs into the nucleus of HepG2 cells leaving the cells still viable after entry of the gold NCs [102].

Surface functionalized Au NCs with carbohydrates could be explored for many biological applications relying on carbohydrate and protein interactions. This was first accomplished by using carbohydrate functionalized Au NCs to mimic glycocalyx, the sticky film found on the outside of many different cells [102].

Nanocrystal Superlattices (SIs)

The technology of preparing ordered films from the NCs opened an entirely new area with enormous promises of synthesizing materials possessing properties that were distinctly different from their random collections in a colloidal form. However, for measuring their collective properties and determining their suitability for active devices and other applications, it was very much desirable to prepare superlattices of reasonable thickness with controllable dimensions for their maneuverable placements.

It is interesting to note that controlled drying of solvents containing monodisperse NPs produced single or several-layer SLs with lateral dimensions extending up to the millimeter ranges [103]. Extending similar processes, three-dimensional super crystals of monodisperse NCs were prepared in beakers or on substrates. In a later attempt, controlled evaporation of solvent was extended to deposit super crystals in lithographically defined channels. Here, a drop consisting of CdSe or Fe_2O_3 nanocrystals, dispersed in a high-boiling-point/low-boiling point two-solvent system, was put into a central reservoir from where the solution was guided into a series of long and narrow channels. With the progress of solvent evaporation, assisted by the vacuum over a period of several hours,the nanocrystals concentration increased leading to ordered growth of super crystals. The high boiling point solvent slowed down the process of drying adequately to allow the crystallization of NPs. Precise fabrication of ~100 layer superlattices, with ~1 μm lateral dimensions, offered, as such, an adequate opportunity for their use in optical, electronic, magnetic and mechanical investigations of their emerging collective behavior and potential applications [103].

Nanocrystals in a solvent are noted to show inherent tendency of self-assembly into ordered superlattices leading to the formation of two-dimensional ordered monolayers or three-dimensional microcrystals [104]. Possibly, an integration of these superlattices into a suitable polymer matrix would not only add mechanical stability but also provide additional leverage of tailoring the superlattice structures by the length and stiffness of the polymer chains for their future applications. In this context, although, inter-particle distance control has been varied using lighter ligands, to some extent, but polymers would eventually provide a much broader range of lattice constants. Of course, the preparation of such ordered assemblies of NCs and polymers poses a number of challenges that are primarily related to the incorporation of high quality monodisperse NCs having simultaneously adequate compatibility with the polymer matrix in preparing a superlattice. Two routes that were explored, in this context, involved either preformed nanocrystals that were subsequently integrated into a polymer matrix or using polymer micro-domains to synthesize nanocrystals from precursors within the polymer matrix. In either of these protocols, there were certain limitations like poor compatibility with the matrix that still needed to be addressed adequately [104].

Solvent evaporation protocols were, however, employed successfully to prepare nanocrystals superlattices as discussed above. Extending a similar reasoning,itseems quite possible to create a similar condition using rapid evaporation of solvents like supercritical CO_2 and others where it is much easier to prepare NCs superlattices. The distinct advantage of SCF based crystallization is its faster de-pressurization speed causing quicker supersaturation and nucleation of the NCs via self-assembly route [105].

Unary and Binary Superlattices

Nanocrystals were primarily considered as “artificial atoms” because of their unique features already discussed earlier. Once the technique of assembling these artificial atoms into desired higher-ordered architectures called ‘nanocrystal superlattice’ was perfected, it was naturally expected to open a new method of synthesizing functional materials for their applications in various related fields [106]. Methods are available, by now, to prepare NC-thin films and colloidal crystals with different kinds of superlattice structures demonstrating collective properties. However, large-scale preparation of nanocrystal superlattices with well-defined size and shape has still been an outstanding challenge that needs further investigations [106].

NC-assemblies, prepared using processes including spray drying, emulsion polymerization, DNA-induced growth, polymer mediator-induced assembly and Debye screening, neither possessed sufficient long-range order

nor had proper size or shape distributions [106]. In this context, in a recent approach, high-quality colloidal super particles with spherical shape and relatively narrow size distributions, exhibited nearly perfect superlattice structure with nm-scale lattice constants using Fe_3O_4 nanoparticles in a nonpolar-solvent. In addition, these super particles could be further assembled into close-packed solid structures, demonstrating their role as a new type of building blocks in the science of nanomaterials. Using oleic acid hydrocarbon chain on Fe_3O_4 nanocrystals and dodecyl-tri-methyl-ammonium bromide surfactant, micelles were prepared and added to the ethylene glycol solution, where nanocrystals-micelles were decomposed due to removal of the DTAB molecules in the solution. Strong interactions between nanocrystal ligands and ethylene glycol solution resulted in aggregation and super particle formation. Here, a chloroform solution of oleic-acid-functionalized Fe_3O_4 nanoparticles was mixed with aqueous DTAB solution resulting into micelles in aqueous solution after chloroform evaporation. Under vigorous stirring, the nanocrystal-micelle solution was injected into a polyvinyl pyrrolidone ethylene glycol solution and the mixture was heated to 80°C using 10°C/minute heating rate after which the temperature was maintained for 6 hours and then, the solution was cooled down to room temperature resulting in colloidal super particles precipitated with a typical yield of about 70%. SEM/TEM analysis of the synthesized samples confirmed the formation of 190 nm diameter spherical particles. The repulsive interaction between ethylene glycol and Fe_3O_4 nanocrystals was likely the cause of spherical shape, based on minimum surface energy considerations. In addition, these colloidal particles were further assembled into multilayered, close-packed particle thin films [106].

A room temperature protocol for preparing oxide nanomaterials using metal cations and oxide anions in alcohol, was developed for preparing ordered, free-standing ZnO nanocrystal superlattices by either evaporation or precipitation-induced self-assembly from carboxylic and alkylthiol stabilized and functionalized monodisperse nanocrystals. These superlattices were coated in form of a thin film on indium tin oxide deposited glass substrates for characterization to explore their possible applications [107].

Self-assembly of a large variety of binary NC-superlattices from colloidal solutions of nearly spherical NPs of different materials, extending coherently packed domains up to 10 mm in lateral dimensions, was accomplished. In quite a few cases, several binary superlattices (BNSLs) were formed simultaneously on the same substrate, under identical conditions. The same mixture could self-assemble into BNSLs with very different stoichiometry and packing symmetry such as a combination of 6.2 nm PbSe and 3.0 nm Pd nanocrystals, 11 different structures were demonstrated. This kind of structural diversity on one side defied the theoretical and experimental expectations but otherwise promised enough potentials of modular self-assembly at the nano scales.

The formation of binary nanocrystals with packing density lower than single-phase FCC close packing ruled out as the cause of ordering. Moreover, even van der Waals, steric or dipolar inter-particle interactions were insufficient to explain the ordering observed besides the constituents trying to separate into single-component superlattices. However, the opposite electrical charges on NCs could be considered as a cause of affinity between one type of NCs like dodecane-thiol-capped Au, Ag, Pd with the other like PbSe, PbS, Fe_2O_3, $CoPt_3$ capped with long chain carboxylic acids. In case of oppositely charged NCs, the Coulombic interaction stabilized the BNSL while destabilizing the formations of single component superlattices.

A strong possibility emerged where tuning of the nanocrystal charge states could be used for influencing the self-assembly of an ordered NC-superlattice. This concept was verified while noting reproducible switching between different BNSL structures by adding carboxylic acids, TOPO and dodecylamine to the colloidal solutions of PbSe, PbS, Fe_2O_3 and Au, Ag, Pd NCs. Combining solutions of 6.2 nm PbSe and 3.0 nm Pd NPs in the ratio of 1:5 gave rise to several BNSL structures with $MgZn_2$ and cuboctahedral AB_{13} lattice symmetry. However, the same nanocrystals assembled into orthorhombic AB and AlB_2-type superlattices after adding oleic acid and into $NaZn_{13}$ or cuboctahedral AB_{13}-type BNSLs after mixing dodecylamine or TOPO, respectively. In the AB_{13}-type BNSL, metal NCs assembled into icosahedral $NaZn_{13}$ or cuboctahedral AB_{13} clusters, with each large PbSe particle surrounded by 24 metal spheres at the vertices of a cube. In the presence of TOPO, the metal NPs were neutral favoring formation of the Pd_{13}, Au_{13} and Ag_{13} clusters. The clusters of metal NPs in turn provided screening of the charges on PbSe NCs in the AB_{13}-type BNSL.

Gold, silver and palladium nanocrystals for BNSL studies were prepared by ultrasonic treatment of metal salts dissolved in toluene in presence of dodecyl-dimethyl-ammonium bromide (DDAB). For the synthesis of Au, Ag and Pd NCs, $AuCl_3$, $AgNO_3$ and $PdCl_2$ salts were used with DDAB [108]. Aqueous solution of $NaBH_4$ was added slowly while stirring vigorously and after 20 minutes, 1-dodecanethiol was added and stirring was continued for another 5 minutes. Adding ethanol precipitated the NCs that were re-dispersed in toluene in presence of 1-dodecane-thiol and refluxed under nitrogen. Fe_2O_3 NCs were synthesized by injecting iron penta-carbonyl into tri-octyl-amine in the presence of oleic acid @ 270 ^{0}C and 250 ^{0}C, respectively, yielding 11 and 13.4 nm nanocrystals. After heating the mixtures for 1 hour @ 320^{0}C, it was cooled to room temperature. The mixture was warmed for 1.5 h @130^{0}C and 1 hour @ 320^{0}C after adding tri-methyl-amine N-oxide to oxidize iron NCs. A carbon/SiO_2 coated TEM grid, silicon nitride membrane or alkyl-functionalized Si chip was placed inside a 60^0–70^0 tilted glass vial having colloidal solution kept in a low-pressure chamber. Ordered binary nanocrystals were formed upon evaporation of the solvent like toluene or mixtures of toluene and tetrachloroethylene or chloroform. The best binary assemblies, determined by the length scale of ordering and a low defect density, were prepared by evaporating relatively concentrated solutions @ 45 ^{0}C under reduced pressure of 3.2 kPa [108].

Spontaneous self-organization of multicomponent micron-sized NCs into SLs is of scientific interest for understanding the assembly process on the nanometer scale and is of great importance in bottom-up fabrication of functional materials and devices [109]. In particular, co-assembly of two types of NCs into binary nanocrystal superlattices (BNSLs) has been pursued as it provided a low-cost method to design meta-materials with precisely controlled properties that arise from the organization and interactions of the nanocrystal components. A general procedure of preparing centimeter-scale, uniform membranes of BNSLs that could readily be transferred to arbitrary substrates was reported recently involving liquid–air interfacial assembly of multicomponent NCs and circumventing the limitations of the current assembly strategies, allowing integration of BNSLs on any substrate for the fabrication of NC-devices. Magneto-resistive devices were fabricated by using large-area BNSL membranes. Magneto-transport measurements confirmed that magneto-resistance was stoichiometry dependent of the BNSLs ordering. Transferring BNSLs was used in realizing membranes and other architectures that were not accessible earlier [109].

The drawbacks in preparing high quality NCs were addressed to in a program and a potential solution for preparing bimetallic NCs was developed in which crystal structure; size, composition, surface chemistry and the distribution of the component metals within a bimetallic nanocrystal could be precisely controlled. A multi-step procedure was developed to substitute commonly available one-pot synthesis or two-step protocol, yielding bimetallic NPs with an unprecedented control of particle attributes, quality and consistency in which each step could take care of one attribute of nanocrystal at a time. Improved monodispersity with tunable attributes like size; crystal structure, composition and elemental distribution were possible to take care of simultaneously. For a systematic study of structure-property relationships, a library of high-quality nanocrystals was prepared to offer recipes for tailoring the NP-properties of interest for the intended application, or to extend the method of synthesis to other bimetallic or more complex multi-metallic systems. For example, precise process control could shift the absorption band of Ag-Au bimetallic NCs continuously from the visible to infrared region. High quality monodisperse NCs facilitated the self-assembly of 3D superlattices with different packing patterns and long-range orders. The fabrication of binary nanocrystal superlattices with controllable and predictable structures using self-assembly, was particularly exciting as it provided opportunity of creating new multifunctional nanostructured materials.

Micrometer-size 3-d gold superlattices were prepared at an air/water interface by mercapto-succinic acid (MSA), N-(2-mercapto-propionyl)-glysine (MPG), and reduced glutathione treated Au-NCs by decreasing the repulsive interactions between the surface modifiers with the help of adjusting the acid concentration. The experimental measurements confirmed the presence of hcp and fcc-type single-crystal structures. Measured optical absorption confirmed the red shift of SPR peaks with increase in nanocrystal density along with decreasing peak widths with NCs forming regular lattices in contrast to the observed optical absorption behavior of randomly assembled nanocrystals.

Silicon Nanocrystal Superlattices

Strong motivations for preparing Si-nanocrystals in a form suitable for their use in light emitting devices tempted several teams to look into this from of microelectronics application angle. The concept of phase separation and crystallization of Si NCs from amorphous thin film protected by SiO_2 was thus initiated involving well-established microelectronic processes [110]. A number of attempts were made, in this direction, using porous silicon, silicon clusters embedded in SiO_2 matrix; sub-stoichiometric SiO_x films in $SiO_2/SiO_x/SiO_2$ configuration prepared by CVD, sputtering and reactive evaporations. All these methods, however, produced relatively broader size distribution of the synthesized Si-NCs. Size control in these methods was normally obtained by varying Si content within the SiO_2 matrix, changing the etching conditions in the case of porous Si and subsequent oxidation of the nanocrystals [110].

In another alternate approach, Si/SiO_2 superlattices, prepared by molecular-beam epitaxy (MBE), reactive magnetron sputtering, co-sputtering, plasma-enhanced and low-pressure CVD and reactive evaporation, were used for silicon NCs synthesis. Brick shaped silicon nanocrystals were obtained after crystallization of the amorphous silicon layers was surrounded by insulating layers. Insulating SiO_2 layer was, subsequently, replaced by other insulators like Si-NC:H/a-Si:H (RF Sputtering), Si/SiN_x (E-Beam Evaporation + Electron Cyclotron Resonance Plasma Nitridation, Excimer Pulsed Laser Deposition and LPCVD), $Si/Si_xO_yN_z$ (LPCVD) and Si/CaF_2 (Room Temperature MBE) [110].

A novel but very simple method was reported recently for the preparation of Si nanocrystal superlattices using reactive Si evaporation to incorporate oxygen in Si resulting in sub-stoichiometric SiO_x [111]. Presence of sub-stoichiometric oxide was confirmed by EDX giving composition of $SiO_{1.8}$. TEM ruled out the presence of any crystalline structure in as deposited films. Subsequent dissolution of SiO_x in 0.5-wt % $HF+H_2O$ solution released Si clusters dispersed in the solution in about 30 minutes. Assembly of the Si clusters into three-dimensional lattices proceeded just after HF addition possibly due to inversion of Si cluster surfaces from hydrophilic to hydrophobic form after removing the oxide on their surface [111]. Narrow size hydrophobic particles spontaneously assembled into large size and well-ordered structures. Smaller size Si clusters were attracted to the air/suspension interface whereas the larger clusters descended to the bottom. This was noted to be favorable for separation of Si clusters: smaller clusters segregated to the surface, while larger ones precipitated. High-quality three-dimensional lattice arrangements were found at the air/suspension interface leading to the growth of Si cluster superlattices over a period of 1 hour. TEM analysis confirmed that micron-size faceted structures belonged to nanocrystals superlattices grown under equilibrium comprising of mainly cubic structures with less than 10% hexagonal structures. The presence of fcc and bcc structures with a ~ 0.75 and ~ 0.69 nm, respectively, was confirmed during further characterizations. The nearest-neighbor distances between lattice points in the above structures were estimated as 0.53 and 0.60 nm, respectively, which were considerably larger than the interatomic distance of Si in bulk and thus showing the presence of three-dimensional arrays of Si clusters. These Si-NCs based superlattices showed intense PL under the excitation light of 435 nm resulting in the emission of blue-green and orange colors. Though such small Si clusters are expected to spontaneously convert into polycrystalline or amorphous Si due to a large number of unsaturated bonds of the surface atoms, but perhaps hydrogen termination during HF treatment provided them the observed stability [111].

Outcome of this study, however, opened up an opportunity of depositing Si-NC-SLs on patterned hydrophobic Si or graphite wafers just by dipping the same in the solution. The present fabrication method of Si-SLs could very well be incorporated into wet process of integrated circuit fabrications easily in near future.

Biomolecular Nanocrystals Superlattices

Many nanosize building blocks are prone to assemble into macroscopic structures which provided the effective control of the inter-block interactions and entropy effects are known and incorporated into the protocols. However, still it remains a challenge to use self-assembly to prepare systems comprising of different types of nm-size building blocks leading to novel magnetic, plasmonic and photonic meta-materials. A conceptually simple idea is to use programmable interactions between building blocks derived from a variety of biomolecules. Using programmable DNAs to control the placement of nanocrystals in 1 and 2-d hasbeen demonstrated. However,

theoretical study of how to extend this approach to three dimensions is limited as in most of the experiments amorphous aggregates have been observed.

Transition from a completely disordered phase to a 3-d ordered phase in a DNA-guided particle assembly was theoretically shown to depend upon the inter-particle interaction potentials that are defined by the interplay of attractive (E_a) and repulsive (E_r) energies and the ratio of repulsive interaction range (d_r) and particle diameter (d_p) [112]. These parametric ratios E_a/E_r, and d_r/d_p in DNA particle assembly can be manipulated in a variety of ways, including the design of individual DNA, their shell structures and solution ionic strengths [112]. Experimentally, in case of a single component system, DNA-induced crystallization was observed near surfaces into hexagonal close-packed crystals with short-range interactions whereas in case of long-range interaction potentials for which the expected non-close-packed structures were not achieved. In a later study, a set of DNA-capped gold nanocystals with different DNA structures were allowed to assemble into mesoscale aggregates [113]. The complementary nature of recognition sequences of the DNA capping provided the driving force where length of the recognition sequence sets the scale of adhesion from 30 – 0 k_BT from room temperature to DNA melting temperature, respectively. In a ''brush'' regime, DNA length and the flexibility of the non-complementary internal spacer allowed the tuning range of repulsive interaction and its strength. For single-stranded DNAs, inter-particle separations, sufficient DNA surface densities and suitable salt concentrations, E_r could reach several k_BT per chain. Thus, using multiple systems with constant E_a and varied d_r enabled effective inter-particle potential tuning, providing the environment required achieving crystalline morphologies of nanocrystals assemblies via the thermal pathway [113].

In order to verify the influence of the parameters mentioned above, five sets of structures were designed by varying the length of spacers on two sets of DNA functionalized Au nanocrystals while the linker was kept the same. Particle assembly was carried out at 25 ^{0}C by combining equimolar amounts of the two types of DNA-capped Au nanocrystals in phosphate buffer. The particles were allowed to assemble into aggregates overnight, and the resulting precipitate was collected and transferred in buffer to quartz capillary for thermal treatment where the amorphous assembly was heated to pre-melting temperature followed by heating beyond melting point to disassemble the constituents completely. Reducing the temperature below melting recrystallized the assembly depending upon the combinations of the parameters chosen. It was noted that long flexible spacers (i.e. 35 and 50 bases respectively) showed spontaneous crystallization with remarkable long-range order. In contrast, with shorter or more rigid spacers, the assembly remained amorphous upon cooling. The observed crystallization is the result of specific DNA–DNA interactions, as confirmed by the multiple control experiments with non-complementary DNA-capped nanoparticles or with uncapped particles, none of which exhibited assembly [113].

A number of biomimetic routes have been explored in recent past to prepare nanocrystal superlattices where periodic structures formed using of a large variety of proteins are found extremely useful. In one such example of S-layer proteins, examined very extensively, nanocrystalline superlattices were prepared using a large variety of metal nanocrystals. Efforts were also made to use them for a number of biosensor and other applications.

Proteins found in the bacterial cell surface layer, also known as S-layer, do possess self-assembly features appropriate for precise periodic nanostructuresin Nature [114-116]. S-layer proteins reassemble into two-dimensional arrays on surfaces of a number of materials including silicon, metals, and polymers and interfaces like lipid films or liposomes. The S-layer unit cell repeats at a distance of ~ 10 nm, forming regular arrays of bound molecules and nanocrystals.

The outermost cell surface of a large number of bacteria and archaeacomprises of a S-layer exhibiting oblique, square or hexagonal lattice symmetry with 3–30 nm unit cell forming 5–10 nm thick layer with 2–8 nm diameter pores with negative charges on its inner surface arising due to excess of carboxyl and amino groups and a neutral outer face [117]. These S-layer protein subunits suspend freely once dissolved in a solvent containing guanidine hydrochloride, urea; or by lowering/raising the pH value, or using EDTA, EGTA or cation substitution. After removing these agents, the S-layer protein subunits start reassembly into flat sheets, open-ended cylinders or closed vesicles and during this process, rapid nucleation of the subunits into oligomeric precursors leads to slow

aggregation into larger crystalline arrays. Large-scale domains of crystalline S-layers arrays were observed at the water-air interface within a few hours during recrystallization process. The formation of coherent crystalline arrays on solid substrates, on the other hand, was noted to depend upon the specific proteins involved, conditions of the crystallization solution and surface properties of the substrate. For example, 10–20 μm diameter monocrystalline domains of *B. coagulans* E38-66 were obtained while in case of *B. sphaericus* CCM2177, the domains were of much smaller size. Similarly, hydrophobic substrate surfaces were most often used for crystal growth as noted in case of *B. stearothermophilus* NRS 2004/3a related experiments, but in contrast, large domains of *B. sphaericus* CCM2177 were also formed on especially hydrophilic surfaces [117]. Absorption of ArF-laser radiation in the S-layer protein causing ablation was proposed for using such superlattices as deep UV-photoresist for pattern delineation in micro and nano electronic applications. Because of 4-10 nm thickness of S-layers, which is comparatively much thinner than conventional resists, considerable improvement in edge definitions of submicron structures is expected accordingly. These S-layers were reported as nm-size-templates for the nucleation of inorganic NCs into ordered arrays. For example, CdS andAu NC-superlattices were prepared using such templates [118,119]. A square superlattice, comprising of monodisperse 4-5 nm sized gold NCs with a 12.8 nm repeat distance, was fabricated by exposing S-layer lattice with thiol groups to a tetra-chloroauric (III) acid solution [119]. It was interesting to observe that the shape of these gold NCs resembled the S-layer lattice pores morphology. These experiments were repeated successfully in case of other metal salts like $PdCl_2$, $NiSO_4$, $KPtCl_6$, $Pb(NO_3)_2$ and $K_3Fe(CN)_6$ demonstrating that NC-superlattices were induced by S-layers as templates with a broad range of particle sizes (5–15 nm diameter), ~ 30 nm inter-particle spacing and oblique, square or hexagonal lattice symmetries [117].

Discussion and Conclusions

Considering the recent developments of newer varieties of meso-materials using inorganic, organic, polymeric and biomolecular nanocrystals as building blocks, we are currently passing through a similar situation as it existed almost hundred years ago when high purity bulk materials were prepared using atomic building blocks especially in the area of monocrystalline semiconductors, metals and dielectrics. Extrapolating from the Century old experience further, it is natural to expect another revolution in offing involving the applications of these meso-materials in producing components, devices and systems, which would certainly surpass the capabilities that are presently being covered by the microelectronics technology based counterparts [120]. The coming decade, in near future, is going to witness a strong emergence of smart and intelligent features in overall development of altogether new materials, components and devices. The impact of such a technology that is strongly enabled by better types of nano biosensors and actuators, is expected to be far more profound than what we are experiencing right now in our day-to-day life. A dominating portion of the development will be related to the biomimetic designs incorporating green processes and features to the extent that it would be practically possible. This will lead to reducing the burden on environmental pollution and human health care while attempting to improve the quality of human life as a whole [102].

From the brief descriptions of the subject included in the discussions here, it appears that the basic understanding of the processes like nucleation, growth and morphology control during solution-grown synthesis of a large variety of NCs is slowly reaching to a level where large scale synthesis is clearly foreseen besides attaining other features like mono-dispersion with better than 5% spread in nanocrystal dimensions having stability during storage over a period of a year or more in aqueous and other media [121]. Surface functionalization schemes, having been investigated so far, have shown significant promise for attaching a large number of linkers and spacer ligands chosen from polymeric and biomolecular species facilitating the self-assembly based synthesis of hierarchical structures leading to the superlattices of practically useable dimensions [5,122]. Once again, the role of biomimetic designs and synthesis [117], learnt from Mother Nature including living organisms of various types, will provide significant push in this direction. Use of high precision sophisticated characterization equipment, available today, provides invaluable help in analyzing various experimental observations while trying to understand the underlying mechanism of NC growth via different pathways. This kind of study has facilitated ways for controlling the nanocrystal growth parameters for achieving the targeted features within certain ranges [123].

It is fairly evident from the discussions presented earlier in this review that solution-grown synthesis of nanocrystals is practically much easier to be handled than that in case of bulk material growths using high temperature melts especially in case of inorganic semiconductors and metals [124]. Process instrumentation, handling and measuring devices and tools and the reactor designs and their involved maintenance – all are of stringent nature not available so commonly. On the contrary, solution-grown nanocrystals syntheses need very moderate kind of set-up operating at relatively lower temperatures. Nanocrystal synthesis is noted to very much resemble the biological processes occurring in Nature where the catalytic routes involving enzymes and other biomolecules besides including a large variety of microbial and fungal species appear to be still open to explore in future [124].

There is a necessity to investigate in detail the phytochemical based nanocrystal synthesis of inorganic materials to minimize the use of toxic chemicals following ecofriendly green chemistry routes. However, it is still better to explore using nanocrystals, NPs and branched-NPs synthesized from phytochemicals that are derived from the sustainable natural resources of the different regions. Continuing to examine the future possibilities further, it is quite likely to explore using phytochemicals NC-superlattices based preparations for targeted drug delivery in different forms suitable for drug administration involving optimal dosages and minimizing wastages and thus reducing the overall cost. Chemical conjugations of a number of different drug molecules to a suitable herbal NC-superlattice might prove to be a valuable replacement of the existing alternative natural medicines with much better efficacies involving even a combination of synthetic molecular and natural herbal drugs in due course of time. The advantages of such an integrated system of medicines will have immense benefits once properly understood and developed on the basis of sound theoretical basis.

Newer applications of nanocrystal-based superlattices may be explored using their unique tunable optical propertiesof these building blocks [125,126]. It is quite possible to have optimized structures appropriate for improving the solar radiation absorption leading to better efficiencies of solar photovoltaic devices at reduced cost especially in case of dye sensitized solar cells. Early experiments, conducted using metal nanocrystals, have already shown the positive results in this direction. However, still better improvements are expected using more appropriate designs of nanocrystals and their compositionskeeping in view the optimal properties of nanocrystals. Self-assembly of nanocrystals in organized forms is quite likely to provide low-cost process for surface modifications to incorporate number of feature that are currently being observed in a lesser controlled manner using some sort of colloidal solution of nanocrystals [127]-[132]. Self-assembly of nanocrystals at slid-liquid interface during substrate dipping into the colloidal solution of nanocrystals in suitable solvent will certainly be a very cost effective way of achieving reproducible processes of thin film coatings in future [103,104,122,124,133]. Compared withthe sophisticated methods of thin film coating developed for microelectronic devices and circuit fabrications, the current method of dip coating in any form of high precision movements and automation is still going to be much simpler and of low cost. This could very effectively and efficiently be extended to realize flexible electronicswhere polymeric substrates may be used with added flexibility and cost reduction [134].

The discussion regarding future possibilities of nanocrystals in active device fabrications are taken up elsewhere [135]. It suffices to state that many newer applications, not yet conjectured till date, will be possible to realize soon. The overall contributions of nanocrystals and meso-materials will go beyond the expectations of today. Only time will tell the exact impact of the much-awaited revolution in the field of nanocrystals and related materials.

ACKNOWLEDGEMENT

The author gratefully acknowledges support and encouragement extended by the Management Council and Academic Staff, KPGI, Technical Campus, Agra, India. In connection with preparing the manuscript, various concepts, developed over past few decades forimproving the material characteristics for device applications, which were elaborately discussed in various excellent reviewsand particularly the current status of the device-related developments reported in the recent publications, have been used with due acknowledgements of the excellent contributions made by the respective authors. The references provided here, though, may not be exhaustive, but the contributions made by numerous researchers in this area are all duly acknowledged, directly or indirectly,

through the references currently included in the text as well as those mentioned in the referred review articles.

REFERENCES

[1] Talapin, D. V., Jong-Soo Lee, M. V. Kovalenko, and E. V. Shevchenko. Prospects of colloidal nanocrystals for electronic and optoelectronic applications. *Chem. Rev. 110* (1)(2010): 389-458; DOI: 10. 1021/cr900137k

[2] Li, J. and Lin-Wang. Shape effects on electronic states of nanocrystals. *Nano Letters 3* (10)(2003): 1357-63; DOI**:** 10.1021/nl034488o

[3] Diaconescu, B., L. A. Padilha, P. Nagpal, B. S. Swartzentruber, and V. I. Klimov. " Measurement of electronic states of PbS nanocrystal quantum dots using scanning tunneling spectroscopy: The role of parity selection rules in optical absorption." Phys. Rev. Lett. 110(2013): 127406.

[4] Yin, Y., and A. P. Alivisatos. " Colloidal nanocrystal synthesis and the organic–inorganic interface." *Nature* 437(2005): 664-70; doi: 10.1038/nature 04165;

[5] Murray, C. B., and C. R. Kagan, and M. G. Bawendi. "Synthesis and characterization of monodisperse nanocrystals and close packed nanocrystal assemblies." Ann. Rev. Mater. Sci, 30(2000): 545–610.

[6] Nguyen, V. S., D. Rouxel, and B. Vincent. "Dispersion of nanoparticles: From organic solvents to polymer solutions."Ultrasonics Sonochemistry21 (1)(2014): 149–153.

[7] Holman, Z. C., and U. R. Kortshagen. " A flexible method for depositing dense nanocrystal thin films: impaction of germanium nanocrystals." Nanotechnology 21(2010): 335302. doi: 10. 1088/0957-4484/21/33/335302

[8] Collier, C. P., T. Vossmeyer, and J. R. Heath. "Nanocrystal Superlattices." Ann. Rev. Phys. Chem. 49(1998): 371-404. DOI: 10.1146/ annurev.physchem.49.1.371

[9] Hu, H., J.-y. Xu, H. Yang, J. Liang, S. Yang, and H. Wu. "Morphology-controlled hydrothermal synthesis of MnCO3 hierarchical superstructures with Schiff base as stabilizer." Mater. Res. Bulletin 46 (2011): 1908-15.

[10] Kumar, S. M., and G. R. Rao. "Novel nanostructured CeO_2 as efficient catalyst for energy and environmental applications." J. Chemical Sciences 126(2)(2014): 361-372.

[11] Zhu, G., C. Bao, Y. Liu, X. Shen, C. Xi, Z. Xu, and Z. Ji. "Self-regulated route to ternary hybrid nanocrystals of Ag–Ag_2S–CdS with near-infrared photoluminescence and enhanced photo thermal conversion." Nanoscale**,** 2014, DOI: 10.1039/C4NR03001J

[12] Markovich, G., C. P. Collier, and J. R. Heath. "Reversible Metal-Insulator Transition in Ordered Metal Nanocrystal Monolayers Observed by Impedance Spectroscopy." Phy. Rev. Lett. 80(17)(1998): 3807.

[13] Mark, J. E., H. R. Allcock, and R. West. Inorganic Polymers. Second Edition. Oxford University Press, 2005.

[14] Ali, D. Phytochemical investigations on the constituents of *LaunaeaNudicaulis* and *Euphorbia Thymipholia* and light harvesting oligomers/polymers via stable free radical polymerization. PhD Thesis submitted to University of Karachi, Pakistan, 2008.

[15] Lee, S. H., D. Heng, W. K. Ng, H. K. Chan, and R. B. Tan. "Nano spray drying: a novel method for preparing protein nanoparticles for protein therapy." Int. J. Pharm. 403(1-2)(2011): 192-200. doi: 10.1016/j.ijpharm. 2010.10.012. Epub 2010 Oct 15.

[16] Kittel, C. Introduction to Solid State Physics, 8th Edition, John Wiley & Sons, Inc., 2004.

[17] Markovich, G., C. P. Collier, S. E. Henrichs, F. Remacle, R. D. Levine, and J. R. Heath."Architectonic quantum dot solids." Acc. Chem. Res. 32(1999):415-23.

[18] Alvarez[1], M. M., J.T. Khoury, T.G. Schaaff, M. Shafigullin, I. Vezmar, R.L. Whetten. "Critical sizes in the growth of Au clusters." Chem. Phy. Lett.266(1-2)(1997): 91–98.

[19] Vetter, T., M. Iggland, D. R. Ochsenbein, F. S. Hänseler, and M. Mazzotti. "Modeling Nucleation, Growth, and Ostwald Ripening in Crystallization Processes: A Comparison between Population Balance and Kinetic Rate Equation." *Cryst.*

Growth Des. 13 (11)(2013): 4890-905. DOI: 10.1021/cg4010714

[20] Hussain, I., S. Graham, Z. Wang, B. Tan, D. C. Sherrington, S. P. Rannard, A. I. Cooper, and M. Brust. "Size-controlled synthesis of near-mono dispersed gold nanoparticles in the 1-4 nm range using polymeric stabilizers." J. Am. Chem. Soc. 127(2005): 16398-9.

[21] Rong, H., Y. Xiaogang, T. Hongye, G. Feng, C. Daxiang, and G. Hongchen. " Synthesis and characterization of monodisperse CdSe quantum dots in different organic solvents." Front. Chem. China 4(2006): 378–383; DOI 10.1007/ s11458-006-0052-7

[22] Ramanery, F. P., A. A. P. Mansur, and H. S. Mansur. "Synthesis and Characterization of Water-dispersed CdSe/CdS Core-shell Quantum Dots Prepared via Layer-by-layer Method Capped with Carboxylic-functionalized Poly (Vinyl Alcohol)." Materials Research. 17(Suppl. 1)(2014): 133-140 DDOI: http://dx.doi.org/10.1590/S1516-14392014005000060

[23] York, P. " Strategies for particle design using supercritical fluid technologies." Pharm. Sci. Technolo. Today. 2(11)(1999): 430-440.

[24] Reverchon, E. Supercritical antisolvent precipitation of micro- and nano-particles. J. Supercrit. Fluids 15(1999): 1-21.

[25] Jung, J., and M Perrut. " Particle designs using supercritical fluids." J. Supercrit. Fluids 20(2001): 179-219

[26] Kawashima, Y. "Nanoparticulate systems for improved drug delivery." Adv. Drug Deliv. Rev. 47(2001): 1-2.

[27] Shariati, A., and C. J. Peters. "Recent developments in particle design using supercritical fluids." Curr. Opin. Solid State Mater. Sci. 7(2003): 371-383.

[28] Vemavarapu, C., M. J. Mollan, M. Lodaya, and T. E. Needham. " Design and process aspects of laboratory scale SCF particle formation systems." Int. J. Pharm. 292(2005): 1-16.

[29] Weber, M., and M. C. Thies. Understanding the RESS Process. In, Sun, Y-P, Editor, Supercritical fluid technology in materials science and engineering: synthesis, properties, and applications, CRC press, New York; pp. 387-437, 2002.

[30] Blasig, A., C. Shi, R. M. Enick, and M. C. Thies. "Effect of concentration and degree of saturation on RESS of a CO_2-soluble fluoropolymer." Ind. Engg. Chem. Res. 41(2002): 4976-83.

[31] Sane, A., and M. C. Thies. " Effect of material properties and processing conditions on RESS of poly(L-lactide)." J. Supercrit. Fluids 40(2007): 134-3.

[32] Sun, Y. P., H. W. Rolling, J. Bandara, J. M. Meziani, and C. E. Bunker. "Preparation and processing of nanoscale materials by supercritical fluid technology." In: Sun, Y. P., Editor. Supercritical fluid technology in materials science and engineering: synthesis, properties, and applications. NewYork: Marcel Dekker: pp. 491–576, 2002.

[33] Meziani, M. J., P. Pathak, R. Hurezeanu, M. C. Thies, R. M. Enick, and Y.-P. Sun. "Supercritical-fluid processing technique for nanoscale polymer particles. Angew. Chem. Int. Ed. 43(2004): 704-707. DOI: 10.1002/anie. 200352834

[34] Vehring, R. "Pharmaceutical particle engineering via spray drying."Pharm. Res. 25(5)(2008): 999-1022.

[35] Schuck, P., A. Dolivet, S. Méjean, P. Zhu, E. Blanchard, and R. Jeantet. " Drying by desorption: A tool to determine spray-drying parameters. J. Food Eng. 94(2009): 199-204.

[36] Arpagaus, C., N. Schafroth, and M. Meuri. " Laboratory Scale Spray Drying of Lactose: A Review." Respir. Drug Deliv. Eur. 2(2009): 269-74.

[37] Li, X., N. Anton, C. Arpagaus, F. Belleteix, T. F. Vandamme. " Nanoparticles by spray drying using innovative new technology: The Büchi Nano Spray Dryer B-90." J. Controlled Release, 147(2010): 304-310.

[38] Meng, Q., H. Xin, Y. Zhang, Y. Huang, X. Yi, Y. Sun, S. Zhong, and X. Li. "Catalytic Dehydration of Ethanol to Ethylene Over Steam-Treated ZSM-5 Zeolites." Science of Advanced Materials, 7(11)(2015): 2343-2351(9)

[39] Nie, Q., W. B. Tan, and Y. Zhang. "Synthesis and characterization of monodisperse chitosan nanoparticles with embedded quantum dots." Nanotechnology 17(1): 140-4.

[40] Su, Y. T., G. Y. Lan, W. Y. Chen, and H. T. Chang. "Detection of copper ions through recovery of the fluorescence of DNA templated copper/silver nanoclusters in the presence of mercaptopropionic acid." Anal. Chem. 82 (2010): 8566-72.

[41] Hines, M. A. and G.D. Scholes. "Colloidal PbS Nanocrystals with Size-Tunable Near-Infrared Emission: Observation of Post-Synthesis Self-Narrowing of the Particle Size Distribution." Advanced Materials 15(21)(2003): 1844-49; DOI: 10.1002/adma.200305395

[42] Protière, M., N. Nerambourg, O. Renard, and P. Reiss. "Rational design of the gram-scale synthesis of nearly monodisperse semiconductor nanocrystals." Nanoscale Res Lett. 6(1)(2011): 472; doi: 10.1186/1556-276X-6-472

[43] Yan, Y., Y. Zhang, G. Meng, L. Zhang. "Synthesis of ZnO nanocrystals with novel hierarchical structures via atmosphere pressure physical vapor deposition method." J. Crystal Growth 294(2-4)(2006): 184-90.

[44] Rauda, I. E., R. Buonsanti, L. C. Saldarriaga-Lopez, K. Benjauthrit, L. T. Schelhas, M. Stefik, V. Augustyn, J. Ko, B. Dunn, U. Wiesner, D. J. Milliron, and S. H. Tolbert. "General method for the synthesis of hierarchical nanocrystal-based mesoporous materials**."** *ACS Nano 6* (7)(2012): 6386-99;DOI: 10. 1021/nn302789r

[45] Whang, D., S. Jin, Y. Wu, and C. M. Liebe. " Large-scale hierarchical organization of nanowire arrays for integrated nano systems." Nano Lett. 3(9)(2003): 1255-9.

[46] Zhang, H., Q. Zhu, Y. Zhang, Y. Wang, L. Zhao and B. Yu. "One-Pot synthesis and hierarchical assembly of hollow Cu_2O microspheres with nano crystals-composed porous multi shell and their gas-sensing properties." Adv. Func. Mater. 17(15)(2007): 2766-71. DOI: 10.1002/adfm.200601146

[47] Miszta, K. J. de Graaf, G. Bertoni, D. Dorfs, R. Brescia, S. Marras, L. Ceseracciu, R. Cingolani, R. van Roij, M. Dijkstra and L. Manna. "Hierarchical self-assembly of suspended branched colloidal nanocrystals into superlattice structures." *Nature Materials* 10(2011):872–876; doi: 10.1038/nmat3121

[48] Sabba**,** D., S. Agarwala**,** S. S Pramana **and** S. Mhaisalkar. "A maskless synthesis of TiO_2-nanofiber-based hierarchical structures for solid-state dye-sensitized solar cells with improved performance." *Nanoscale Res. Lett.* 9 (2014): 14; doi: 10.1186/1556-276X-9-14

[49] Zhang, H., and L. Qi. "Low-temperature, template-free synthesis of wurtzite ZnS nanostructures with hierarchical architectures." Nanotechnology 17(2006): 3984-8 doi: 10.1088/0957-4484/17/15/063

[50] Shen, X., Z. Li, Y. Cui, and Y. Pang. " Glutathione-assisted synthesis of hierarchical PbS via hydrothermal degradation and its application in the pesticide bio sensing." Int. J. Electrochem. Sci. 6(2011): 3525-35

[51] Nosheen, F., Z. Zhang, G. Xiang, B. Xu, Y. Yang, F. Saleem, X. Xu, J. Zhang, and X. Wang. " Three-dimensional hierarchical Pt-Cu superstructures." Nano Res. Just Accepted; (2014); DOI: 10.1007/s12274-014-0565-1

[52] Alvarez[2], M. M., J. T. Khoury, T. G. Schaaff, M. N. Shafigullin, Vezmar, and R. L. Whetten. "Optical absorption spectra of nanocrystal gold molecules." J. Phys. Chem. B 101(1997): 3706-3712.

[53] Koole, R., G. Allan, C. Delerue, A. Meijerink, D. Vanmaekelbergh, and A. J. Houtepen. " Optical Investigation of Quantum Confinement in PbSe NCs at Different Points in the Brillouin Zone." small 4(1)(2008): 127-133; DOI: 10.1002/smll. 200700632

[54] Tao, A. R., S. Habas, and P. Yang. "Shape control of colloidal metal nanocrystals." small 4(3)(2008): 310-25; DOI: 10.1002/smll. 200701295

[55] Dorokhin, D. V. "Surface engineered quantum dots in photo-electro-chemistry and supramolecular assembly." Doctoral Thesis, 2010.

[56] Sperling, R. A., and W. J. Parak. "Surface modification, functionalization and bioconjugation of colloidal inorganic nanoparticles." *Phil. Trans. R. Soc. - A* 368(2010): 1333-83.

[57] Zhang, Y., and A. Clapp. (**2011**). "Overview of stabilizing ligands for biocompatible quantum dot nanocrystals." Sensors 11(2011): 11036-11055; doi:10.3390/s111211036

[58] Wei, D., W. Sun, W. Quian, Y. Ye, and X. Ma. " Synthesis of chitosan based silver nanoparticle and their antibacterial activity." Carbohydr. Res. 344(17)(2009): 2375-82.

[59] Wei, D., and W. Qian. " Facile synthesis of Ag and Au nanoparticles utilizing chitosan as a mediator agent." Colloids Surf.

B Biointerfaces 62(1)(2008): 136-42.

[60] Potara, M., D. Maniu, and S. Astilean. "The synthesis of biocompatible and SERS-active gold nanoparticles using chitosan." Nanotechnology, 20(31)(2009), article id. 315602.

[61] Mata, Y. N., E. Torres, M.L. Blázquez, A. Ballester, F. González, J.A. Munoz. "Gold(III) biosorption and bioreduction with the brown alga Fucus vesiculosus." J. Hazard. Mater. 166(2-3)(2009): 612-8.

[62] Nadkarni, V. D., A. Pervin, and R.J. Linhardt. " Directional Immobilization of Heparin Onto Beaded Supports." Anal Biochem, 222(1)(1994): 59-67.

[63] Kemp, M. M., A. Kumar, S. Mousa, T.-J. Park, P. Ajayan, N. Kubotera,S. Mousa, and R. J. Linhardt. "Synthesis of Gold and Silver Nanoparticles Stabilized with Glycosaminoglycans having Distinctive Biological Activities." Biomacromolecules. 10(3)(2009): 589–595; doi: 10.1021/bm801266t

[64] Cai, J., S. Kimura, M. Wada and S. Kuga. "Nanoporous Cellulose as Metal Nanoparticles Support." *Biomacromolecules* 10 (1)(2009): 87-94. DOI: 10.1021/bm800919e

[65] Saha, S., A. Pal, S. Kundu, S. Basu, and T. Pal. " Photochemical green synthesis of calcium-alginate-stabilized Ag and Au nanoparticles and their catalytic application to 4-nitrophenol reduction." Langmuir 26(4)(2010): 2885–93.

[66] Ahmad, A., P. Mukherjee, S. Senapati, D. Mandal, M.I. Khan, R. Kumar, M. Sastry. "Extracellular biosynthesis of silver nanoparticles using the fungus *Fusarium oxysporum."* Colloids Surf. B Biointerfaces, 28(4)(2003): 313-8.

[67] Mukherjee, P., S. Senapati, D. Mandal, A. Ahmad, M. I. Khan, R. Kumar, and M. Sastry. Extracellular Synthesis of Gold Nanoparticles by the Fungus *Fusarium oxysporum.* ChemBioChem, 3(5)(2002): 461-3. DOI: 10.1002 /1439-7633(20020503)3:5<461::AID-CBIC461>3.0.CO;2-X

[68] Lengke, M. F., M. E. Fleet, and G. Southam. "Biosynthesis of silver nanoparticles by filamentous cyanobacteria from a silver(I) nitrate complex." Langmuir 23(5)(2007): 2694-9.

[69] Klaus, T., R. Joerger, E. Olsson, and C. G. Granqvist. " Silver-based crystalline nanoparticles, microbially fabricated." PNAS, USA 96(24)(1999): 13611-4.

[70] Parikh, R. Y., R. Ramanathan,P. J. Coloe,S. K. Bhargava,M. S. Patole,Y. S. Shouche, andV. Bansal. "Genus-Wide Physicochemical Evidence of Extracellular Crystalline Silver Nanoparticles Biosynthesis by morganella spp." ChemBioChem, 9(9)(2008): 1415-22. DOI: 10.1371/journal.pone.0021401

[71] Krpetic, Z., G. Scarı`, E. Caneva, G. Speranza, and F. Porta. "Gold Nanoparticles Prepared Using Cape Aloe Active Components." Langmuir 25(13)(2009): 7217-21.

[72] Kasthuri, J., S. Veerapandian, and N. Rajendran. "Biological synthesis of silver and gold nanoparticles using apiin as reducing agent." Colloids Surf. B Biointerfaces. 68(1)(2009): 55-60. http://dx.doi.org /10.1016/j.colsurfb.2008.09.021

[73] Khaleel Basha, S., R. G. K, Manikandan, J. S. Ahn, E. Y. Bae, and G. Singaravelu." Phytochemical mediated gold nanoparticles and their PTP 1B inhibitory activity." Colloids Surf. B Biointerfaces. 75(2)(2010): 405-9; doi: 10.1016/j.colsurfb.2009.09.008.

[74] Shukla, R., S. K. Nune, N. Chanda, K. Katti, S. Mekapothula, R. R. Kulkarni, W. V. Welshons, R. Kannan, and K. V. Katti. "Soybeans as a Phytochemical Reservoir for the Production and Stabilization of Biocompatible Gold Nanoparticles." Small 4(9)(2008): 1425-36; DOI: 10. 1002/smll.200800525

[75] Vivekanandhan, S., M. Misra, A. K. Mohanty. "Biological Synthesis of Silver Nanoparticles Using *Glycine max*(Soybean) Leaf Extract: An Investigation on Different Soybean Varieties." J. Nanoscience and Nanotechnology 9(12)(2009): 6828-33.

[76] Philip, D. "Biosynthesis of Au, Ag and Au-Ag nanoparticles using edible mushroom extract."Spectrochimica Acta - Part A: Molecular and Biomolecular Spectroscopy, 73(2)(2009): 374-381.

[77] Armendariz, V., I. Herrera, J. peralta-videa, M. J. Yacaman, H. Troiani, P. Santiago, and J. L Gardea-Torresdey."Size controlled gold nanoparticle formation by Avena sativa biomass: use of plants in nanobiotechnology." J. Nanoparticle. Res. 6(4) (2004): 377-382; DOI: 10.1007/s11051-004-0741-4

[78] Ghodake, G. S., N.G. Deshpande, Y.P. Lee, and E.S. Jin. "Pear fruit extract-assisted room-temperature biosynthesis of gold nanoplates." Colloids Surf. B Biointerfaces, 75 (2)(2010): 584-9.

[79] Niemeyer, C. M. "Nanoparticles, Proteins, and Nucleic Acids: Biotechnology Meets Materials Science." Angew. Chem. Int. Ed. 40(2001): 4128-58; DOI: 10.1002/1521-3773(20011119) 40:22<4128::AID-ANIE4128>3.0.CO;2-S

[80] Broderick, J. B., M. J. Natan, T. V. O'Halloran , R. P. Van Duyne. "Evidence for retention of biological activity of a non-heme iron enzyme adsorbed on a silver colloid: A surface-enhanced resonance Raman scattering study." *Biochemistry*32 (50)(1993): 13771-6. DOI: 10.1021/ bi00213a003

[81] Macdonald, I. D. G., and W. E. Smith. "Orientation of Cytochrome *c* Adsorbed on a Citrate-Reduced Silver Colloid Surface." *Langmuir*12 (3)(1996): 706–713. DOI: 10.1021/la950256w

[82] Rospendowski, B. N., K. Kelly, C. R. Wolf, and W. E. Smith. " Surface-enhanced resonance Raman scattering from cytochromes P-450 adsorbed on citrate-reduced silver sols." *J. Am. Chem. Soc.* 113 (4)(1991): 1217-25. **DOI:** 10.1021/ja00004a023

[83] Safer, D., L. Bolinger, J. S. Leigh Jr. " Undecagold clusters for site-specific labeling of biological macromolecules: simplified preparation and model applications." J. Inorg. Biochem. 26(1986): 77-91.

[84] Dubertret, B., M. Calame and A. J. Libchaber. "Single-mismatch detection using gold-quenched fluorescent oligonucleotides." *Nature Biotechnology* 19(2001): 365–370; doi: 10.1038/86762

[85] Alivisatos, P. A., K. P. Johnsson, X. Peng, T. E. Wilson, C. J. Loweth, M.P Bruchez Jr, and P. G. Schultz. "Organization of 'nanocrystal molecules' using DNA." *Nature* 382(1996): 609-611; doi: 10.1038/382609a0

[86] Dameron, C. T., R. N. Reese, R. K. Mehra, A. R. Kortan, P. J. Caroll, M. L. Steigerwald, L. E. Brus, and D. R. Winge. " Biosynthesis of cadmium sulphide quantum semiconductor crystallites." *Nature* 338(1989): 596 - 597; doi: 10.1038/338596a0

[87] Bae, W., R. Abdullah, D. Henderson, and R. K. Mehra. " Characteristics of Glutathione-Capped ZnS Nanocrystallites." Biochem. Biophys. Res. Comm. 237(1)(1997): 16 - 23.

[88] Kho, R., C. L. Torres-Martínez, and R. K. Mehra. "A Simple Colloidal Synthesis for Gram-Quantity Production of Water-Soluble ZnS Nanocrystal Powders." J. Colloid. Interf. Sci.227(2)(2000): 561-6.

[89] Bruchez, M. Jr, M. Moronne, P. Gin, S. Weiss, A. P. Alivisatos. " Semiconductor nanocrystals as fluorescent biological labels." Science 281(5385)(1998): 2013-6.

[90] Drexler, K. E. "Molecular engineering: An approach to the development of general capabilities for molecular manipulation." PNAS USA, 78(1981): 5275 -78.

[91] Seeman, N. C., and N. R. Kallenbach. " Design of immobile nucleic acid junctions." Biophys J. 44(2)(1982): 201–209.doi: 10.1016/S0006-3495(83)84292-1

[92] Drexler, K. E. Nanosystems: Molecular Machinery, Manufacturing and Computation. Wiley, New York, 1992.

[93] Seeman, N. C. " DNA engineering and its application to nanotechnology." *Trends in biotechnology* 17(11)(1999): 437-443.

[94] Niemeyer, C. M. " Self-assembled nanostructures based on DNA: towards the development of nanobiotechnology." Curr. Opin. Chem. Biol. 4(2000): 609-18.

[95] Thermo Scientific. Avidin-Biotin Technical Handbook. Text available @ http://www.piercenet.com/files/1601675_AvBi_HB_INTL.pdf

[96] Clapp, A. R., E. R. Goldman, and H. Mattoussi. "Capping of CdSe–ZnS quantum dots with DHLA and subsequent conjugation with proteins." *Nature Protocols* 1(2006): 1258-66. doi: 10.1038/nprot.2006.184

[97] WPR-01. "The structure of DNA and RNA", Chap 6; available @ http://biology.kenyon.edu/courses/biol63/watson_06.pdf

[98] Alivisatos, P. " The use of nanocrystals in biological detection." Nature Biotechnology 22(2004): 47-52; doi:10.1038/nbt927

[99] Pathak, S., M. C. Davidson, and G. A. Silva. "Characterization of the functional binding properties of antibody conjugated quantum dots." *Nano Lett.* 7 (7)(2007): 1839-45; DOI: 10.1021/nl062706i

[100] Gao, X., Lily Yang, John A Petros, F. F. Marshall, J. W. Simons, and S. Nie. " In vivo molecular and cellular imaging with

quantum dots." Curr. Opinion Biotech.16(1)(2005): 63-72.

[101] Ghadiali, J. E.,and M. M. Stevens. "Enzyme-Responsive Nanoparticle Systems." Adv. Mater. 20(22)(2008): 4359-63.DOI: 10.1002/adma.200703158

[102] Cliffel, D. E., B. N. Turner, and B. J. Huffman. "Nanoparticle-based biologic mimetics." Wiley Interdiscip. Rev. Nanomed. Nanobiotechnol. 1(1)(2009): 47-59. doi: 10.1002/wnan.20

[103] Akey, A., C. Lu, L. Yang, and I. P. Herman. "Formation of thick, large-area nanoparticle superlattices in lithographically defined geometries." *Nano Lett.* 10 (4) (2010): 1517-21; DOI: 10.1021/nl100129t

[104] Taheri, S. M., S. Fischer and S. Förster. Routes to Nanoparticle-Polymer Superlattices. Polymers, 3(2011): 662-73.

[105] Blanton, T. N., R. Jagannathan, S. Jagannathan, and R. V. Mehta. US Patent – US 7,097, 902 (2006); Available @ http://patents.com/us-7097902.html

[106] Zhuang, J., H. Wu, Y. Yang, Y. C. Cao. " Supercrystalline Colloidal Particles from Artificial Atoms." *J. Am. Chem. Soc.* 129(46)(2007): 14166-7. doi: 10. 1021/ja076494i

[107] Chen, L., Ju Xu, Justin D. Holmes and M. A. Morris. "A Facile Route to ZnO Nanoparticle Superlattices: Synthesis, Functionalization, and Self-Assembly." *J. Phys. Chem. C* 114 (5)(2010): 2003-11. DOI: 10. 1021/jp9085766

[108] Shevchenko, E. V., D. V. Talapin, N. A. Kotov, S. O'Brien and C. B. Murray. "Structural diversity in binary nanoparticle superlattices." *Nature* 439(2006): 55-59; doi:10.1038/nature04414

[109] Dong, A.,J. Chen,P. M. Vora,J. M. Kikkawa, and C. B. Murray. " Binary nanocrystal superlattice membranes self-assembled at the liquid–air interface." Nature. 466(2010): 474-7; doi: 10.1038/nature09188

[110] Heitmann, J., F. Müller, M. Zacharias, and U. Gösele. "Silicon nanocrystals: Size matters." Advanced Materials 17(7)(2005): 795-803.

[111] Israelachvili, J. N. Intermolecular and Surface Forces; Second Edition; Academic Press: London, 1991.

[112] Tkachenko, A. V. "Morphological Diversity of DNA-Colloidal Self-Assembly." Phys. Rev. Lett. 89(2002): 148303

[113] Nykypanchuk, D., M. M. Maye, D. van der Lelie, and O. Gang. " DNA-guided crystallization of colloidal nanoparticles." *Nature* 451(2008): 549-52; doi:10.1038/nature06560

[114] Pum, D., and U. B. Sleytr. "The application of bacterial S-layers in molecular nanotechnology." *Trends Biotechnol.* 17(1999): 8-12.

[115] Sleytr, U.B., P. Messner, D. Pum, and M. Sára. "Crystalline bacterial cell surface layers (S-layers): from supramolecular cell structure to biomimetics and nanotechnology." *Angew. Chem. Int. Ed. Engl.* 38(1999): 1034-54.

[116] Sleytr, U. B., M. Sara, and D. Pum. In SupramolecularPolymerization, Editor, A. Ciferri, New York: Marcel Dekker, 2000

[117] Pum, D., A. Neubauer, E. Györvary, M. Sára, and U. B. Sleytr. "S-layer proteins as basic building blocks in a biomolecular construction kit." *Nanotechnology* 11(2000):100-107. doi: 10.1088/0957-4484/11/2/310

[118] Shenton, W., D. Pum, U. B. Sleytr, and S. Mann. " Synthesis of cadmium sulphide superlattices using self-assembled bacterial S-layers." *Nature* 389(1997): 585-7.

[119] Dieluweit, S., D. Pum, and U. B. Sleytr. "Formation of a gold superlattice on an S-layer with square lattice symmetry." Supramol. Sci. 5(1998): 15–19.

[120] Lecture-40. "Microelectronics Technology in 21st Century." EECS40 Lectures. Text available @ http://www-inst.eecs.berkeley.edu/~ee40/fa03/lecture.html

[121] Chan, E. M., C. Xu, A. W. Mao, G. Han, J. S. Owen, B. E. Cohen, D. J. Milliron. " Reproducible, high-throughput synthesis of colloidal nanocrystals for optimization in multidimensional parameter space." Nano Lett. 10(5)(2010): 1874-85. doi: 10.1021/nl100669s.

[122] Eah, S.-K. "A very large two-dimensional superlattice domain of monodisperse gold nanoparticles by self-assembly." J. Mater. Chem.21(2011)**:** 16866-8. DOI: 10.1039/C1JM11671A

[123] Woehl,T. J., J. E. Evans, I. Arslan, W. D. Ristenpart, and N. D. Browning. "Direct *in situ* determination of the mechanisms

controlling nanoparticle nucleation and growth." ACS Nano. 6(10)(2012): 8599-610.doi: 10.1021/nn303371y

[124] Mei, T., and Y. Hu. Optoelectronic Devices and Properties, O. Sergiyenko (Editor), 2011. Available from: http://www.intechopen.com/books/optoelectronic-devices-and-properties/ synthesis-self-assembly-and-optoelectronic-properties-of-monodisperse-zno-quantum-dots

[125] Smith, A. M., and S. Nie. " Next-generation quantum dots."Nat. Biotechnol. 27(8)(2009): 732-3.doi: 10.1038/nbt0809-732

[126] Alaeian, H., and J. A. Dionne. "Plasmon nanoparticle superlattices as optical-frequency magnetic metamaterials." Optics Express, 20(14)(2012):15781-96; http://dx.doi.org/10.1364 /OE.20.015781

[127] NREL. Research Review 2007 available @ http://www.nrel.gov/docs/fy08osti/42386.pdf

[128] Dong, A.,J. Chen,P. M. Vora,J. M. Kikkawa, and C. B. Murray. " Binary nanocrystal superlattice membranes self-assembled at the liquid–air interface." Nature. 466(2010): 474-7; doi: 10.1038/nature09188

[129] Dalal, V. L., and A. Madhavan. "Alternative designs for nanocrystalline silicon solar cells." J. Non-Crystalline Solids 354(19)(2008): 2403-6. DOI: 10.1016/j.jnoncrysol.2007.09.110

[130] Webber, D. H., and R. L. Brutchey. **"**Nanocrystal ligand exchange with 1,2,3,4-thiatriazole-5-thiolate and its facile in situ conversion to thiocyanate**."** *Dalton Trans. 2012* DOI: 10.1039 /C2DT30197K

[131] Chung, I., B. Lee, J. He, R. P. H. Chang, M. G. Kanatzidis. "All-solid-state dye-sensitized solar cells with high efficiency**."** *Nature* 485: (7399)(2012): 486 DOI: 10.1038/nature11067

[132] Diederich, G., T. O'Connor, P. Moroz, E. Kinder, E. Kohn, D. Perera, R. Lorek, S. Lambright, M. Imboden, and M. Zamkov. **"** Harvesting Solar Energy by Means of Charge-Separating Nanocrystals and Their Solids**."** *J. Visualized Experiments* (66)(2012); DOI: 10.3791/4296

[133] Chane-Ching, J.-Y., F. Cobo, D. Aubert, H. G. Harvey, M. Airiau andA. Corma. "A General Method for the Synthesis of Nanostructured Large-Surface-Area Materials through the Self-Assembly of Functionalized Nanoparticles." Chemistry - A Euro J, 11 (3)(2005): 979-87. DOI: 10.1002/chem.200400535

[134] Tu, H., and Y. Xu. "A silicon-on-insulator complementary metal oxide-semiconductor compatible flexible electronics technology." App. Phys. Lett. 101(2012): 052106.

[135] Ahmad, S. "Device Applications of Band-Structure-Engineered Nanomaterials - Current Status and Future Trend – Review." Int. J. Nanoelectronics and Materials 8 (2015): 129-202

Asymptotic Analysis of Thermoelastic Response in a Functionally Graded Solid Based on L-S Theory

Y. Z. Wang*, J. Xue

Energy and Power Engineering Department, Jiangsu University,Zhenjiang, 212013, China

wyz3701320@ujs.edu.cn

Abstract

This paper is concerned with the thermoelastic response in a functionally graded solid with an analytical method. The governing equations are proposed in the context of Lord-Shulman generalized theory (L-S theory). The Laplace transform techniques and some approximate treatments are employed to have an analytical solution for the thermoelastic response in a semi-infinite solid composed of functionally graded materials, whose boundary is subjected to a sudden thermal shock. Some important phenomena involving finite speed of heat signal are obtained. The comparison with the results for different values of non-homogeneous index is also conducted to evaluate the effect of graded material properties on thermoelastic response.

Keywords

Generalized Thermoelasticity; Functionally Graded Materials; Analytical Solution; Thermal Shock

Introduction

In recent years, functionally graded materials (FGMs), as a new class of intelligent material, has been widely applied in various engineering practices [1]. The analysis of thermoelastic response, especially the prediction of thermal stresses generated in severe temperature environments, is very important to evaluate the lives of FGMs. Many investigations have been conducted in the context of conventional theory of thermoelasticity, however, the conventional theory proposed by Biot [2], predicts an infinite speed of heat propagation, which contradicts physical facts and limits the applicability of these investigations to certain heat conduction. To eliminate this shortcoming, some modified theories admitting a finite propagation speed of heat signal are proposed on different perspective, which are also named as generalized theories of thermoelasticity. The widely applied theories include the L-S theory with one relaxation time [3], G-L theory with two relaxation time [4] and G-N theory with the assumption of no energy dissipation [5].

Within these generalized theories, some thermoelastic problems of FGMs with different boundary conditions have been studied by Bagri and Eslami [6], Darabseh et al. [7], Ghosh and Kanoria [8], where the power law distribution along the spatial position was used to describe the graded material properties. Meanwhile, the exponential distribution with spatial position for material properties was also employed to analyze the thermoelastic interaction in FGMs by Mallik and Kanoria [9], Tokovyy and Ma [10] respectively. Furthermore, Kanoria and Ghosh [11] studied the thermoelastic reponse further for a functionally graded spherically isotropic hollow, where the temperature-dependent properties were also considered. Abbas [12] also solved the thermoelastic interaction in a thick-walled FGM cylinder with the condition that material properties are the function of temperature and graded in the radial.

Since the complexity of the solution for governing equations with variable material properties, which are nonlinear forms in general cases, the theoretical treatment is very difficult and the closed-form solutions is rare in previous investigations [6-12]. Recently, an asymptotic approach [13], based on the Laplace transform and its limit theorem, has been introduced to solve some generalized thermoelastic problems [14, 15]. The asymptotic solutions with closed form can be obtained by this asymptotic approach, which is very effective to the problems involving short thermal duration, such as thermal shock, and is very convenient to evaluate thermo-mechanical properties of

2226-4523/16/01 035-6 © 2016 DEStech Publications, Inc.
doi:10.12783/ijmsci.2016.0601.02

FGMs in severe circumstances.

In this paper, the thermoelastic interaction in a functionally graded solid is studied with this asymptotic approach [13-15]. The governing equations of FGMs are derived in the context of L-S theory, where the exponentially distribution along the spatial position is used to describe the graded material properties. The closed-form solutions for a special problem of a semi-infinite functionally graded solid with the boundary subjected to a sudden thermal shock are derived. Utilizing these solutions, the propagation of each wave, the distributions of the displacement, temperature and stresses, and the variation of each distribution at different non-homogeneous index are obtained and plotted.

Formulation of the Problem

Due to the L-S theory, the governing equations of FGMs in absence of body forces and heat generation can be expressed as

$$\sigma_{ij} = \lambda\gamma_{kk}\delta_{ij} + 2\mu\gamma_{ij} - \beta\theta\delta_{ij}, \tag{1}$$

$$\rho\ddot{u}_i = \sigma_{ij,j}, \tag{2}$$

$$\left[kT_{,i}\right]_{,i} = \rho c_p\left(\tau_0\ddot{T} + \dot{T}\right) + T_0\beta\left(\tau_0\ddot{\gamma}_{kk} + \dot{\gamma}_{kk}\right). \tag{3}$$

where u_i are the components of the displacement vector, σ_{ij} are the components of the stress tensor, $\gamma_{ij} = \left(u_{i,j} + u_{j,i}\right)/2$ are the components of the strain tensor, $\theta = T - T_0$ is the increment temperature, T is the absolute temperature, T_0 is the reference temperature, ρ is the mass density, k is the thermal conductivity, c_p is the specific heat at constant strain, $\beta = \left(3\lambda + 2\mu\right)\alpha_T$ is the thermal-mechanical coefficient, α_T is the coefficient of linear thermal expansion, λ and μ are the Lame's constants, and τ_0 is the thermal relaxation time constant defined in L-S theory. Meanwhile, the superscript dot $(\cdot)$ and the subscript comma $(,)$ denote the derivatives respect to the time t and coordinates $x_i\left(i = 1,2,3\right)$, respectively.

With the effects of functionally graded solid, the parameters ρ, λ, μ, β, c_p and k are no longer constant but become space-dependent. Thus, we use $\rho_0 f\left(x_z\right)$, $\lambda_0 f\left(x_z\right)$, $\mu_0 f\left(x_z\right)$, $\beta_0 f\left(x_z\right)$, $c_{p_0} f\left(x_z\right)$ and $k_0 f\left(x_z\right)$ to replace, respectively, in which ρ_0, λ_0, μ_0, β_0, c_{p_0} and k_0 are assumed to be constants and $f\left(x_z\right)$ is a given non-dimensional function of space variable $x_z\left(z = 1,2,3\right)$.

We now considered a semi-infinite solid composed of FGMs, whose boundaries are traction free and keep the uniform temperature T_0 initially. For time $t = 0$ the surface of boundary $x = 0$ is suddenly raised to a constant temperature T_1.

From the physics of the problem, it is clear that all the physical quantities will depend on x and t only. Thus, the displacement vector has the components:

$$u_x = u\left(x,t\right),\ u_y = u_z = 0. \tag{4}$$

Substituting these displacement vectors (4) into above equations in order and assuming $f\left(x\right) = e^{\kappa x}$, we have

$$\sigma_{xx} = e^{\kappa x}\left[\left(\lambda_0 + 2\mu_0\right)u_{,x} - \beta_0\theta\right], \tag{5}$$

$$\rho_0\ddot{u} = \left(\lambda_0 + 2\mu_0\right)u_{,xx} - \beta_0\theta_{,x} + \kappa\left[\left(\lambda_0 + 2\mu_0\right)u_{,x} - \beta_0\theta\right], \tag{6}$$

$$T_{,xx} + \kappa T_{,x} = a_0\left(\tau_0\ddot{T} + \dot{T}\right) + \frac{T_0\beta_0}{k_0}\left(\tau_0\ddot{u}_{,x} + \dot{u}_{,x}\right). \tag{7}$$

where κ is a non-dimensional constant indicating the non-homogeneity of FGMs, $a_0 = \rho_0 c_{p_0}/k_0$ is the thermal viscosity constant.

Asymptotic Solutions of the Problem

General Solution in the Physical Domain

For simplicity, some following non-dimensional variables are introduced as follows

$x^* = a_0 v_e x$, $t^* = a_0 v_e^2 t$, $\tau_0^* = a_0 v_e^2 \tau_0$, $k^* = k/a_0 v_e$, $u^* = a_0 v_e (\lambda_0 + 2\mu_0) u/\beta_0 T_0$, $\theta^* = \theta/T_0$, $\sigma_{xx}^* = \sigma_{xx}/\beta_0 T_0$.

Substituting these non-dimensional variables into above equations (5)-(7) and dropping the asterisks for convenience, we have

$$\sigma_{xx} = e^{\kappa x}\left(u_{,x} - \theta\right), \tag{8}$$

$$\ddot{u} = u_{,xx} - \theta_{,x} + \kappa\left(u_{,x} - \theta\right), \tag{9}$$

$$\theta_{,xx} + \kappa\theta_{,x} = \tau_0\ddot{\theta} + \dot{\theta} + \vartheta\left(\tau_0\ddot{u}_{,x} + \dot{u}_{,x}\right), \tag{10}$$

where $v_e = \sqrt{(\lambda_0 + 2\mu_0)/\rho_0}$ is the speed of thermal elastic wave, and $\vartheta = T_0\beta_0^2/a_0 k_0(\lambda_0 + 2\mu_0)$ is the thermoelastic coupling constant.

Applying the Laplace transform for the both sides of Eqs. (8)-(10), then we have

$$\bar{\sigma}_{xx} = e^{\kappa x}\left(\bar{u}_{,x} - \bar{\theta}\right), \tag{11}$$

$$s^2\bar{u} = \bar{u}_{,xx} - \bar{\theta}_{,x} + \kappa\left(\bar{u}_{,x} - \bar{\theta}\right), \tag{12}$$

$$\bar{\theta}_{,xx} + \kappa\bar{\theta}_{,x} = \tau_0 s^2\bar{\theta} + s\bar{\theta} + \vartheta\left(\tau_0 s^2\bar{u}_{,x} + s\bar{u}_{,x}\right). \tag{13}$$

Eliminating term $\bar{u}$ and $\bar{\theta}$ separately by combining Eq. (12) and Eq. (13) results in

$$\frac{\mathrm{d}^4\phi_i}{\mathrm{d}x^4} + 2\kappa\frac{\mathrm{d}^3\phi_i}{\mathrm{d}x^3} + \left[\kappa^2 - s^2 - (1+\vartheta)\left(\tau_0 s^2 + s\right)\right]\frac{\mathrm{d}^2\phi_i}{\mathrm{d}x^2} - \kappa\left[s^2 + (1+\vartheta)\left(\tau_0 s^2 + s\right)\right]\frac{\mathrm{d}\phi_i}{\mathrm{d}x} + s^2\left(\tau_0 s^2 + s\right)\phi_i = 0, \tag{14}$$

where $\phi_i\,(i = 1,2)$ represent term $\bar{u}$ and $\bar{\theta}$, respectively.

The general solutions of Eq.(14) can be expressed as

$$\phi_i = A_{1i}(s)\exp(R_1 x) + B_{1i}(s)\exp(R_2 x) + C_{1i}(s)\exp(-R_1 x) + D_{1i}(s)\exp(-R_2 x), \tag{15}$$

where $R_{1,2}^2$ are the roots of following characteristic equation

$R^4 + 2\kappa R^3 + \left[\kappa^2 - s^2 - (1+\vartheta)\left(\tau_0 s^2 + s\right)\right]R^2 - \kappa\left[s^2 + (1+\vartheta)\left(\tau_0 s^2 + s\right)\right]R + s^2\left(\tau_0 s^2 + s\right) = 0$, $A_{1i}(s)$, $B_{1i}(s)$, $C_{1i}(s)$ and $D_{1i}(s)$ are coefficients depending on parameter s and are determined by the given boundary conditions.

Here the following non-dimensional boundary conditions on the boundary plane $x = 0$ are introduced

$$\theta(0,t) = \theta_0 H(t),\ \sigma_{xx}(0,t) = 0, \tag{16}$$

where $H(t)$ is the Heaviside unit function and $\theta_0 = (T_1 - T_0)/T_0$ is a non-dimensional constant.

Applying the Laplace transform to the above condition (16), we have

$$\bar{\theta}(0,s) = \theta_0/s,\ \bar{\sigma}_{xx}(0,s) = 0. \tag{17}$$

Substituting these boundary conditions in general solutions (15) and stress component expression (11), and considering the bounded solutions with large x for an unbounded problem, the general solutions for u, θ and σ_{xx} in the physical domain can be obtained as

$$\bar{u} = \frac{(\kappa - R_1)\theta_0\exp(-R_1 x)}{(R_2 - R_1)\left[\kappa - (R_2 + R_1)\right]s} - \frac{(\kappa - R_2)\theta_0\exp(-R_2 x)}{(R_2 - R_1)\left[\kappa - (R_2 + R_1)\right]s}, \tag{18}$$

$$\bar{\theta}=\frac{\left(R_1^2-s^2-\kappa R_1\right)\theta_0\exp\left(-R_1x\right)}{\left(R_2-R_1\right)\left[\kappa-\left(R_2+R_1\right)\right]s}-\frac{\left(R_2^2-s^2-\kappa R_2\right)\theta_0\exp\left(-R_2x\right)}{\left(R_2-R_1\right)\left[\kappa-\left(R_2+R_1\right)\right]s}, \tag{19}$$

$$\bar{\sigma}_{xx}=\frac{s\theta_0\exp\left(\kappa x\right)\exp\left(-R_1x\right)}{\left(R_2-R_1\right)\left[\kappa-\left(R_2+R_1\right)\right]}-\frac{s\theta_0\exp\left(\kappa x\right)\exp\left(-R_2x\right)}{\left(R_2-R_1\right)\left[\kappa-\left(R_2+R_1\right)\right]}. \tag{20}$$

General Solutions in the Time Domain

Since the complicated expressions of roots $R_i\left(i=1,2\right)$ contained in these transform solutions, some approximate treatment for roots R_i has been conducted by the asymptotic approach [13-15], where the limit theorem of Laplace transform is used to obtain the following expressions:

$$R_{1,2}=k_{1,2}s+m_{1,2}, \tag{21}$$

where $k_{1,2}=\left[\frac{1+\tau_0+\vartheta\tau_0\pm\sqrt{a_1}}{2}\right]^{1/2}$, $m_{1,2}=\frac{1+\vartheta\pm\sqrt{a_1}/b_1}{4k_{1,2}}-\frac{\kappa}{2}$, $a_1=\left(1+\tau_0+\vartheta\tau_0\right)^2-4\tau_0$, and $b_1=\left(1+\vartheta\right)\tau_0+\vartheta-1$.

Substituting these approximations (21) into transform solutions (18)-(20), the forms are convenient to inverse Laplace transform can be obtained. By means of the standard results of the Laplace transform, the corresponding asymptotic solutions in the time domain can be obtained as

$$u=-\frac{k_1\theta_0}{p}\exp\left(-m_1x\right)\left(t-k_1x\right)H\left(t-k_1x\right)+\frac{k_2\theta_0}{p}\exp\left(-m_2x\right)\left(t-k_2x\right)H\left(t-k_2x\right), \tag{22}$$

$$\begin{aligned}\theta=&\frac{\theta_0}{p}\exp\left(-m_1x\right)\left[k_1^2-1+\left(2m_1k_1-\kappa k_1-\frac{q}{p}\left(k_1^2-1\right)\right)\left(t-k_1x\right)\right]H\left(t-k_1x\right)-\\&\frac{\theta_0}{p}\exp\left(-m_2x\right)\left[k_2^2-1+\left(2m_2k_2-\kappa k_2-\frac{q}{p}\left(k_2^2-1\right)\right)\left(t-k_2x\right)\right]H\left(t-k_2x\right)\end{aligned}, \tag{23}$$

$$\sigma_{xx}=\exp\left(\kappa x\right)\frac{\theta_0}{p}\left\{\exp\left(-m_1x\right)\left[1-\frac{q}{p}\left(t-k_1x\right)\right]H\left(t-k_1x\right)-\exp\left(-m_2x\right)\left[1-\frac{q}{p}\left(t-k_2x\right)\right]H\left(t-k_2x\right)\right\}, \tag{24}$$

where $p=k_1^2-k_2^2$, $q=\kappa\left(k_2-k_1\right)+2\left(m_1k_1-m_2k_2\right)$.

Asymptotic Solutions of the Problem

Wave Propagation Analysis

Due to the properties of Heaviside unit function, two waves, named as thermoelastic wave and thermal wave respectively, would generate from the boundary, whose propagation velocities and positions of wavefront can be derived as

$$v_{1,2}=1/k_{1,2},\ \xi_{1,2}=t/k_{1,2}. \tag{25}$$

Combining with the expressions of parameters $k_{1,2}$, we can observe that both propagation velocities $v_{1,2}$ and positions $\xi_{1,2}$ of each wavefront are dependent on relaxation time τ_0 and thermoelastic coupling constant ϑ. The distributions of propagation velocities $v_{1,2}$ versus relaxation time τ_0 at different values of ϑ are shown in Fig.1.

We can clearly observe that $v_{1,2}$ are decreasing with increasing, which indicates the propagation of two waves would be difficult with the enhancement of the delay effect. On the other hand, the effects of ϑ on the propagation of two waves are different, v_1 is decreasing with the increase of , but is increased for v_2. Furthermore, it is noted that the non-homogeneous parameter κ is not contained in expressions $k_{1,2}$, which means that the non-homogeneity of FGMs has no effect on the propagation of two waves.

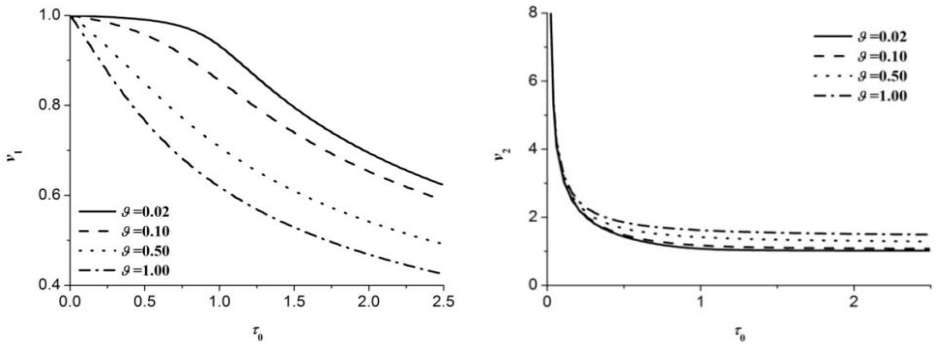

FIGURE 1. DISTRIBUTION OF NON-DIMENSIONAL PROPAGATION VELOCITIES VERSUS RELAXATION TIME CONSTANT

Thermoelastic Response Analysis

Now for the purpose of illustration, we consider copper like material with material constants [9, 16], and some values of non-dimensional parameters are taken as

$\tau_0 = 0.5$, $\vartheta = 0.0168$, $\theta_0 = 1.0$.

Figures 2-4 display the distributions of displacement u, temperature θ and stress component σ_{xx} for a wide range of x ($0 < x < 2.5$) at different time t and given value of $\kappa = -0.5$. The important phenomenon for generalized thermoelastic problem, that is, all of u, θ and σ_{xx} vanish identically at all positions beyond the faster wavefront, can be observed clearly from these distributions. The displacement is continuous at all positions including each wavefront, but the temperature and stress are discontinuous at each wavefront, and two jumps would be generated in each wavefront.

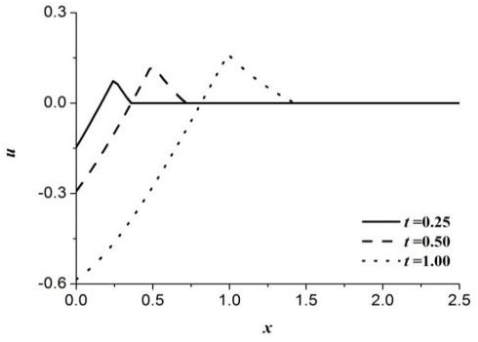

FIGURE 2. DISTRIBUTION OF DISPLACEMENT FOR $\kappa = -0.5$

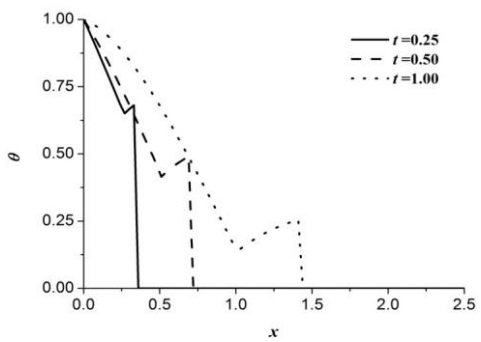

FIGURE 3. DISTRIBUTION OF TEMPERATURE FOR $\kappa = -0.5$

Figures 5-7 displays the variation of each distribution for different values of non-homogeneous parameter κ at given time $t = 0.5$, where $\kappa = 0.0$ corresponds the homogeneous case with constant material properties. Obviously the non-homogeneity has a significant effect to each distribution. The magnitudes of displacement u, temperature θ and stress component σ_{xx} are decreasing with the increasing of parameter for the case of $\kappa < 0$, but all the magnitudes are increasing for the case of $\kappa > 0$, which means the effect of non-homogeneity is dependent on the real variation of material properties with the spatial positions. Furthermore, it is noted that the variation of temperature and stress is more significant than that of displacement for the different values of parameter κ, which means the temperature and stress have the stronger dependency on non-homogeneity of FGMs.

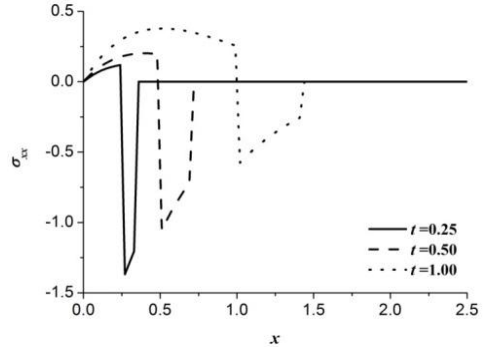

FIGURE 4. DISTRIBUTION OF STRESS COMPONENT FOR $\kappa = -0.5$

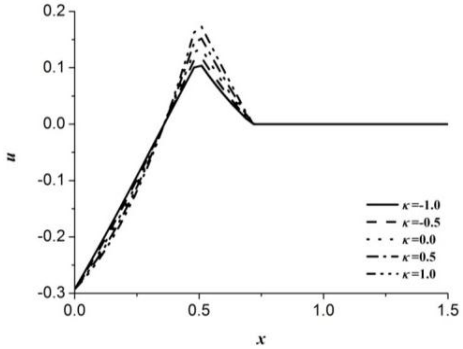

FIGURE 5. DISTRIBUTION OF DISPLACEMENT FOR $t = 0.5$

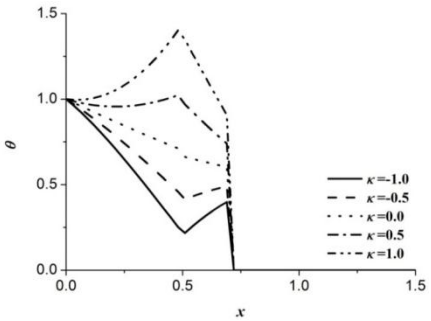

FIGURE 6. DISTRIBUTION OF TEMPERATURE FOR $t = 0.5$

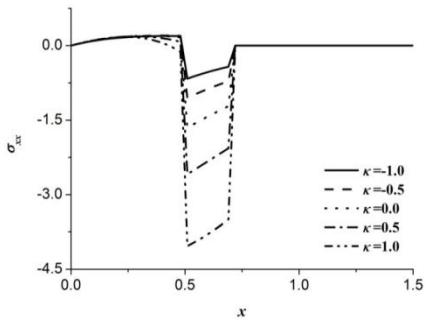

FIGURE 7. DISTRIBUTION OF STRESS COMPONENT FOR $t = 0.5$

Conclusions

The thermoelastic response in a functionally graded solid is studied by an analytical method in this paper. The analysis of the results permits some concluding remarks:

1) The displacement, temperature and stresses have a delay distribution when the heat signal propagates with a finite speed. The propagations of each wave are dependent on the relaxation time τ_0 and thermoelastic coupling constant ϑ, but are independent on non-homogeneous index κ.

2) The presence of non-homogeneous parameter has significant effect on each distributions. Comparison with the effect on displacement, temperature and stresses are more sensitive to the variation of material properties.

REFERENCES

[1] R. C. Wetherhold and S. S. Wang, The use of functionally graded materials to eliminate or control thermal deformation, Compos. Sci. Technol. 56, 1099 (1996).

[2] M. A. Biot, Thermoelasticity and irreversible thermodynamic, J. Appl. Phys.27, 240 (1956).

[3] H. W. Lord and Y. Shulman, A generalized dynamic theory of thermoelasticity, J. Mech. Phys. Solids 15, 299 (1967).

[4] A. E. Green and K. A. Lindsay K A, Thermoelasticity, J. Elast.2, 1 (1972).

[5] A. E. Green and P. M. Naghdi, Thermoelasticity without energy dissipation, J. Elast.31, 189 (1993).

[6] A. Bagri and M. R. Eslami, Generalized coupled thermoelasticity of functionally graded annular disk considering the Lord-Shulman theory, Compos. Struct. 83, 168, (2008).

[7] T. Darabseh, N. Yilmaz and M. Bataineh, Transient thermoelasticity analysis of functionally graded thick hollow cylinder based on Green-Lindsay model, Int. J. Mech. Mater. Des.8, 247 (2012).

[8] M. K. Ghosh and M. Kanoria, Analysis of thermoelastic response in a functionally graded spherically isotropic hollow sphere based on Green-Lindsay theory, Acta Mech. 207, 51 (2009).

[9] S. H. Mallik and M. Kanoria, Generalized thermoelastic functionally graded solid with a periodically varying heat source, Int. J. Solids Struct.44,7633 (2007).

[10] Y. Tokovyy and C. C. Ma, An analytical solution to the three dimensional problem on elastic equilibrium of an exponentially-inhomogeneous layer, J. Mech., 2015, doi: 10.1017/jmech.2015.17.

[11] M. Kanoria and M. K. Ghosh, Study of dynamic response in a functionally graded spherically isotropic hollow sphere with temperature dependent elastic parameters, J. Therm. Stresses 33, 459 (2010).

[12] I. A. Abbas, Nonlinear transient thermal stress analysis of thick-walled FGM cylinder with temperature-dependent material properties, Meccanica, 49, 1697 (2014).

[13] M. Balla, Analytical study of the thermal shock problem of a half-space with various thermoelastic models, Acta Mech.89, 73 (1991).

[14] Y. Z. Wang, X. B. Zhang and X. N. Song, A unified generalized thermoelasticity solution for the transient thermal shock problem, Acta Mech.223, 735 (2012).

[15] Y. Z. Wang, X. B. Zhang and D. Liu, Asymptotic analysis of generalized thermoelasticity for axisymmetric plane strain problem with temperature-dependent material properties, Int. J. Appl. Mech.5, 20 (2013).

Effects of Yield Strength and Elastic Modulus on Cement Sheath Interface Stress at Well Head

Jingfu Zhang*, Siyu Chen, Yingbo Lv, Jundong Chen, Qiang Zhang

Petroleum Engineering Institute, Northeast Petroleum University, Daqing 163318, China

*zjf286@126.com

Abstract

For reasonable choice of mechanical parameters and keeping long-term sealing performance of cement sheath, effect laws of yield strength and elastic modulus on the interface stress of cement sheath at well head were researched. Finite element mechanical model of the casing-cement sheath-stratum combination was established. Damage conditions of cement sheath structural integrity were analyzed. Results showed that every interface stress increased with the increase of the yield strength while cement sheath yielding deformation occurred. And the yield strength could not affect all interface stresses while the deformation was elastic. For lower elastic modulus, elastic deformation occurred in cement sheath and every interface stress increased with the increase of elastic modulus. For high elastic modulus, Cement sheath was partially or fully yielded. With the increase of elastic modulus, the interface contact stress increased, the inner interface circumferential stress decreased, and the interface contact stress was turned into tensile stress after unloading.

Keywords

Cement Sheath; Yield Strength; Elastic Modulus; Interface Stress; Combinatio

Introduction

After cementing, the sealing efficiency of cement sheath would be damaged by stress generated inner the cement sheath or at its interface from producing load. It was important for reasonable designing cement slurry system to analyze the change law of the cement sheath stress. Experts and scholars such as Rodriguez W J, Li Zifeng, Li Jun, Yin Youquan ect. [1-7] had researched the mechanical problems of the casing-cement sheath-stratum combination. Different combination mechanical models were established. Influence law of formation and cement mechanical parameters on the combination were analyzed. However, conditions of continuous radial deformation for the combination were assumed in above achievements of mechanical model and numerical calculation. The problem of probable damage of cement sheath body and bond interface by tensile stress were ignored. Based on the mechanical analysis in the literature [7], the influence law of the cement sheath yield strength、elastic modulus on its interface stress were deeply analyzed.

Finite Element Mechanical Model

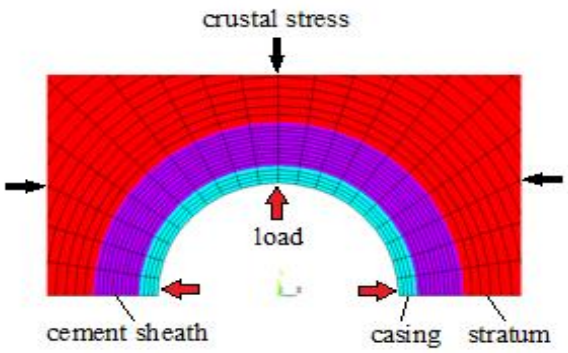

FIGURE 1. FINITE ELEMENT MECHANICAL MODEL

2226-4523/16/01 041-6 © 2016 DEStech Publications, Inc.
doi:10.12783/ijmsci.2016.0601.03

Casing and stratum were bonded together to form the combination of casing-cement sheath-stratum by cement sheath, which was formed by hydration and hardening of cement slurry pumped into the oil and gas well annuals. According to the literature [7] for condition of the creep formation, PLANE183 plane strain unite could be used to describe the mechanical action among casing-cement sheath-stratum combination when casing bending instability and failure were not considered. The 1/2 model could be selected to analyze the stress and strain mechanical problems of the combination for loading and unloading. The mechanics function machine of finite element mechanical model was shown in Fig. 1. In the mechanical model, the linear elastic and nonlinear plastic deformation of cement sheath were all taken into account under the production load action. And the carrying capacity of cement sheath bond interface was also considered to establishe the model.

Constitutive Equation of Cement Sheath

According to the experiment results, deformation properties of cement sheath were the same as those of elastic-plastic material under tri-axial stress action (Fig.2). Elastic deformation was generated at the initial loading stage. Plastic deformation occurred when the loading stress was higher than cement sheath yield strength. According to the deformation characteristic given in Fig.2, cement sheath could be assumed as ideal elastic-plastic material and the following formula could approximately be used to describe the mechanical constitutive relationship for three-dimensional stress condition:

$$\begin{cases} \sigma = E\varepsilon & 0 \le \varepsilon \le \varepsilon_e \\ \sigma = \sigma_e & \varepsilon_e \le \varepsilon \le \varepsilon_s \end{cases} \tag{1}$$

Where, σ was stress; ε was strain; σe was cement sheath yield strength; εe was the strain at yield point; E was cement sheath elastic modulus; εs was total strain generated at cement sheath damage.

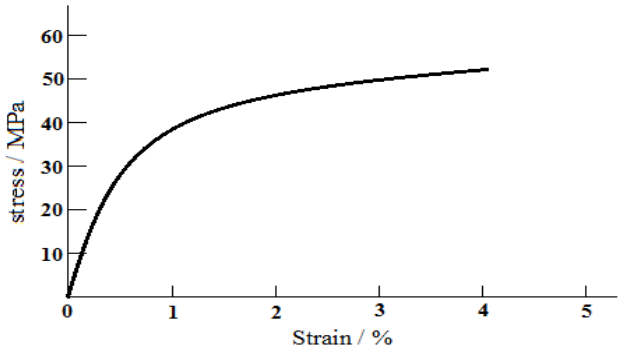

FIGURE 2. STRESS-STRAIN CURVE OF CEMENT SHEATH

Conditions of Combination Failure

Structure integrity damage of casing-cement sheath-stratum combination depended mainly on the cement sheath body and cement bond interface, both of which were the relatively weak parts of combination's carrying capacity. If any one of them was damaged, the combination body was also damaged and the sealing efficiency of cement sheath was failure. Therefore, failure conditions could be established based on the carrying limits of cement sheath body and its bond interface.

There were two characteristics in the mechanical properties of the cement sheath by tri-axial stress action according to experimental results. One was that the plastic deformation would be produced when cement sheath was yielded. And another was that compressive strength was high but tensile strength was low. Thus, the distortion energy density theory and the maximum tensile stress theory could be used to determine the cement sheath carrying capacity.

Under the conditions of the tri-axial stress, cement sheath yielded with Von Mises yield condition:

$$\sigma_M \le \sigma_e \tag{2}$$

$$\sigma_M = \sqrt{\frac{1}{2}\left[(\sigma_1-\sigma_2)^2+(\sigma_2-\sigma_3)^2+(\sigma_3-\sigma_1)^2\right]}$$

(3)

Where, σM was Von Mises stress; σ1, σ2, σ3 were the three principal stresses.

Cement sheath would suffer tensile failure when the tensile stress was higher than the maximum tensile strength:

$$\sigma_{\max} \leq \sigma_t \tag{4}$$

Where, σmax was the maximum tensile stress; σt was the tensile strength of cement sheath.

The cement sheath bond interfaces were the weak parts of the combination and were easily damaged by load action, because of that the bond strength were relatively low. When the contact stress generated at the interface was compressive stress, casing and cement sheath or cement sheath and stratum was at the squeezing state, which represented that the combination was contacted closely. But when the contact stress was tensile stress, the bond interface would be threatened by the radial strech. This radial tensile stress was generally produced in the process of unload because of that cement sheath generated plastic deformation during loading and irrecoverable deformation occurred after unloading. Based on the cement sheath bond interface mechanical relation, bond interface began to tear when radial tension stress reached the cementation strength, and the contact stress was zero when bond interface was completely torn. So, two mechanical conditions decided whether the bond interface would contact or separate: interface contact stress was zero, and there was a gap in bond interface.

According to the above analysis, the combination structure had three aspects of damage conditions, which could be used to evaluate the structure integrity.

Influences of Yield Strength

Cement sheath yield strength was used to evaluate whether there was yielding deformation by load. Figure 3 showed the influence law of yield strength on interface stress calculated by mechanical model. Calculation parameters were: Borehole diameter was 241.3mm. Casing diameter was 177.8mm. Casing thickness was 12.65mm, elastic modulus was 210000MPa and poisson ratio was 0.3. Cement sheath elastic modulus was 10000MPa, poisson ratio was 0.178 and tensile strength was 3.5MPa. The first interfacial bond strength of the cement sheath was 0.6MPa and the second interfacial bond strength was 0.18MPa. Radius of the wellbore surrounding rock was 1m. The crustal stress was zero for the depth of stratum being 0 at well head. Rock elastic modulus was 24000MPa and poisson ratio was 0.25. Loading added at well head was 35MPa, which was the inner pressure of casing.

Fig.3(a) was the calculated results after loading, curves 1 and 2 displayed interior and external interface contact stress of cement sheath (positive value was compressive stress); curves 3 and 4 were interior and external interface circumferential stress (positive value was tensile stress); curves 5 and 6 graphed interior and external interface Von Mises stress; Fig.3 (b) showed the calculated results after unloading, curves 7 and 8 were interior and external interface contact stress (negative value was tensile stress).

With the given load, the cement sheath yield strength and low crustal stress at well head and other conditions, when the casing was loaded, contact stress、Mises stress and circumferential stress of the cement sheath interior interface were higher than corresponding stress of the external interface. When loading (Fig.3 (a)), according to various forms of interface stresses changing with yield strength, it could be divided into two intervals. One was the zone of low yield strength (≤10MPa). Within this zone, the inner side of cement sheath yielded and got partially plastic deformation easily during loading, which Mises stress at yielding part equaled to yield strength (curve 5) based on equation (1). If load was high, whole cement sheath would yield. Each interface stress increased with increasing yield strength. Among all interface stresses, internal interface Mises stress (curve 5) and circumferential stress (curve 3) had obvious variation with yield strength, and others had relatively small change. Another was the zone of high yield strength (>10MPa), cement sheath got elastic deformation by loading, while, yield strength was higher than Mises stress. The yield stress could not affect cement sheath interface stress.

Curves 3 and 4 in Fig.3 (a) showed that when the yield strength reached or over 10MPa, circumferential tensile stress (3.82MPa) of cement sheath internal interface was higher than the given tensile strength (3.5MPa), tensile cracks would appear at the inside cement sheath. However, when the yield strength was lower than 10MPa, the stress was lower than the tensile strength and tensile cracks could not exist.

As shown in Fig.3 (b), as cement sheath only had elastic deformation during loading when the yield strength

exceeded 10MPa, the deformation would fully recover after unloading, at this time, interface contact stress、circumferential stress etc. all restore to the initial state of zero. When cement sheath yielded during loading (yield strength≤10MPa), because the complete recovery of cement sheath deformation was impossible, the radial interface contact stress would change from pressure stress of loading into tensile stress which probably tears cement sheath bond interface, because the boundary stratum could not provide sufficient impetus of deformation recovery. The higher the degree of yielding deformation was, the more easily tearing bond interface was produced. Under the calculated condition in this paper, when yield strength was lower than 10MPa, both of two bond interfaces stresses were tensile stress. The lower the yield strength was, the greater tensile stress was. For the yield strength was 6MPa, the inner interface of cement sheath was torn, while tensile stress was 0 and micro gap was 0.0013mm.

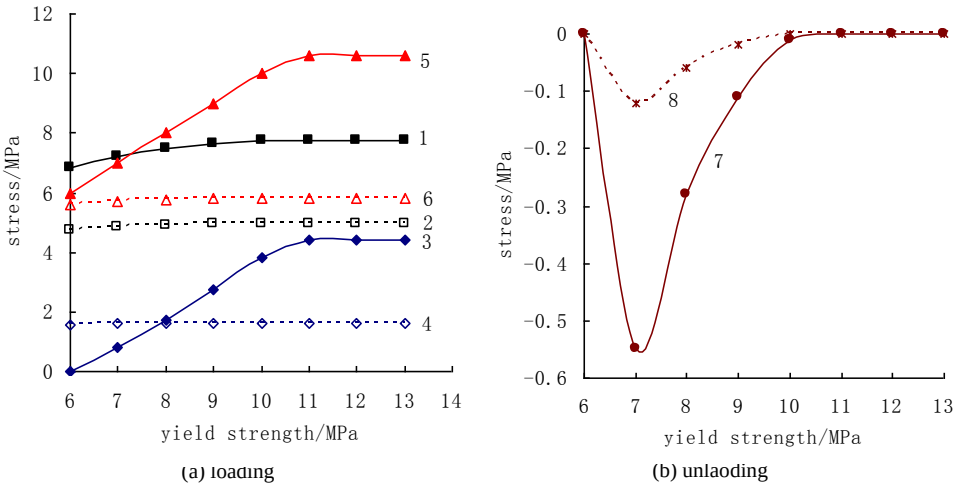

FIGURE 3. EFFECT ON INTERFACE STRESS OF CEMENT SHEATH BY YIELD STRESS

Effects of Elastic Modulus

When cement sheath yield strength was 10MPa, casing loading was 35MPa; effects of cement sheath elastic modulus on interface contact stress, circumferential stress and Von Mises stress were shown in Figure 4. In this figure, curves 1, 2, 3, 4, 5, 6, 7, 8 represented the same stresses as Fig.3.

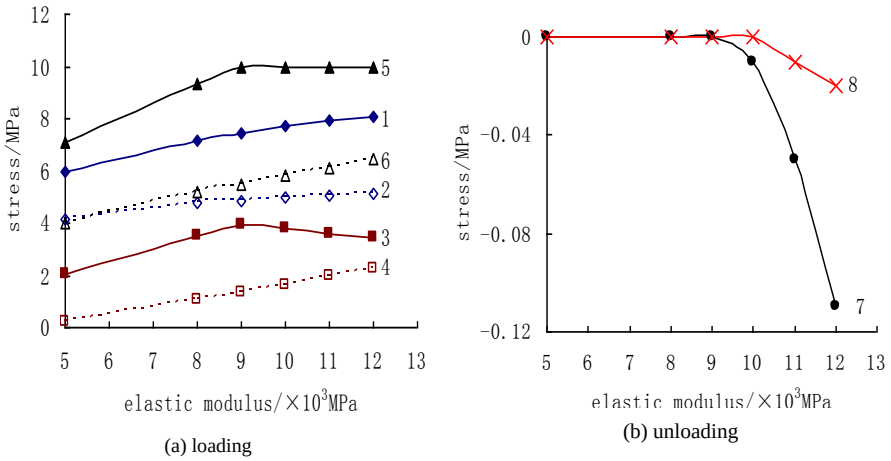

FIGURE 4. EFFECT ON INTERFACE STRESS BY ELASTIC MODULUS

The results in Fig.4 showed that differences of the interior and external interface variation trends could also be classified according to elastic and plastic deformation: ① at the lower value stage of elastic modulus, cement sheath had elastic deformation. With elastic modulus increasing, both of two interfaces various stresses increased; ② when elastic modulus increased to a certain value, the interior interface Mises stress was no less than the yield strength; partial plastic deformation was generated inside the cement sheath, interface Mises stress equaled to the yield strength. After that, the interior interface Mises stress was no longer changeable (see curve 5 in Fig.4). With

increasing elastic modulus, cement sheath interface contact stress, external interface circumferential tensile stress and Mises stress increased (curves1, 2, 4 and 6 in Fig.4), and the interior interface circumferential stress (curve3) decreased.

The results showed that when the elastic modulus of the cement was 9000MPa, interior interface Misess stress (9.97MPa) was close to the yield strength, and when elastic modulus was 10000MPa, cement sheath yielded at inner side, and the Misess stress would remain at a constant value (10MPa). Meanwhile, due to partial yielding of cement sheath, not only did the value variation trend of circumferential stress change with elastic modulus (curve3 in Fig.4), but also the position of the maximum circumferential stress moved to inside cement (Fig.5).

In Fig.5, the elastic modulus of the cement was 12000MPa. The circumferential stress value at different radial position was described by different color, which represented different stress value. The interior interface circumferential stress was 3.44MPa, and the maximum internal tensile stress represented by red portion was 4.18MPa.

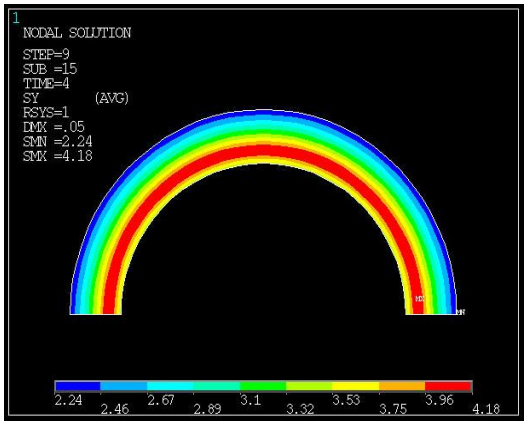

FIGURE 5. CEMENT SHEATH CIRCUMFERENTIAL STRESS CLOUD CHART

According to Fig.4 and Fig.5, when the elastic modulus was 9000MPa, the high tensile stress (3.96MPa) was produced at cement sheath interior interface (curve3 in Fig.4) and the stress exceeded the tensile strength of cement sheath (3.5MPa). So, interior interface tensile cracks would be generated. The structural integrity of the cement sheath would be damaged. Then, with elastic modulus continually increasing, even though the interior interface circumferential stress was decreased, it was still possible that the maximum circumferential stress (4.18MPa) inside cement sheath was higher than the tensile strength, which leaded to tensile break of inside cement.

After unloading, for the elastic deformation region of low elastic modulus, casing、cement sheath and stratum generated elastic deformation recovery, all stresses returned to the initial condition before loading. But for the region of high elastic modulus, when cement sheath yielded, the interior and external interface contact stress was turned into tensile stress after unloading (Fig.4 (b)), and compressive stress was generated at the circumferential direction of cement sheath. With increasing elastic modulus, interface radial tensile stress increased, and tearing cement sheath bond interface became more possible.

According to the above calculated results, cement sheath various mechanical parameters cooperated harmoniously when taking yield strength, elastic modulus and load capacity all into account. Therefore, working loading and cement sheath mechanical characteristics should be the basement to design cement slurry system.

Conclusions

(1) For the zone of low yield strength, when loading, internal cement sheath yielded and got partially plastic deformation easily. Within this zone, with increasing yield strength of cement sheath, each interface stress increased. Among all interface stresses, cement sheath internal interface Mises stress and circumferential stress have obvious variation with yield strength, and others have relatively small change. For the zone of high yield strength, cement sheath got elastic deformation. Yield strength could not affect cement sheath interface stress.

(2) At the initial stage of elastic modulus increasing, cement sheath had elastic deformation. With elastic modulus

increasing, various stresses of cement sheath interior and external interface increased. When elastic modulus increased to a certain value, partial plastic deformation was generated inside the cement sheath. After that, cement sheath interior interface Mises stress was no longer changeable. With increasing elastic modulus, cement sheath interface contact stress, circumferential tensile stress and Mises stress of external interface increased, and circumferential stress of interior interface decreased.

(3) In the process of cement sheath elastic deformation during loading, maximum circumferential tensile stress was at cement sheath interior interface. After unloading, the combination structure could fully recover, and all stresses could return to the initial condition. In the process of cement sheath yielding deformation during loading, position of maximum circumferential tensile stress moved from interior interface to inside cement sheath. After unloading, there was radial tensile stress on cement sheath interface, and bonding interface had potential risk of tearing.

ACKNOWLEDGMENT

The authors wish to thank National Natural Science Foundation of China and National Natural Science Foundation of Heilongjiang Province for supporting the research. The supporting research projects were respectively: Mechanical analysis and research on annular sealing reliability of cement sheath (51474074); Analysis on structure integrity of casing-cement sheath-stratum cementing combination (E201334).

REFERENCES

[1] W. J. Rodriguez, W. W. Fleckenstein, A. W. Eustes. Simulation of collapse loads on cemented casing using finite element analysis[C] . SPE 84566, 2003 :1-9.

[2] Z. F. Li, Y. G. Zhang, X.J.Yang. Mechanics model for interaction between creep formation and oil well casing Acta Petrolei Sinica, 2009, 30(1): 129-131.

[3] J. Li, M. Chen, G. H. Liu, et al. Elastic-plastic analysis of casing-concrete sheath-rock combination[J]. Acta Petrolei Sinica, 2005,26 (6): 99-103.

[4] Y. Q. Yin, C. W. Chen, E. Q. Li, et al. Theoretical solutions of stress distribution in casing-cement and stratum system [J]. Chinese Journal of Theoretical and Applied Mechanics, 2006,38 (6): 835-842.

[5] J. Fang, H. W. Zhao, B. Q. Yue, et al. Analys is of loading property of casing and cement sheath under non uniform geologic stress [J]. Journal of the Universirty of Petroleum, China, 1995, 19(6) : 52-57.

[6] B. Zhou, X. Yao, S. D. Hua. The influence of pressure testing of casing string on the integrity of cement sheath [J]. Drilling Fluid & Completion Fluid, 2009,26(1): 32-34.

[7] J. F. Zhang, D. B. Zhang, Q. Zhang, et al. Impact of elastic parameters of cement ring on structural integrity of casing-cement ring-strata cementing combination[J]. Oil Drilling & Production Technology, 2013, 35(5): 43-46.

Preparation and Electrochemical Performance Of Cr3+ and Sb5+ Co-Doped Li4Ti5O12 Anode Material for Lithium-Ion Batteries

Fuyun Li, Min Zeng*

School of Materials Science and Engineering, Southwest University of Science and Technology, Mianyang 621010, P R China

*zengmin@swust.edu.cn

Abstract

Cr3+/Sb5+ co-doped Li4Ti5O12 in the form of Li4Ti5-2xCrxSbxO12 (0≤x≤0.1) compounds were successfully synthesized via solid-state reaction method. The structure and electrochemical properties of the spinel Li4Ti5-2xCrxSbxO12 materials were investigated. The Li4Ti5-2xCrxSbxO12 (x=0.05) presents the best discharge capacity among all the samples, and shows better reversibility and higher cyclic stability compared with pristine Li4Ti5O12, especially at high current rates. When the discharge rate was 1C, the Li4Ti5-2xCrxSbxO12 (x=0.05) sample presented the excellent discharge capacity of 166.7 mAhg-1, which was very close to the theoretical capacity of Li4Ti5O12 (175mAhg-1).

Keywords

Lithium-Ion Battery; Anode Material; Li4Ti5O12; Cr3+/Sb5+ Co-Doping; Capacity

Introduction

Nowadays, lithium-ion batteries are widely employed as the main power source for portable electronic devices and the increasingly popular electric vehicles (EVs) or hybrid electric vehicles (HEVs) 1-4. Material development is one of the most important tasks to achieve these goals. Among the studied electrode materials, Li4Ti5O12 has been demonstrated as a promising anode material of lithium-ion batteries, since it has excellent Li-ion insertion, extraction reversibility and almost negligible volume change during charge-discharge process. Unfortunately, its rate performance is limited heavily due to the low electronic conductivity of material 5. To improve the conductivities, several effective ways have been proposed, including synthesis of nano-sized Li4Ti5O12 6,7, doping with metal ions (such as V5+, Mn4+, Cr3+, Mg2+ and F−) in Li, Ti or O sites 1-2,8-10, surface coating (such as Ag, Cu, Zn, TiN, SnO2, TiO2, carbon, carbon nanotubes, and graphene) 11-16. It was found that a substitution of Ti4+ site by Zr4+ can increase the amount of mixing Ti3+/Ti4+ as charge compensation and thus enhance its electronic conductivity 17. The average valence state of Cr3+ and Sb5+ is +4, which is equal to that of Ti4+. The ionic radius of Ti4+ (0.605 Å) is comparable to that of Cr3+ (0.615 Å) and Sb5+ (0.60 Å). Hence, there is a possibility to increase the electronic conductivity of Li4Ti5O12 which is to substitute Cr3+ and Sb5+ on a Ti4+ site, which should lead to an increase in electron concentration. In this work, Cr3+/Sb5+ co-doped Li4Ti5O12 powders were prepared by solid-state reaction method and the effect of Cr3+/Sb5+ co-doping on the physical and electrochemical performance of Li4Ti5-2xCrxSbxO12 was systematically investigated.

Experimental Procedure

The pristine Li4Ti5O12 (LTO) and Cr3+/Sb5+ co-doped Li4Ti5O12 (Cr, Sb - LTO) samples were synthesized by solid-state reaction method. The raw materials consisted of Li2CO3 (AR, Chengdu kelong Chemical Agents Co. Ltd), TiO2 (P25 Nano Material, Hetachroma), Cr2O3 (AR, Shanghai Chemical Agents Co. Ltd) and Sb2O5 (AR, Shanghai Chemical Agents Co. Ltd) according to the stoichiometric quantities of Li4.2Ti5-2xCrxSbxO12 (x=0, 0.025, 0.05, 0.075 and 0.1). Excess Li was added to compensate for lithium volatilization during the sintering process. The raw materials were mixed at the required molar ratios, ball milled, and sintered at 800°C for 12 h to prepare the Li4Ti5-2xCrxSbxO12.

The samples were initially characterized by X-ray diffraction using an X-ray diffraction analyzer with Cu-Kα

2226-4523/16/01 047-5 © 2016 DEStech Publications, Inc.
doi:10.12783/ijmsci.2016.0601.04

radiation (X`Pert PRO, PANalytical). The more detailed structural information was measured on a transmission electron microscope (TEM) and a high-resolution transmission electron microscope (HRTEM, Tecnai F20, FEI). The electrochemical characterizations were realized in CR2016-type coin cell. The working electrodes were fabricated by mixing the active materials, super P and polyvinylidene difluoride (PVDF) in a weight ratio of 80 : 10 : 10, and then milled homogeneously in an agate mortar. Subsequently, an appropriate amount of N-methylpyrrolidone (NMP) solvent was slowly introduced and wet mixed to produce electrode slurry. The uniform slurry was coated onto a copper foil using a scraper and dried at 120℃ for 24 h to remove the solvent. Then the electrodes were punched into disks and assembled into half cells in an Ar-filled glove box. Li foils were used as the counter electrodes and the polypropylene microporous films (Celgard 2300) were enployed as the separators. The commercial electrolyte was 1 M solution of LiPF6 in ethylene carbonate (EC) and dimethyl carbonate (DMC) in a volume ratio of 1:1. Electrochemical impedance spectroscopy (EIS) were measured by means of a CHI760C electrochemical station in the frequency range of 0.01 Hz to 10 kHz. Charge-discharge measurement at room temperature was carried out using a LAND test system with cut- off voltage of 1.0–2.5 V (vs. Li/Li+) at constant current densities (1C).

Results and Discussion

The X-ray diffraction (XRD) patterns of the samples of Li4Ti5-2xCrxSbxO12 (0≤x≤0.1) are shown in Fig 1. The diffraction patterns of LTO powders with and without Cr2O3 and Sb2O5 particles agreed well with cubic spinel LTO (JCPDS 49-0207). The diffraction peaks were sharp and strong, suggesting their high crystallinity. No impure-phases related peaks were detected in the XRD patterns of Li4Ti5-2xCrxSbxO12 (x<0.075), indicating that the Cr3+ and Sb5+ ions had entered the lattice of Li4Ti5O12 without destroying the crystal structure of pristine Li4Ti5O12 or forming a new phase. However, for x≥0.075, a few impurity peaks emerge in the XRD diagrams, which shows that (Cr, Sb) was co-replaced for Ti and also that there is a limit to the amount of doping elements for Li4Ti5O12.

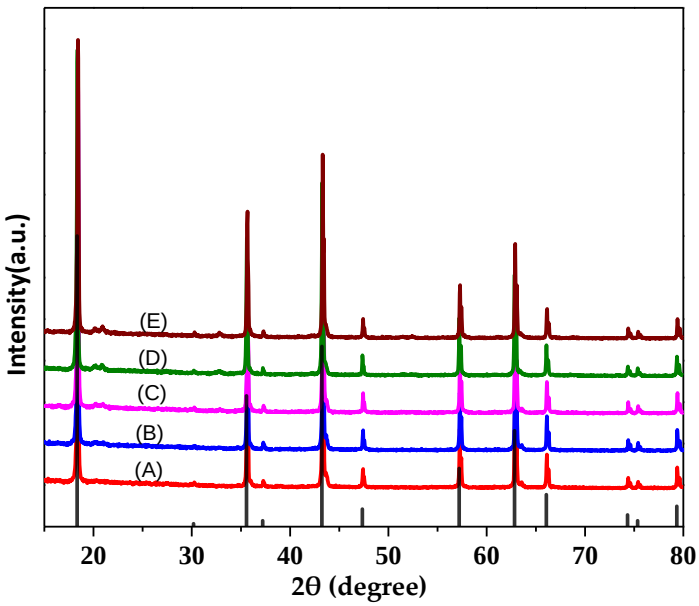

FIGURE 1. XRD PATTERNS OF PURE LI4TI5O12 POWDERS: X=0(A) AND DOPED POWDERS Li4Ti5-2xCrxSbxO12: X=0.025(B), X=0.05(C), X=0.075(D), X=0.1(E).

Fig. 2(a) and 2(b) show the typical transmission electron microscopy (TEM) images of the pristine Li4Ti5O12 and sample Li4Ti5-2xCrxSbxO12 (X=0.05). From the images, we can see that the samples are composed of irregular particles, and the particle size is almost in a range of 100-500 nm.

As can be seen in Fig. 2(c) and 2(d), the lattice parameters of synthesized samples are changed. The interplanar spacing is ca. 4.832 Å (Fig. 2(c)), corresponding to (111) latticeplane of Li4Ti5O12. However, the interplanar spacing (111) of the doped material is ca. 4.61 Å (Fig. 2(d)), which is a bit smaller than the undoped one. The changing trend shown on the lattice parameters of synthesized samples is related to the doping amount of the Cr3+ and Sb5+, and the lattice parameter reduces with the co-doping of the Cr3+ and Sb5+ ions. This suggests that Cr3+ and Sb5+ ions had entered the Ti sites of the crystal structure and produced adverse lattice distortion.

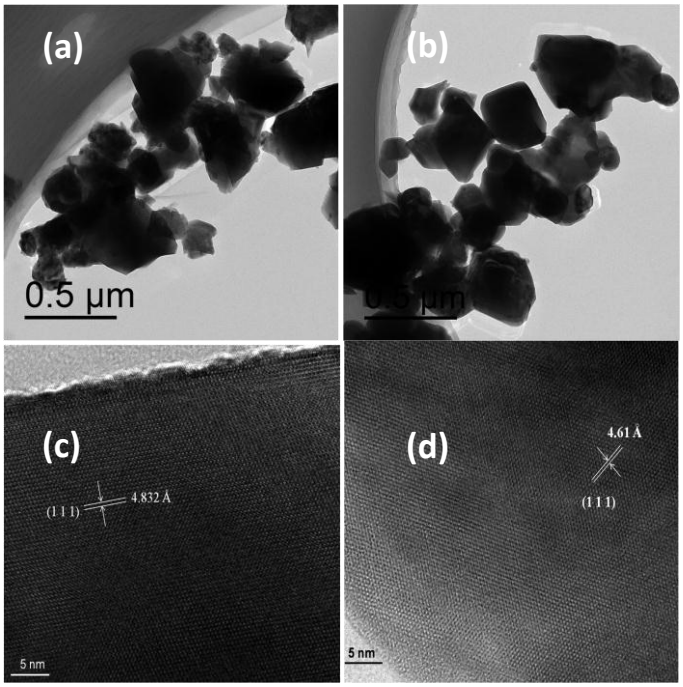

FIGURE 2. (A) TEM IMAGE AND (C) HRTEM IMAGE OF PURE Li4Ti5O12. (B) TEM IMAGE AND (D) HRTEM IMAGE OF Li4Ti5-2xCrxSbxO12 (X=0.05).

Electrochemical impedance spectroscopy (EIS) was performed and the corresponding Nyquist plots of the spectra are shown in Fig. 3(a). Compared with Li4Ti5O12, the Cr3+/Sb5+ co-doped Li4Ti5O12 displays lower transfer impedance, which means that the doped material has better conductivity than the undoped one.

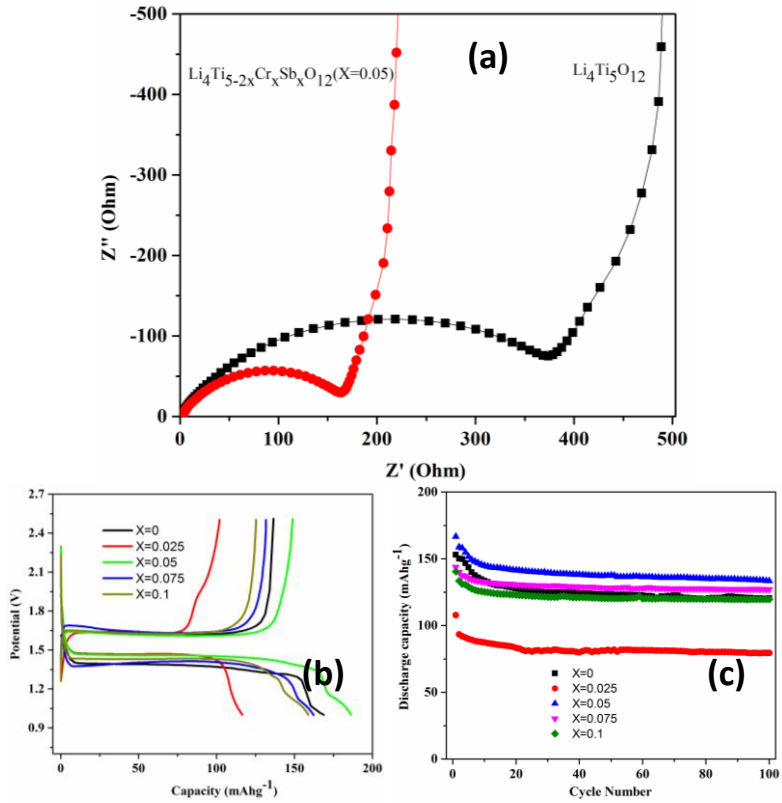

FIGURE 3. (A) THE AC IMPEDANCE SPECTRA OF THE AS-PREPARED CELLS. (B) INITIAL CHARGE/DISCHARGE CURVES AND (C) CYCLING PERFORMANCE OF THE PURE Li4Ti5O12 POWDERS AND DOPED POWDERS Li4Ti5-2xCrxSbxO12 (CURRENT RATE, 1 C).

The initial charge and discharge galvanostatic curves of all samples at 1 C are shown in Fig. 3(b). It can be seen that the Li4Ti5-2xCrxSbxO12 samples displayed the first discharge capacities of 153.1 (X=0), 107.8 (X=0.025), 166.7 (X=0.05), 143.8 (X=0.075), and 140.55 (X=0.1) mAhg-1, respectively. The flat plateau position of the charge and

discharge curves for all samples at about 1.7 and 1.5 V can be attributed to the redox reactions of Ti4+/Ti3+ in Li4Ti5O12. In addition, it can be noted that a small discharge plateau is observed at about 1.1 V (vs. Li/Li+). These peaks can be ascribed to the phase transformation of impurity. However, there is not any signal in the charging process, this may be due to the charging platform of impurity is higher than 2.5 V (vs. Li/Li+). Fig. 3(c) shows the cycle performance of the as-obtained samples at 1C rate. The cut-off voltage is set between 1.0 and 2.5 V. The doped samples show better cycle performance than the pristine Li4Ti5O12. Among these Cr3+/Sb5+ co-doped samples, only the capacity and cycle performance of sample Li4Ti5-2xCrxSbxO12 (x=0.05) is larger than the pure Li4Ti5O12. This may due to the interaction of adverse lattice distortion and synergistic effect of doping and compositing.

Conclusions

Li4Ti5-2xCrxSbxO12 powders have been successfully synthesized by solid-state reaction method. XRD patterns show that all Cr3+/Sb5+ co-doped materials have good crystallinity and high phase purity. With increasing the Cr3+/Sb5+ co-doping amount, the lattice parameter is observed to decrease. From the above discussion, it can be seen that the Cr3+ and Sb5+ ions had entered the lattice of Li4Ti5O12 without destroying the crystal structure of pristine Li4Ti5O12 or forming a new phase. The Li4Ti5-2xCrxSbxO12 (X=0.05) electrode presents a higher specific capacity and better cycling performance than the Li4Ti5O12 electrode prepared by the similar process. Li4Ti5-2xCrxSbxO12 (X=0.05) exhibits a specific capacity of 166.7 mAhg-1 at 1C. All the evidences demonstrate that the Li4Ti5-2xCrxSbxO12 (X=0.05) electrode is a promising anode material for Li-ion batteries.

REFERENCES

[1] D. Li, Y. Sun, X. Liu, R. Peng and H. Zhou, Doping-induced memory effect in Li-ion batteries: the case of Al-doped, Chem. Sci. 6, 4066(2015).

[2] S. Y. Li, M. Chen, Y. Xue and Z. B. Wang, Electrochemical properties of citric acid-assisted combustion synthesis of Li4Ti5O12 adopting Cr by the solid-state reaction process, Ionics. 21, 1545(2015).

[3] S. Chen, Y. L. Xin, Y. Y. Zhou and L. M. Qi, Self-supported Li4Ti5O12 nanosheet arrays for lithium ion batteries with excellent rate capability and ultralong cycle life, Energy. Environ. Sci.7, 1924(2014).

[4] Y. C. Kuo and J. Y. Lin, One-pot sol-gel synthesis of Li4Ti5O12/C anode materialsfor high-performance Li-ion batteries, Electrochimi. Acta. 142, 43(2014).

[5] C. H. Chen, J. T. Vaughey, A. N. Jansen and M. M. Thackeray, Studies of Mg-substituted Li4-xMgxTi5O12 spinel electrodes (0≤x≤1) for lithium batteries, J. Electrochem. Soc. 148, 102(2001).

[6] L. f. Shen, X. G. Zhang, E. Uchaker and G. Z. Cao, Li4Ti5O12 nanoparticles embedded in a mesoporous carbon matrix as a superior anode material for high Rate lithium ion batteries, Adv. Energy. Mater. 2, 691(2012).

[7] W. Wang, B. Jiang and S. Q. Jiao, A nanoparticle Mg-doped Li4Ti5O12for high rate lithium-ion batteries, Electrochimi. Acta. 114, 198(2013).

[8] M. D. Ji, Y. L. Xu and C. H. Zhao, Preparation and electrochemical performance of La3+ and F- co-doped Li4Ti5O12 anode material for lithium-ion batteries, J. Power. Sources. 263, 296(2014).

[9] H. D. Yoo, Y. L. Liang and Y. Yao, High areal capacity hybrid magnesium-lithium-ion battery with 99.9% coulombic efficiency for large-scale energy storage, ACS. Appl. Mater. Interfaces. 7, 7001(2015).

[10] Y. Y. Zhang et al, Influence of Sc3+ doping in B-site on electrochemical performance of Li4Ti5O12 anode materials for lithium-ion battery, J. Power Sources, 250, 50(2014).

[11] L. P. Wang et al, Superior rate performance of Li4Ti5O12/TiO2/C/CNTs composites via microemulsion-assisted method as anodes for lithium ion battery, Electrochim. Acta, 142, 202(2014).

[12] X. Wang, D. Q. Liu and C. Zhang, Cu/Li4Ti5O12 scaffolds as superior anodes for lithium-ion batteries, NPG. Asia. Mater.7, 171(2015).

[13] H. Q. Zhang, et al, Surface structure and high-rate performance of spinel Li4Ti5O12 coated with N-doped carbon as anode material for lithium-ion batteries, J. Power Sources, 239, 538(2013).

[14] Y. Q. Wang, L. Gu and L. J. Wan, Rutile-TiO2 nanocoating for a high-rate Li4Ti5O12 anode of a lithium-ion battery, J. Am. Chem. Soc.134, 7874(2012).

[15] Y. Wang, et al, Solid state synthesis of graphite carbon coated Li4Ti5O12 anode for lithium ion batteries', IONICS, 20, 1377(2014).

[16] Y. Wang, A. J. Zhou and J. Z. Li, Solid-state synthesis of submicron-sized Li4Ti5O12/Li2TiO3 composites with rich grain boundaries for Lithium ion batteries, J. Power Sources, 266, 114(2014).

[17] T. F. Yi, B. Chen and H. B. Qiao, Spinel Li4Ti5-xZrxO12 (0≤x≤0.25) materials as high-performance anode materials for lithium-ion batteries, J. Alloy. Compd. 558, 11(2013).

Cracking Angle of an Arbitrary Oriented Crack Embedded in a Strip under I-II Mixed Mode Loading

B. K. Guo[1], H. H. Yan[2], L. Zhang[3]

[1]Department of Mechanics, Xi'an University of Architecture and Technology, Xi'an, 710055, China

[2]College of Mechanical and Electrical Engineering, Xi'an University of Architecture and Technology, Xi'an, 710055, China

[3]Department of Astronautic Science and Mechanics, Harbin Institute of Technology, Harbin, 150001, China

[1]guobaoke@126.com; [2]yanhh521@126.com; [3]19666894@hit.edu.cn

Abstract

In this paper, the stress intensity factor and the initial cracking angle of a crack with an arbitrary oriented direction in a strip material are calculated. The aim is to consider the variation of the angle with the orientation of the cracks and their position. Firstly, the problem is separated by the superposition principle into several sub-problems which are solved using Fourier transformation technique. For the sub-problem of a crack, the unknown dislocation density functions are introduced. Singular integral equations are then obtained and solved by a numerical method. The stress intensity factor and the initial angle are obtained. The results show that crack tends to propagate to the free boundary and the influence of the existence of other cracks on the initial cracking angle can be negligible when the distance between the cracks is larger.

Keywords

Initial Cracking Angle; Fourier Integral Transformation; Singular Integral Equation; Stress Intensity Factor

Introduction

Layered structure is a kind of common material, and is used widely because of lower-expense, easy-producing and multi-function, and a strip is the basic component. In this structure, there often exist many inevitable problems (such as cracking, spallation, debonding and so on). So its fracture and damage mechanics became important and complex rather than common single material. For the better understanding of the mechanics, some researchers have done many useful studies 1–10 up to now. In the above studies, they did not consider the initial cracking angle and its variation when the position and the number of crack are changing. To determine the angle, researchers have proposed some different fracture criteria 11–14 and have obtained many useful results which very agree with the corresponding experiments. In this paper, the problem about initial cracking angle of an arbitrarily oriented crack embedded in a strip with one or several cracks is studied analytically. The aim of this paper is to investigate the variation of the angle when the distance between crack tip and interface and the crack direction are changing.

Description of Problem

Let's consider a problem of a strip structure in which many or single oriented cracks are embedded (see Fig.1). We set coordinate system 0xy to be the global coordinate system. The strip is homogeneous and is infinite along x-axis and has thickness H along y-axis. $0^i x^i y^i (i = 1,2\ldots)$ are local coordinate systems with origin point 0^i located at crack center point. x^i-axis is along the surface of crack and y^i-axis perpendicular. (x_c^i, y_c^i) are the coordinates of point 0^i in 0xyz. θ^i is the angle from x to x^i and $0 \le \theta^i \le \pi$. μ, ν are shear modulus and Poisson's ratio of the material, respectively.

Applying the superposition principle, the problem can be treated as a sum of two sub-states. One is a strip structure with the same dimensions but no crack on it. The other can then be separated into several single crack situations. We let $u_x, u_y, \sigma_{xx}, \sigma_{yy}, \sigma_{xy}$ denote the total displacement, stress components of the problem in 0xy, and

2226-4523/16/01 052-7 © 2016 DEStech Publications, Inc.
doi:10.12783/ijmsci.2016.0601.05

$u_x^0, u_y^0, \sigma_{xx}^0, \sigma_{yy}^0, \sigma_{xy}^0$ the displacement, stress components without crack in 0xy, and $u_{x^i}^i, u_{y^i}^i, a_{x^i x^i}^i, \sigma_{y^i y^i}^i, \sigma_{x^i y^i}^i$ the displacement, stress components of single crack problem in $0^i x^i y^i$. So

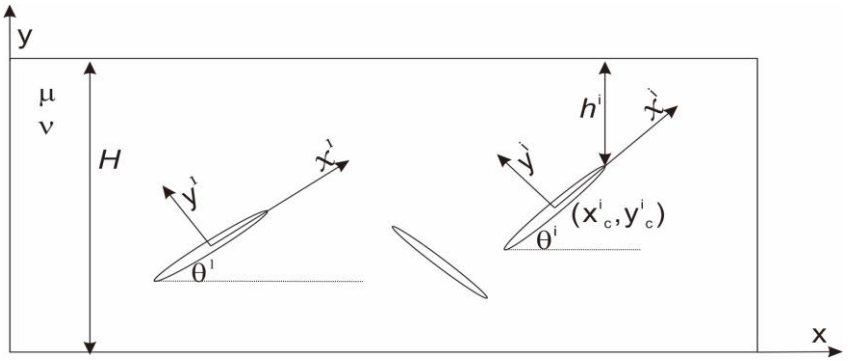

FIGURE 1. GEOMETRY OF A STRIP STRUCTURE WITH SOME CRACKS

$$\begin{pmatrix} u_x \\ u_y \end{pmatrix} = \begin{pmatrix} u_x^0 \\ u_y^0 \end{pmatrix} + \sum_{i=1}^{N} \mathbb{A}_1^i \begin{pmatrix} u_{x^i}^i \\ u_{y^i}^i \end{pmatrix}, \mathbb{A}_1^i = \begin{pmatrix} \cos\theta^i & -\sin\theta^i \\ \sin\theta^i & \cos\theta^i \end{pmatrix} \tag{1}$$

Here N is the crack number and $\mathbb{A}_1^i$ is displacement transformation matrix from $0^i x^i y^i$ to 0xy. So the coordinates of point (x^i, y^i) in 0xy is

$$\begin{pmatrix} x \\ y \end{pmatrix} = \begin{pmatrix} x_c^i \\ y_c^i \end{pmatrix} + \mathbb{A}_1^i \begin{pmatrix} x^i \\ y^i \end{pmatrix} \tag{2}$$

The total stress of the strip is

$$\begin{pmatrix} \sigma_{xx} \\ \sigma_{yy} \\ \sigma_{xy} \end{pmatrix} = \begin{pmatrix} \sigma_{xx}^0 \\ \sigma_{yy}^0 \\ \sigma_{xy}^0 \end{pmatrix} + \sum_{i=1}^{N} \mathbb{B}_1^i \begin{pmatrix} \sigma_{x^i x^i}^i \\ \sigma_{y^i y^i}^i \\ \sigma_{x^i y^i}^i \end{pmatrix} \tag{3}$$

Here $\mathbb{B}_1^i$ is the stress transformation matrix, and

$$\mathbb{B}_1^i = \begin{pmatrix} \cos\theta^i \cos\theta^i & \sin\theta^i \sin\theta^i & -\sin 2\theta^i \\ \sin\theta^i \sin\theta^i & \cos\theta^i \cos\theta^i & \sin 2\theta^i \\ \sin\theta^i \cos\theta^i & -\sin\theta^i \cos\theta^i & \cos 2\theta^i \end{pmatrix} \tag{4}$$

The total displacement and stress components in coordinate system $0^i x^i y^i$ can be obtain easily as

$$\begin{pmatrix} u_{x^i} \\ u_{y^i} \end{pmatrix} = \mathbb{A}_2^i \begin{pmatrix} u_x \\ u_y \end{pmatrix}, \begin{pmatrix} \sigma_{x^i x^i} \\ \sigma_{y^i y^i} \\ \sigma_{x^i y^i} \end{pmatrix} = \mathbb{B}_2^i \begin{pmatrix} \sigma_{xx} \\ \sigma_{yy} \\ \sigma_{xy} \end{pmatrix} \tag{5}$$

Here, $\mathbb{A}_2^i = \left(\mathbb{A}_1^i\right)^{-1}, \mathbb{B}_2^i = \left(\mathbb{B}_1^i\right)^{-1}$, superscript -1 means the inverse operation of matrix.

In this paper, the loading is acting on the face of cracks. The boundary and continuous conditions can be described as following

$$\begin{cases} \sigma_{xy}(x,0) = 0, \sigma_{yy}(x,0) = 0 \\ \sigma_{xy}(x,H) = 0, \sigma_{yy}(x,H) = 0 \end{cases}, \begin{cases} \sigma_{y^i y^i}(x^i, 0^+) = \sigma_{y^i y^i}(x^i, 0^-) \\ \sigma_{x^i y^i}(x^i, 0^+) = \sigma_{x^i y^i}(x^i, 0^-) \end{cases} \tag{6}$$

$$x^i \notin (-a^i, a^i), \begin{cases} u_{x^i}(x^i, 0^+) = u_{x^i}(x^i, 0^-) \\ u_{y^i}(x^i, 0^+) = u_{y^i}(x^i, 0^-) \end{cases} \tag{7}$$

$$x^i \in (-a^i, a^i), \begin{cases} \sigma_{x^i y^i}(x^i, 0^+) = \sigma_{x^i y^i}(x^i, 0^-) = -\tau(x^i)\delta_1^i \\ \sigma_{y^i y^i}(x^i, 0^+) = \sigma_{y^i y^i}(x^i, 0^-) = -\sigma(x^i)\delta_1^i \end{cases} \tag{8}$$

Here a^i is half length of the ith crack and δ_1^i is dirichet function.

Basic equations and singular integral equations

We can set the displacement solutions of the problem as following

$$u_x = \frac{1}{\sqrt{2\pi}}\int_{-\infty}^{+\infty}\left(\begin{array}{l}\sum_{k=1}^{4} d_k\, C_k^0(\alpha)\exp\left(n_k y + I\alpha x\right) + \\ \sum_{i=1}^{N}\sum_{l=1}^{2} F_l^i(\alpha)\sum_{k=1}^{4}\left(a_{11}^{i1}d_k + a_{12}^{i1}\right)\frac{h_{kl}}{h}\exp\left(n_k y^i + I\alpha x^i\right)\end{array}\right)d\alpha,$$

$$u_y = \frac{1}{\sqrt{2\pi}}\int_{-\infty}^{+\infty}\left(\begin{array}{l}\sum_{k=1}^{4} C_k^0(\alpha)\exp\left(n_k y + I\alpha x\right) + \\ \sum_{i=1}^{N}\sum_{l=1}^{2} F_l^i(\alpha)\sum_{k=1}^{4}\left(a_{21}^{i1}d_k + a_{22}^{i1}\right)\frac{h_{kl}}{h}\exp\left(n_k y^i + I\alpha x^i\right)\end{array}\right)d\alpha \tag{9}$$

Here a_{jk}^{i1} is the i row, j column component of matrix $\mathbb{A}_1^i$, $C_k^0(\alpha)$ are unknown functions, $F_l^i(\alpha)(l = 1,2, i = 1,2,\ldots,N)$ are defined as

$$F_l^i(\alpha) = \int_{-a^i}^{a^i} D_l^i(t)\exp\left(-I\alpha t\right)dt \tag{10}$$

$n_k(k = 1,2,3,4)$ are the roots of equation $n^4 - 2\alpha^2 n^2 + \alpha^4 = 0$, and

$$d_k = \frac{n_k\left(-\alpha(-i + s(1-2\nu)^2) + n_k^2(2 - 6\nu + 4\nu^2)\right)}{2\alpha^2(-1+\nu)} \tag{11}$$

$$\begin{aligned}
h_{11} &= I\left(g_{24}(g_{32} - g_{33}) + g_{22}(g_{33} - g_{34}) + g_{23}(-g_{32} + g_{34})\right)\\
h_{12} &= I\left(d_4(g_{23}g_{32} - g_{22}g_{33}) + d_3(-g_{24}g_{32} + g_{22}g_{34}) + d_2(g_{24}g_{33} - g_{23}g_{34})\right)\\
h_{21} &= I\left(g_{24}(-g_{31} + g_{33}) + g_{23}(g_{31} - g_{34}) + g_{21}(-g_{33} + g_{34})\right)\\
h_{22} &= I\left(d_4(-g_{23}g_{31} + g_{21}g_{33}) + d_3(g_{24}g_{31} - g_{21}g_{34}) + d_1(-g_{24}g_{33} + g_{23}g_{34})\right)\\
h_{31} &= I\left(g_{24}(-g_{31} + g_{32}) + g_{22}(g_{31} - g_{34}) + g_{21}(-g_{32} + g_{34})\right)\\
h_{32} &= I\left(d_4(-g_{22}g_{31} + g_{21}g_{32}) + d_2(g_{24}g_{31} - g_{21}g_{34}) + d_1(-g_{24}g_{32} + g_{22}g_{34})\right)\\
h_{41} &= I\left(g_{23}(g_{31} - g_{32}) + g_{21}(g_{32} - g_{33}) + g_{22}(-g_{31} + g_{33})\right)\\
h_{42} &= I\left(d_3(g_{22}g_{31} - g_{21}g_{32}) + d_2(-g_{23}g_{31} + g_{21}g_{33}) + d_1(g_{23}g_{32} - g_{22}g_{33})\right)\\
h &= \alpha\begin{pmatrix} d_1\left(g_{22}(g_{34} - g_{33}) + g_{23}(g_{32} - g_{34}) + g_{24}(g_{33} - g_{32})\right)\\ +d_2\left(g_{21}(g_{33} - g_{34}) + g_{23}(g_{34} - g_{31}) + g_{24}(g_{31} - g_{33})\right)\\ +d_3\left(g_{21}(g_{34} - g_{32}) + g_{22}(g_{31} - g_{34}) + g_{24}(g_{32} - g_{31})\right)\\ +d_4\left(g_{21}(g_{32} - g_{33}) + g_{22}(g_{33} - g_{31}) + g_{23}(g_{31} - g_{32})\right)\end{pmatrix}
\end{aligned}$$

and

$$g_{1k} = \frac{\mu}{\sqrt{2\pi}(k_s - 1)}\left((1 + k_s)I\alpha d_k + (3 - k_s)n_k\right) \tag{12}$$

$$g_{2k} = \frac{\mu}{\sqrt{2\pi}(k_s - 1)}\left((3 - k_s)I\alpha d_k + (1 + k_s)n_k\right) \tag{13}$$

$$g_{3k} = \frac{\mu}{\sqrt{2\pi}}\left(n_k d_k + I\alpha\right) \tag{14}$$

Here, $k_s = 3 - 4\nu$ is for plane strain and $k_s = (3-\nu)/(1+\nu)$ for plane stress. So the total stress components can be expressed as

$$\sigma_{yy}(x,y) = \frac{1}{\sqrt{2\pi}}\int_{-\infty}^{+\infty}\left(\begin{array}{l}\sum_{k=1}^{4} g_{2k}\, C_k^0(\alpha)\exp\left(n_k y + I\alpha x\right) + \\ \sum_{i=1}^{N}\sum_{l=1}^{2} F_l^i(\alpha)\sum_{k=1}^{4}\sum_{r=1}^{3} b_{2r}^{i1} g_{rk}^1 \frac{h_{kl}}{h}\exp\left(n_k y^i + I\alpha x^i\right)\end{array}\right)d\alpha$$

$$\sigma_{xy}(x,y) = \frac{1}{\sqrt{2\pi}}\int_{-\infty}^{+\infty}\left(\begin{array}{l}\sum_{k=1}^{4} g_{3k}\, C_k^0(\alpha)\exp\left(n_k y + I\alpha x\right) + \\ \sum_{i=1}^{N}\sum_{l=1}^{2} F_l^i(\alpha)\sum_{k=1}^{4}\sum_{r=1}^{3} b_{3r}^{i1} g_{rk}^1 \frac{h_{kl}}{h}\exp\left(n_k y^i + I\alpha x^i\right)\end{array}\right)d\alpha \tag{15}$$

Here b_{jk}^{il} is the irow, jcolumn component of matrix $\mathbb{B}_l^i$.

Consider the boundary and continuous conditions described in Eq. (6) - Eq. (8), the singular integral equations can be obtained as following

$$\begin{aligned} R_2^i \int_{-a^i}^{a^i} \frac{D_2^i(t)}{t-x^i} dt + \sum_{j=1}^{N}\sum_{l=1}^{2} \int_{-a^j}^{a^j} w_{2l}^j(t, x^j, 0) D_l^j(t) dt = -\sqrt{2}i\delta_1^i \sigma(x^1) \\ R_3^i \int_{-a^i}^{a^i} \frac{D_1^i(t)}{t-x^i} dt + \sum_{j=1}^{N}\sum_{l=1}^{2} \int_{-a^j}^{a^j} w_{3l}^j(t, x^j, 0) D_l^j(t) dt = -\sqrt{2}i\delta_1^i \tau(x^1) \end{aligned} \tag{16}$$

Here

$$w_{jl}^i(t, x^i, 0) = \int_{-\infty}^{+\infty} \left(r_{jl}^i(t, \alpha, x^i, 0) - \delta_l^j \frac{\alpha R_l^i}{|\alpha|} \exp(-I\alpha t) \right) d\alpha, (j = 2,3) \tag{17}$$

$$\begin{aligned} &r_{Jl}^i(t, \alpha, x^i, y^i) = \\ &\sum_{k=1}^{4}\sum_{j=1}^{3} b_{jj}^{j2} g_{jk} \exp \begin{pmatrix} n_k \left(a_{21}^{i1}(x_c^i + x^i) + a_{22}^{i1}(y_c^i + y^i) \right) + \\ I\alpha \left(a_{11}^{i1}(x_c^i + x^i) + a_{12}^{i1}(y_c^i + y^i) \right) \end{pmatrix} s_{kl}^i(\alpha) \exp(-I\alpha t) \\ &+ \sum_{K=1}^{N}\sum_{k=1}^{4}\sum_{r=1}^{3}\sum_{i=1}^{3} b_{jr}^{i2} b_{rj}^{i1} g_{jk} \frac{h_{kl}}{h} \exp(n_k y^i + I\alpha x^i) \end{aligned} \tag{18}$$

$$C_k^0(\alpha) = \sum_{i=1}^{N}\sum_{l=1}^{2} s_{kl}^i(\alpha) F_l^i(\alpha) \tag{19}$$

R_l^i is a constant. The value of the integral in Eq. (17) can be derived using Gaussian integral method.

Solution of singular integral equations and the initial cracking angle

In this paper, the numerical solution of the singular integral Eq. (16) will be obtained by using the method described in Ref.15. According to the theory, $D_l^i(t)$ can be written as

$$D_l^i(t) = \frac{W_l^i(t)}{\sqrt{(a^i)^2 - t^2}}, l = 1,2 \tag{20}$$

$W_l^i(t) = \sum_{i=0}^{\infty} c_i^l P_i^{(\beta,\gamma)}(t/a^i)$, c_i^l are unknown coefficients, $P_i^{(\beta,\gamma)}(x)$ are Jacobi polynomials. So the stress intensity factors only calculated at the upper tip of the ith crack are as following

$$K_{11} = \lim_{x^1 -> a} \sqrt{a^1 - x^1}\, \sigma_{x^1 y^1}(x^1, 0) = \frac{1}{\sqrt{\pi}} R_2^1 c_i^1 P_i^{(\beta,\gamma)}(1), \tag{21}$$

$$K_{12} = \lim_{x^1 -> a} \sqrt{a^1 - x^1}\, \sigma_{y^1 y^1}(x^1, 0) = \frac{1}{\sqrt{\pi}} R_3^1 c_i^1 P_i^{(\beta,\gamma)}(1) \tag{22}$$

In Ref.16, Moes pointed out that the asymptotic near-tip circumferential and shear stresses in the local polar coordinate system take the following form under general mixed-mode loadings

$$\begin{aligned} \begin{pmatrix} \sigma_{\theta\theta} \\ \sigma_{r\theta} \end{pmatrix} = \frac{K_I}{\sqrt{2\pi r}} \frac{1}{4} \begin{pmatrix} 3\cos(\theta/2) + \cos(3\theta/2) \\ \sin(\theta/2) + \sin(3\theta/2) \end{pmatrix} \\ + \frac{K_{II}}{\sqrt{2\pi r}} \frac{1}{4} \begin{pmatrix} -3\sin(\theta/2) - 3\sin(3\theta/2) \\ \cos(\theta/2) + 3\cos(3\theta/2) \end{pmatrix} \end{aligned} \tag{23}$$

Use the maximum circumferential stress criterion, which states that the crack will propagate from its tip in a direction θ_c so that the circumferential stress $\sigma_{\theta\theta}$ is maximum. The circumferential stress in the direction of crack propagation is a principal stress. Therefore, the critical angle θ_c defining the radial direction of propagation can be determined by setting the shear stress in Eq. (23) to zero. After a few manipulations, the initial cracking angle can be obtained as following

$$\theta_c^1(a^i, x_c^i, y_c^i, \theta^i) = 2\arctan\left(\frac{1}{4} \left(\frac{K_{11}}{K_{12}} - \mathrm{sign}(K_{12}) \sqrt{8 + \left(\frac{K_{11}}{K_{12}} \right)^2} \right) \right) \tag{24}$$

θ_c^1 is the initial cracking angle at $x^1 = a^1$. To investigate the variation of θ_c^1 with the angle θ^i, the distance h^i which is from the upper tip of the ith crack to the upper boundary of the strip. In Eq. (24), we make some simple variable substitutions which are described as following

$$\eta^i = x_c^1 - x_c^i, \varsigma^i = y_c^1 - y_c^i, y_c^1 = a^1 \sin\theta^1 + h^1, (\eta^i, \varsigma^i \geq 0) \tag{25}$$

Results and Discussions

To investigate the validity of the method described above, here consider a simple example which is a homogeneous strip with two cracks (See Fig.2). The cracks are under constant normal traction σ_0. The normalized stress intensity factors of the left crack are only calculated and compared with that obtained in Ref. 18. The agreement of the results in Table 1 shows that the above method is believable.

TABLE 1. STRESS INTENSITY FACTOR FOR A STRIP WITH TWO CENTERLINE CRACKS

2l	x_c	Zhou et al.		Present	
		$K_{IL1}\sqrt{\pi}/\sigma_0$	$K_{IR1}\sqrt{\pi}/\sigma_0$	$K_{IL1}\sqrt{\pi}/\sigma_0$	$K_{IR1}\sqrt{\pi}/\sigma_0$
0.9	0.55	1.88188	2.12466	1.88102	2.12473
0.8	0.6	1.67217	1.65257	1.67292	1.65288
0.7	0.65	1.48364	1.44443	1.48392	1.44451
0.6	0.7	1.29357	1.27218	1.30058	1.27263
0.5	0.75	1.10538	1.09732	1.105221	1.09786
0.4	0.8	0.924887	0.922574	0.925002	0.922697
0.3	0.85	0.753472	0.752981	0.753918	0.753008
0.2	0.9	0.585505	0.585439	0.585814	0.585392
0.1	0.95	0.400829	0.400826	0.401258	0.401214

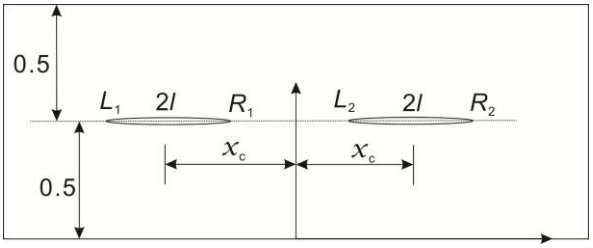

FIGURE 2. CONFIGURATION OF A STRIP WITH TWO CENTERLINE CRACKS

In the following content, we propose two examples to show the influence of θ^i and h^1 on θ_c^1. The strip is also with two cracks, i.e. $N = 2$. For simplicity, we set H to be unit 1 and all crack half length to be 0.1, then other length parameters become the ratio coefficients about H. The first case is the strip with a single crack and the second is with two cracks. The material of the strip is Al.

θ^1 and h^1 on θ_c^1

The variation of θ_c^1 versus h^1 and θ^i is presented in Fig.3 (a). The result shows that no matter increasing h^1 or θ^1 for the same crack orientation will both decrease the initial cracking angle θ_c^1, and it also demonstrates that the cracking direction tends to free boundary. Fig.3 (b) shows the influence of the existence of other cracks to θ_c^1. Here only the case, $\theta^1 = 0$, is investigated. The result illustrates that the initial cracking angle will increase when η^2 becomes bigger or θ^2 becomes smaller. The interaction of cracks may be negligible when the distance between the two crack centers is larger than ten times of the half length of the cracks. The variation of θ^2 also has influence on θ_c^1 but it is non-significant.

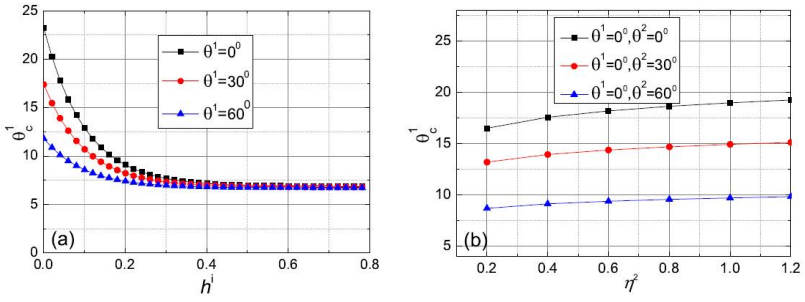

FIGURE 3. VARIATION OF THE INITIAL CRACKING ANGLE

ACKNOWLEDGEMENT

This work is supported by Shaanxi Province Department of Education Fund (12JK0968).

REFERENCES

[1] T. S. Cook and F. Erdogan, Stresses in bonded materials with a crack perpendicular to the interface, Int. J. Eng. Sci. 10, pp.677-697 (1972).

[2] F. Erdogan, Fracture mechanics of functionally graded materials, Compos. Eng. 5, (1995).

[3] F. Erdogan and M. Ozturk, Periodic cracking of functionally graded coatings, Int. J. Eng. Sci. 33, (1995).

[4] F. Erdogan and B. H. Wu, The surface crack problem for a plate with functionally graded properties, J. App. Mech. Trans. ASME. 64, pp.449-456 (1997).

[5] S. Dag and F. Erdogan, A surface crack in a graded medium under general loading conditions, J. Appl. Mech. Trans. ASME 69, pp. 580-588 (2002).

[6] L. C. Guo, L. Z. Wu, T. Zeng and L. Ma, Mode I crack problem for a functionally graded orthotropic strip, Euro. J. Mech. A-solids 23, pp. 219-234 (March 2004).

[7] L. C. Guo, L. Z. Wu and T. Zeng, The dynamic response of an edge crack in a functionally graded orthotropic strip, Mech. Res. Commun. 32, pp.385-400 (July 2005).

[8] F. Erdogan, Mixed boundary value problems in mechanics of materials, Multiscale and Functionally Graded Materials 973, Univ Illinois, Urbana Champaign; Univ Virginia; Fed Univ Rio de Janeiro (2008).

[9] M. Ben-Romdhane, S. El-Borgi and M. Charfeddine, An embedded crack in a functionally graded orthotropic coating bonded to a homogeneous substrate under a frictional hertzian contact, Int. J. Solids Struct. 50, pp.3898-3910 (November 2013).

[10] S.-H. Ding and X. Li, The collinear crack problem for an orthotropic functionally graded coating-substrate structure, Arch. .Appl. Mech. 84, pp.291-307 (March 2014).

[11] G. C. Sih and E. P. Chen, Crack propagation in a strip of material under plane extension, Int. J. Eng. Sci. 10, pp.537-551 (1972).

[12] G. Sih, Some basic problems in fracture mechanics and new concepts, Eng. frac. mech. 5, pp.365-377 (1973).

[13] M. Hussain, S. Pu and J. Underwood, Strain energy release rate for a crack under combined mode I and mode II, Frac. Analy. 560, pp.2-28 (1974).

[14] C. H. Wu, Fracture under combined loads by maximum-energy-release-rate criterion, J. Appl. Mech. Trans. ASME 45, pp.553-538 (1978).

[15] S. Krenk, On quadrature formulas for singular integral equations of the first and second kind, Quart. Appl. Math. 33, 225 (1975).

[16] N. Moes, J. Dolbow and T. Belytschko, A finite element method for crack growth without remeshing, Int. J. Numer. Methods Eng. 46, pp.131-150 (1999).

[17] M.-J. Zhou, S. Cen, Y. Bao and C.-F. Li, A quasi-static crack propagation simulation based on shape-free hybrid stress-function finite elements with simple remeshing, Compu. Methods Appl Mech. Eng. 275, pp.159-188 (2014).

[18] Z.-G. Zhou, Y.-Y. Bai and X.-W. Zhang, Two collinear griffith cracks subjected to uniform tension in infinitely long strip, Int. J. Solids Struct. 36, pp.5597-5609 (1999).

Ethylenediamine Modification of Hierarchical Mesoporous Carbon for the Effective Removal of Pb(II) and Related Influencing Factors

Y. B. Li[1], K. Q. Li[2]*, X. H. Wang[3], J. Li[4]

[1,2,3] College of Engineering, Nanjing Agricultural University, Nanjing, 210031, China

[4] School of Environmental Science and Engineering, Zhejiang Gongshang University, Hangzhou, 310012, China

kqlee@njau.edu.cn

Abstract

The polyamine groups were successfully modified in the pores of hierarchical mesoporous bagasse carbon through nitric acid oxidation and ethylenediamine(EDA) polymerisation. The influence of nitric acid concentration, oxidation time, EDA dosage, and modification time on the Pb(II) adsorption ability of the modified mesoporous carbon were discussed in an L9(34) orthogonal experiment as well as the adsorption characteristics and mechanisms. The results suggested that EDA modification conditions significantly affected the Pb(II) adsorption ability. The modified carbons, under different conditions, showed a Pb(II) adsorption difference of 35%; the nitric acid concentration exerted the greatest influence, followed by EDA dosage, and modification time. The carboxylic acid group content in the pores of the biomass carbon was proved as the key agent controlling the Pb(II) adsorption ability of the modified carbon. The Pb(II) adsorption was consistent with the Langmuir model, suggesting that the energy was distributed evenly on the surface of the modified carbon.

Keywords

Porous Carbon; EDA; Orthogonal Adsorption; Lead Ion

Introduction

Owing to its developed pore structure, natural characteristics, and environmentally protective properties, activated carbon has been widely applied to fields including air purification, water treatment, poison protection, catalytic carrier, solvent decolourisation, etc..1-3Lead is one of the common elements used in a variety of industrial processes. Lead ions are toxic, non-biodegradable, and can lead to the anaemia, nerve dysfunction, renal injury, etc. once entering the human body through the food chain.4 Therefore, lead is listed as a priority pollutant which should be controlled in water in many countries.5-6 Adsorption is favoured by researchers due to its advantages such as the recycling ability for valuable metals, good selectivity, and ease of use.7-9 Activated carbon's adsorption to heavy metals is both environmentally friendly and convenient.

Surface chemistry is important in the adsorption by activated carbon of heavy metals. During the adsorption process, the functional groups on the external surface, or in the pore surface of the activated carbon, chemically react with heavy metals through ion exchange or chelation.10 Since the chemical actions are different owing to differences in the functional groups on the surface, the adsorption ability of activated carbon to specific metal ions can be effectively improved by functional groups with corresponding adsorption ability.11-13 Research has proved that the alkaline groups introduced on the surface of activated carbon can provide it with alternative surface diversity and meet requirements for the wider application in separation, catalysis, material science, biotechnology, etc..11 Xie12 found that the adsorption ability of starch to Pb(II) was greatly enhanced after EDA modification; Gao13 successfully prepared a polyamine chelating resin through diethylenetriamine(DETA) modification and found that the resin prepared presented a favourable Cu(II) adsorption performance; Zhang14 et al. successfully grafted amino functional groups onto the surface of the resin. The Cd2+ and Ni2+ adsorption abilities of the resin obtained were greatly strengthened; Li15 pointed out that EDA modification effectively enhanced the adsorption properties of biomass-based mesoporous carbon for lead.

This study prepared biomass activated carbon with high and medium porosity using bagasse as the raw material, phosphoric acid as an activating agent, and a one-step activation method. Through an L9 (34) orthogonal

2226-4523/16/01 058-8 © 2016 DEStech Publications, Inc.
doi:10.12783/ijmsci.2016.0601.06

experiment, it further discussed the influences of nitric acid concentration, oxidation time, EDA dosage, and modification time on the Pb(II) adsorption ability of biomass-based carbon with EDA modification and related influencing mechanisms. Moreover, the properties and mechanisms in biomass-based bagasse carbon samples with polyamine modification which affected the Pb(II) adsorption isotherm were analysed under different conditions according to the orthogonal experimental data. The results obtained would provide data support and a theoretical basis for preparing polyamine-modified biomass carbon with high Pb(II) adsorption.

Experimental Procedure

Reagent and Instrument

The chemical reagents used, including bagasse, phosphoric acid, nitric acid, EDA, N, N- dicyclohexyl carbon phthalimide(DCC), and lead nitrate, were all analytically pure. The water used was deionised. The main instruments used included an Amicus X-ray photoelectron spectrometer (SHIMADZU) and the TENSOR27 FT-IR infrared spectrometer produced by Bruker, Germany, the 3H-2000Ps2 specific surface and pore size analyser (Beijing Persee Instrument Technology Co., Ltd), a flame atomic adsorption spectrophotometer (A3 Type, Beijing Purkinje General Co.), an intelligent microwave carbon material preparation system (Nanjing Yudian Automation Technology Co., Ltd), a pH meter (PHS-2C, Shanghai Kang Instrument Co., Ltd), and a collector type magnetic stirrer (DF- II, Jintan Jinxianglong Electronics Co., Ltd), etc..

Preparation of the Material

After shining, cleaning, and drying, the bagasse was crushed using a pulveriser and sieved through a 50 mesh sieve. Then 20 g of bagasse was dipped into a phosphoric acid solution in the ratio 1:1.5 (by mass) and then dried at 105 °C for 6 h. The bagasse thus obtained was activated in a tube furnace at 500 °C for 90 min under the protection of a nitrogen gas flow and subjected to atemperature increase at a rate of 5°C·min -1. The activated samples were first rinsed for 3 h using hydrochloric acid (0.1 mol·L-1) and then washed using distilled water to pH > 7. After drying, the activated carbon obtained was ground and sieved via a 100 mesh to obtain the mesoporous carbon bagasse biomass. The biomass carbon obtained showed a methylene blue value of 220 mg·g-1, a BET specific surface area of 938 m2·g-1, a total pore volume of 1.49 cm3·g-1, and a mesoporous porosity of 90.7%.

Modification Method

The biomass-based carbon in bagasse was placed in a 10% hydrochloric acid solution and stirred for 5 h at 60 °C. Then it was washed using water until the pH was greater than 7 and then dried at 105 °C; subsequently, 5g dry activated carbon was added to a 300mL nitric acid solution at concentration of 17.5%, 20%, 32.5% and was oxidized at 60 °C for 3 to 5 h; 5 g of the oxidized biomass-based mesoporous carbon was dispersed into 125, 150, 175 mL of EDA, respectively. The mixture was stirred until uniform. Subsequently, the mixture solution acquired was dosed with 5 g DCC and stirred for 24 h to 48 h at 120°C under refluxing conditions. After being filtered and rinsed using ethanol and ether, the prepared sample was dried for 8 h at 80 °C. The polyamine-modified activated carbon was obtained.

The reaction mechanism of the polyamine modification was listed as follows:

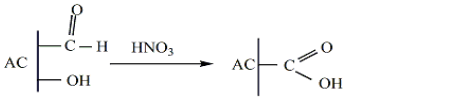

(1)

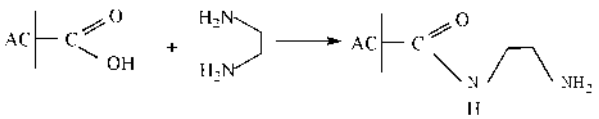

(2)

In order to investigate the effects of the preparation parameters on the Pb2+ adsorption of the polyamine-modified activated carbon, an L9(34) orthogonal array with four parameters and each in three levels was established. Three levels (L1, L2, and L3) of each investigated operational parameter were listed as follows, respectively: nitrate acid concentration(parameter A), oxidation time(parameter B), EDA dosage(parameter C), and EDA modification time(parameter D). The L9(34) orthogonal array, parameters and their values corresponding to their levels to be

studied in this work are shown in Table 1.

TABLE 1. L9 (34) ORTHOGONAL ARRAY, PARAMETERS AND THEIR VALUES CORRESPONDING TO THEIR LEVELS

Parameters	levels		
	1	2	3
A. Nitrate acid concentration/%	17.5	25	32.5
B. oxidation time/ h	3	4	5
C. EDA dosage/mL	125	150	175
D. modification time/ h	24	36	48

Characterisation

The pore structure of the samples was measured using a low nitrogen adsorption/desorption method and the 3 H-2000 Ps2 specific surface and pore-size analyser produced by Beijing Persee Instrument Technology Co., Ltd at 77 K and a relative pressure (P/P0) of 10-3 to 1.0. Before the test, the samples were degassed at 300 °C for 12 h. The total specific surface of the mesoporous carbon was calculated using the BET method, while the mesoporous volume (VH-K) and micropore volume (VBJH) of the mesoporous carbon were computed using the Horvath-Kawazoe (H-K) equation and the BJH equation. The sum of the mesoporous volume (VH-K) and micropore volume (VBJH) was noted as the total volume (Vtotal). The overall pore size distribution of the mesoporous carbon was characterized using the DFT equation. The BET specific surface area and total pore volume were 816 m2·g-1 and 1.184 cm3·g-1, respectively; the pore volume of the mesopore/total pore volume was as high as 89%. Thus, the sample I8 was mesoporous. The surface area, pore volume and mesoporosity of modified I8 were decreased to 721 m2·g-1, 0.784 cm3·g-1 and 73%, respectively. The data showed that the modified carbon I8 belonged to typical mesopourous carbon too.

A PHI 5000 Versa Probe type X-ray photoelectron probe (Ulvac-Phi Co., Japan) was used to measure the XPS spectrograms of the mesoporous biomass carbon and polyamine-modified biomass carbon before and after Pb(II) ion adsorption

Adsorption

$$Q_e = V(C_0 - C_e)/m \quad (3)$$

where, C0 and Ce are initial, and adsorption equilibrium, concentrations of adsorbate in solution (mg·L-1) respectively; V is the volume of solution (L); m is the mass of absorbent (g).

Results and Discussion

The Effects of Modifying Parameters the Adsorption

Research shows that EDA modification can greatly enhance the Pb(II) adsorption ability of the mesoporous carbon, and polyamine groups played a major role in the adsorption.15, 16 However, sufficient carboxylic groups should be modified on the surface of the carbon before EDA can be effectively grafted onto the surface of carbon through the copoly-condensation reaction as shown in equations (1) and (2). The grafting effectiveness of the EDA on the carbon is subject to many factors such as nitrate acid concentration, oxidation time, EDA dosage, and modification time. According to the orthogonality principle, an L9(34) orthogonal table was designed to analyse the influences of the factors on Pb(II)adsorption ability (see Table 1).

Table 2 lists the analytical results of the orthogonal experiment on the EDA-modified bagasse carbon. As shown in table 2, the EDA-modified carbon samples I1-I9 presented a much higher Pb(II) adsorption capacity than the pristine bagasse carbon I, which proved that the EDA modification significantly enhanced the Pb(II) adsorption capacity of bagasse mesoporous carbon. The adsorption amount increased for the modified carbon from 37 mg·g-1 for I5 to the highest 85 mg·g-1 for I8 than the pristine carbon I. This result indicated that the type and level of modification parameter have a great effect on the adsorption capacity. The values of k and R from range analysis can reflect the extent of influence of the parameter type and level on the Pb(II) adsorption, respectively. Through comparing R values for different parameters, it can be inferred that nitrate acid concentration exerted the largest

influences, followed by EDA dosage, EDA modification time and nitric oxidation time in turn. The optimum level of the influence factors were determined as A1B3C1D3 under prevailing experimental conditions according to k value, indicating that the most suitable modification conditions were at nitric acid concentration of 17.5%, nitric acid oxidation time of 5 h, EDA dose of 125 mL, and EDA modification time of 48 h.

TABLE 2. ORTHOGONAL EXPERIMENTAL DESIGN AND RANGE ANALYSIS

N.	Nitrate acid concentration /%	Nitrate acid oxidation time/h	EDA dosage /mL	EDA modification time/h	Adsorption amount /mg·g-1
I	…	…	…	…	100
I1	17.5	3	125	24	175
I2	17.5	4	150	36	181
I3	17.5	5	175	48	175
I4	25	3	150	48	163
I5	25	4	175	24	137
I6	25	5	125	36	164
I7	32.5	3	175	36	164
I8	32.5	4	125	48	185
I9	32.5	5	150	24	177
k1	177	167	175	163	…
k2	155	168	174	170	…
k3	175	172	159	174	…
R	22	5	16	11	…

Influence of Solution Ph

Fig.1 shows the influence of pH value on the Pb(II) adsorption ability of the EDA-modified carbon I8. The Pb (II) adsorption ability increased sharply at pH<5.0, stabilized at pH 5.0-8.0, and slowly deceased at pH>8.0. The point of zero charge value of the modified carbon is about 4.9. At pH<pHpzc, the surface charge of the modified carbon was positive due to the protonation reaction. Obviously, lower positively charged amino groups would come into being at higher solution pH since more H+ desorbed from the carbon, which was helpful for coordination by the modified carbon because of electrostatic repulsion. However, at pH> pHpzc, the surface charge of the modified carbon was negative because of the adsorption of OH- ions through hydrogen bond at high pH. Although the solution pH had some effect on Pb(II) adsorption, the capacity was stable in the range of pH 5.0 to 8.0. The slow decrease of Pb(II) removal was attributed to the precipitation reaction of Pb(II).

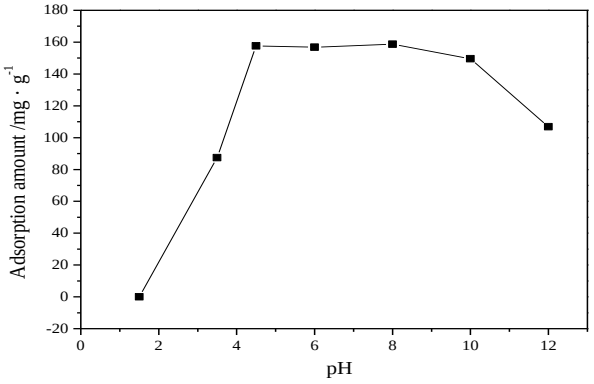

FIGURE 1. THE EFFECT OF PH VALUE ON Pb(II) ADSORPTION ON CARBON I8 (CARBON DOSE 0.02 g, SOLUTION VOLUME 100 mL, INITIAL Pb(II) CONCENTRATION 30 mg·L-1, SOLUTION TEMPERATURE 25 °C)

Adsorption Characteristics

Fig. 2 compares the Pb(II) adsorption ability of the pristine carbon I and the modified carbon I5 and I8. As shown in Fig.5, the adsorption capacity of I5 and I8 were higher than that for I, which indicated that modification can greatly enhance the Pb(II) adsorption ability of bagasse carbon. In addition, the Pb(II) adsorption ability of I8 was superior to that of I5, which implied that the adsorption capacity of EDA-modified carbon varied with its modification parameters.

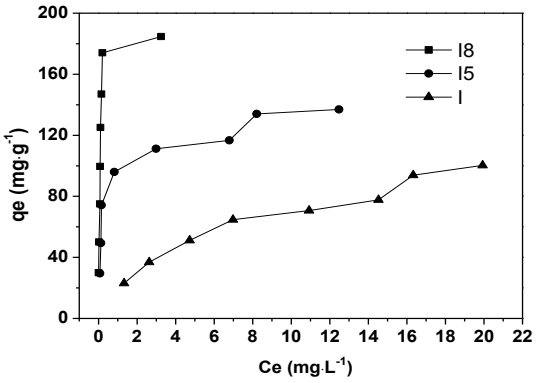

FIGURE 2. ADSORPTION ISOTHERMS OF Pb(II) ON CARBON I, I5 AND I8 (CARBON DOSE 0.02 G, SOLUTION VOLUME 100 mL, INITIAL Pb(II) CONCENTRATION 30 MG·L-1, SOLUTION TEMPERATURE 25 °C, SOLUTION pH 4.5)

The isothermal experimental data were fitted with the well-known models of Langmuir and Freundlich to investigate the adsorption mechanisms of Pb(II) onto bagasse carbon before and after modification. The linearised Langmuir and Freundlich isotherm equations are given as follows.

$$\frac{Ce}{q_e} = \frac{Ce}{q^0} + \frac{q^0}{b} \tag{4}$$

$$\lg q_e = \frac{1}{n}\lg Ce + \lg K \tag{5}$$

Where Ce is the equilibrium solution concentration (mg·L -1) and qe is the amount of Pb(II) adsorbed onto adsorbent at equilibrium (mg·g-1). q0 and b are the Langmuir constants related to the adsorption capacity (mg·g-1) and energy of adsorption (L·mg-1) respectively. K and n are the Freundlich constants related to adsorption capacity and energy of adsorption respectively.

Figures 3a and 3b show the fitting curves of the Pb(II) adsorption isotherm on I, I5 and I8 based on Langmuir and Freundlich respectively. The corresponding fitting parameters are shown in Table 3.

It was found that higher values of correlation coefficient R2 were fitted by the Langumir model than that by Freundlich equation for the modified carbon I5 and I8. However, the opposite was true for the pristine carbon I. The results implied that the Pb(II) adsorption on the modified carbon could be described well by Langumir while the Freundlich fitted well the adsorption for the pristine carbon. The Langmuir isothermal model was mainly applied to monomolecular layer adsorption of an adsorbent with a uniform surface. Moreover, the absorbed molecules were independent.24 The Freundlich isotherm model was suitable when describing heterogeneous adsorption.25, 26 In accordance with the fitted results, the Pb(II) adsorption ability of the modified carbon samples was in line with the homogeneous type assumed by the Langmuir model, with equilibrium energy distribution on the surface. This result proved that the EDA modified carbon mainly functioned through internal chemical adsorption on a monolayer. The saturated adsorption capacities, fitted by the Langmuir model, were 137 mg·g-1 for I5 and 189 mg·g-1 for I8, respectively, which were in agreement with actual conditions. Carbon sample I showed both a better goodness of fit for the Freundlich, suggesting that the Pb(II) adsorption on I was heterogeneous.24-26

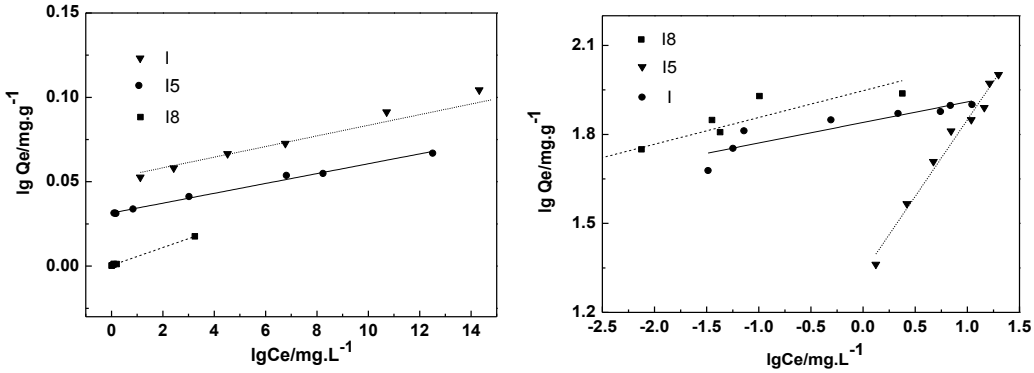

FIGURE 3. LANGUMIR AND FREUNDLICH FIT OF ADSORPTION EQUILIBRIUM DATA OF Pb(II) ON I, I5 AND I8

TABLE 3. ISOTHERM PARAMETERS FOR PB(II) ADSORPTION ONTO CARBON I AND EDA-MODIFIED CARBON I5 AND I8

Model	Model isotherm equation	Parameter	I	I5	I8
Langmuir	$\frac{Ce}{q_e}=\frac{Ce}{q^0}+\frac{q^0}{b}$	q0/ mg·g-1	127	137	189
		b/L·mg-1	2337	49453	527420
		R2	0.960	0.993	0.999
Freundlich	$\lg q_e=\frac{1}{n}\lg Ce+\lg K$	K/ L·mg-1	22	82	173
		n	1.936	4.209	3.233
		R2	0.981	0.829	0.815

XPS Analysis

The surface properties of I8, modified I8, and modified I8 after absorbing Pb(II) were investigated through XPS analysis. This technique not only could provide elemental analysis of carbon, oxygen, lead and other elements, but also offer valuable information about the valence state of adsorbed ions by analyzing the chemical shift in binding energies. The survey spectra are shown in Fig. 8. The XPS spectrums for all samples showed that carbon, oxy-gen were the predominant elements observed on the surface from binding energies at 289 eV (C 1s) and 535 eV (O 1s). The N 1s peak appeared in the modified I8 sample at the location where the binding energy was 400eV. This result implied that after being modified, ethylenediamine was successfully modified on the surface of I8. Lead peaks (138 and 436 eV) were also observed in the spectra after exposure to lead solution, suggesting that lead was absorbed on the surface of I8. Moreover, after the absorption reaction, the N 1s peak displayed an obvious right shift, which implies that a reaction occurred between modified carbon I8 and Pb(II) and that the polyamine group had an important function in the adsorption process.

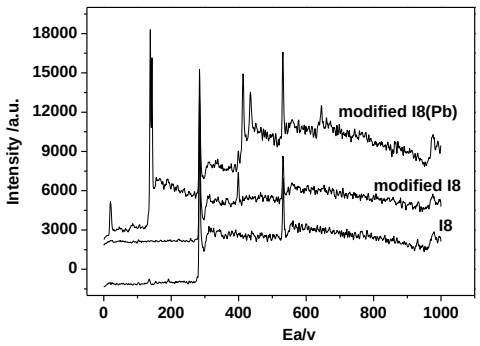

FIGURE 4. XPS OF I8, MODIFIED I8 BEFORE AND MODIFIED I8 AFTER PB(II) ADSORPTION

Conclusions

Bagasse carbons were modified with EDA for adsorbing Pb(II) from aqueous solution by nitric acid oxidation and EDA polymerisation. The effects of concentration of nitric acid, nitric acid oxidation time, EDA dosage, and EDA reaction time on the adsorption of Pb(II) on the modified mesoporous carbon were investigated. The results showed that the modification conditions of EDA greatly influenced the Pb(II) adsorption ability. The optimal modification conditions are at nitric acid concentration of 17.5%, nitric acid oxidation time of 5 h, EDA dose of 125 mL, and EDA modification time of 48 h according to the result of an L9(34) orthogonal experiment. The EDA-modified carbon I8, prepared under optimal conditions, achieved a Pb(II) adsorption ability of 185 mg·g-1, which was 85% higher than the pristine I8. The range analysis showed that nitrate acid concentrate has the most influence on Pb(II) adsorption ability, followed by EDA dosage, EDA modification time, and nitrate acid oxidation time in turn. Before modification, the isotherm for Pb(II) adsorption of carbon I was in line with the Freundlich isotherm model, while those of EDA modified carbons I5 and I8 were consistent with the Langmuir isotherm model. This result suggested that the Pb(II) adsorption on the modified carbon was mainly monomolecular with a uniform energy distribution on the surface.

ACKNOWLEDGMENTS

The authors gratefully acknowledge the research grant provided by China under the Natural Science Foundation (No. 51102136), and the Doctoral fund of Ministry of Education of China financial (No. 20110097120021) and China Postdoctoral Science Fund (No. 2014M560429).

REFERENCES

[1] R. X. Guo and B. H. Li, Progress of application of activated carbon in water treatment, on overview, Carbon Techniques, 25(1), pp.20-24(2006).

[2] P. Li, Application of active carbon adsorption in industrial wastewater treatment, Technology and Enterprise, 21, 316(2013).

[3] B. J. Deng, C. X. Li and H. M. Li, Influence of ACF by different pretreatment on iodine adsorption, Carbon, 4, pp.36-37(2006).

[4] H. Y. Chen, Y. J. Yang, Z. J. Zhang, et al, Effects of the preparation conditions of municipal ewage sludge-bentonite adsorbent on adsorption of Pb2+, Chemical Research and Application, 22(6), pp.800-804 (2010).

[5] E. F. Dong, J. Yao, Key problems discussion on environment impact evaluation of lead-acid battery project, Chemical Engineering &Equipment, 3, pp.167-170(2011).

[6] Benjamin M, Leckie JO, Multiple-site adsorption of Cd, Cu, Zn and Pb on amorphous iron ox hydroxide, Colloid Interface Sic, 79(3), pp.209-221(1981).

[7] W. Zhang, L. Yang, H. Y. Jiang, et al, Characterization of sludge-based activated carbon and its adsorption properties on Cr(VI) , Chinese Journal of Environmental Engineering, 8(4), pp.1439-1446(2014).

[8] H. Jin, Y. Xing, X. M. Sun, et al, Adsorption behaviour of pyromelliticdianhydride-modified chitosan microspheres for Pb2+ and Cd2+, Chinese Journal of Applied Chemistry, 26(5), pp.582-587(2009).

[9] W. F. Chen, M. T. Cheng, D. F. Zhang, et al, Granular activated carbon tailored by organic acid-Fe for arsenic removal, China Environmental Science, 31(6), pp.910-915(2011).

[10] X. Xu, B. Y. Liu, Z. D. Deng, Analysis of decisive parameters in activated carbon's adsorption of heavy metals, Energy Environmental Protection, 24(2), pp.48-50(2010).

[11] Y. L. Wang, D. L. Yin, Y. Xia, et al, Structure and properties of basic activated carbon modified with EDA, Carbon Techniques, 27(4), pp.22-25(2008).

[12] G. R. Xie, X. Q. Shang, R. F. Liu, et al, Adsorption of Pb (II) on copolymer of glycidylmethacrylete grafted on starch modified with EDA, CIESC Journal, 62(4), pp.970-976(2011).

[13] J. Gao, F. Q. Liu, L. J. Li, et al, Adsorption performances of a novel chelating polyamine resin towards copper(II) in aqueous, Ion Exchange and Adsorption, 29(2), pp.108-116(2013).

[14] Q. M. Zhang, S. R. Zheng, J. H. Wang, et al, Synthesis of amine resin and its adsorption properties for heavy metal ions in water, Chinese Journal of Environmental Engineering, 4(12), pp.2657-2661(2010).

[15] K. Q. Li, Y. J. Wang, M. R. Yang, et al, Adsorption kinetics and mechanism of lead (II) on mesoporous activated carbon, Environmental Science, 35(8), pp.3198-3205(2014).

[16] X. Y. Sun, G. Q. Wu, Q. S. Zhang, Adsorption of organic pollutions in micro-polluted water by bamboo charcoal, Environmental Science and Technology, 23 (1), pp.15-18(2010).

[17] Y. F. Yuan, Analysis of multi- target orthogonal experiment, Journal of Hubei Automotive Industries Institute, 19 (4), pp.53-56(2005).

[18] Z. Wang, L. Wei, mplementation of orthogonal experimental ANOVA in pharmaceutical experimental by SPSS, Journal of Mathematical Medicine, 27 (1), pp. 99-102(2014).

[19] Y. Yang, L. Li, Z. Y. Sun, et al, The research on the surface oxidation modification of activated carbon and its adsorption mechanisms of organic matter and heavy metal ions, Science Technology and Engineering, 12(24), pp.6132-6138, 6147(2012).

[20] Y. Xiao, C. Gao, Y. Y. Shi, et al, Synthesis and characterization of porous carbons materials containing quaternary phosphonium salt based on activated carbon, Chinese Journal of Inorganic Chemistry, 28 (6), pp.1222-1228(2012).

[21] L. H. Liu, M. Gu, X. F. Xian, Effect of pore structure and surface chemical properties on adsorption properties of activated carbons, Chinese Journal of Environmental Engineering, 6(4), pp.1299-1304(2012).

[22] F. Hou, M. Chen, M. Y. Tong, Influence of nitric acid modification on properties of active carbon, Chemistry& Bioengineering, 28 (5), pp.70-73, 76(2011).

[23] G. H. Meng, A. M. Li, Q. X. Zhang, Studies on the oxygen-containing groups of activated carbon and their effects on the adsorption character, Ion Exchange and Adsorption, 23(1), pp.88-94(2007).

[24] Langmuir I, The adsorption of gases on plane surfaces of glass, mica and platinum, Journal of American Chemistry Society, 40, pp.1361-1403(1918).

[25] Freundlich H M F, Over the adsorption in solution, Journal of Physical Chemistry, 57, pp.385-471(1906).

[26] Temkin M I, Kinetics of ammonia synthesis on promoted iron catalysts, ActaPhysiochim, URSS, 12, pp.327-356(1940).

[27] Suat U, Murat E, Turgay T, et al, Removal of lead(Ⅱ) and nickel(Ⅱ) ions from aqueous solution using activated carbon prepared from rapeseed oil cake by Na2CO3 activation, Clean Techn Environ Policy, 17, pp.747-756(2015).

[28] Plazinski W, Rudzinski W, Plazinska A, Theoretical models of sorption kinetics including a surface reaction mechanism: A review, Advances in Colloid and Interface Science, 152(1/2), pp.2-13(2009).

[29] S. Nethaji, A. Sivasamy, Removal of hexavalent chromium from aqueous solution using activated carbon prepared from walnut shell biomass through alkali impregnation processes, Clean Techn Environ Policy, 16, pp.361-368(2014).

[30] G. Venkatesan, U. Senthilnathan, ShameelaR., Cadmium removal from aqueous solutions using hybrid eucalyptus wood based activated carbon: adsorption batch studies, Clean Techn Environ Policy, 16, pp.195-200(2014).

[31] X.Liu, X. X. Xie, H. Yan, et al, A review of the adsorption of organic pollutants on mesoporous carbons and carbon/silica hybrids, Carbon, 64(0),557(2013).

[32] X.Yang, C. T. Lira, Modeling of adsorption on porous activated carbons using SLD-ESD model with a pore size distribution, Chemical Engineering Journal, 195/196, pp.314-322(2012).

[33] Kashif R, K. Suresh Kumar Reddy, Ahmed A. S, et al, Sulfur-impregnated porous carbon for removal of mercuric chloride: optimization using RSM, Clean Techn Environ Policy, 15, pp.1041-1048(2013).

Study on Green Supply Chain Coordination in ELV Recycling System with Government Subsidy for the Third-Party Recycler

Daqiang Chen[1*], Peiqi Mao[2], Danzhi Sun[3], Sasa Yang[4]

[1,2] School of Computer Science & Information Engineering, Zhejiang Gongshang University, Hangzhou, 310018, P.R. China, www.zjgsu.edu.cn

[3] Zhejiang Scientific Research Institute of Transport, Hangzhou, 310006, P.R. China

[4] School of Computer Science & Information Engineering, Zhejiang Gongshang University, Hangzhou, 310018, P.R. China

[1*]chendaqiang@zjgsu.edu.cn; [2]869831005@qq.com; [3]281148262@qq.com; [4]714680237@qq.com

Abstract

With the rapid increase of car ownership in China, the quality of the end-of-life vehicle (ELV) is growing rapidly. Since the ELV recycling is helpful for environmental protection and cost reduction of the enterprise in the green supply chain, it is important for the government to design a proper strategy to strengthen the goodness of the green supply chain coordination. In this paper, a green supply chain system with one supplier, one automobile manufacturer, one retailer, one third-party recycler and one government in automobile industry is suggested. In this green supply chain, the third-party recycler can sold the recycled parts that can be reused to manufacturers, sold the rest dismantled parts to the suppliers, and can get a subsidy from the government. Then, game theory was applied and two different scenarios were analyzed for different pricing strategies with government subsidy for the third-party recycler, i.e. an independent decision scenario and joint decision scenario by cooperative game model. Based on the pricing analysis of the third-party recyclers of closed-loop supply chain pricing, it is found that in the joint decision scenario the profit is higher than the non-cooperative decision scenario and the government subsidy has no effect on the coordination of the green supply chain in ELV recycling system, so in order to reduce the automobile production cost, obtain high corporate profits and social benefits, each part of the supply chain should try their best to cooperate, formulate the pricing strategy jointly and the government needs to design more effective strategy to involved in the coordination of green supply chain.

Keywords

Green Supply Chain; ELV Recycling; Government Subsidy; The Third-Party Recycler; Game Theory

Introduction

In recent years, with the rapid development of the economic and society, China has become the biggest automaker and the largest automobile market all over the world. According to China Automotive Industry Yearbook 2011, the production of motor vehicle and small passenger car were more than 18 million and 9 million.[1] Given the stricter regulation on the end-of-life vehicle (ELV) standard issued by the Ministry of Commerce in 2012, the number of ELVs will increase rapidly in next decades. Legislative ELV recycling systems were established in the EU, Japan, Korea, and US, especially in the US, ELV recycling is managed under existing laws on environmental protection.[2] As a significant part of renewable resources, the circulation of the scrap automotive recycling work is difficult to implement, and automobile recycling quantity is in deficiency.[3] The phenomenon that the scrap cars go into the market in an unfair way is more serious, which may not help the environment but discriminate arbitrarily and unjustifiably. In foreign countries, automotive recycling has aroused extensive attention due to environmental requirements, and also because there is a huge opportunity. But in China, due to people's different ideas, legislation lags behind, the domestic government also does not have the corresponding policy to support, resulting in ELV recycling have not been given the attention.

With the development of enterprises in today's world economy, some serve issues are explored, such as the massive resource consumption, the waste production beyond natural limits, and the absence of flows from waste to

2226-4523/16/01 066-6 © 2016 DEStech Publications, Inc.
doi:10.12783/ijmsci.2016.0601.07

resources, cause serious damage to the environment, especially in developing countries. In order to improve the resource utilization efficiency, increase profits, a proper treatment of the re-source and environment problems in the supply chain is particularly urgent and necessary. By now, there are many research methods for solving environmental problems in the supply chain. Green Supply Chain Management is an over-seas platform to promote green low carbon supplier management.[4] Now it has evolved into a fusion of traditional supply chain management idea and the concept of green environment independent integrated supplier re-source management platform.[5] Its main goal is to reduce resource consumption and waste generation at every stage of the supply chain. It uses the enterprise alliance game theory to achieve the target that a single enterprise can't achieve cost reduction or increase the profit of enterprises.[6]

In order to improve the utilization of non-renewable resources, reduce the production cost, the policy-makers can not only strengthen the management of ELV, but also can make the ELV recycling price increase, the quantity of ELV recycled improve and the pollution of the environment reduce by subsidies to the automotive recyclers or consumers. Such subsidies has been provided as financial and technical support for projects, such as the R&D government subsidies for SMEs' development and technical innovation, which caused great impact and promote the development of small and medium enterprises.[7]

Notations and Problem Description

Notations

The following notations are used for the following analysis.

D the demand function of the automobile market
α the price elasticity of the automobile market, where $\alpha<0$
β the initial demand of the automobile market
Q the quantity function of the ELV recycled from the automobile market
γ the price elasticity of the ELV recycled from the automobile market, where $\gamma<0$
q the initial quantity of the ELV recycled from the automobile market
δ_1 the profit margin of the directly reused part of the recycled ELV
δ_2 the profit margin of the dismantled part of the recycled ELV
λ_1 the rate of the directly reused part of the recycled ELV, where $\lambda_1 \in (0,1)$
λ_2 the rate of the dismantled part of the recycled ELV, where $\lambda_2 \in (0,1)$ and $\lambda_1 + \lambda_2 < 1$
c_{s1} the unit cost of the newly produced part by the automobile parts supplier
c_{s2} the unit cost of the part made from the dismantled part of the recycled ELV
c_{m1} the unit cost of the newly produced automobile by the automobile parts supplier
c_{m2} the unit cost of the automobile with parts from the third-party recycler
c_r the unit sale cost of automobile retailer of the automobile retailer
c_t the unit processing cost of ELV recycling of the third-party recycler
u the price of the automobile parts supplied of automobile parts supplier
w the whole price of the automobile sold to the automobile retailer
p_r the retail price of the automobiles in the market
p_c the recycling price of the third-party recycler for the recycled ELV
p_{tm} the prices of the directly reused part of the recycled ELV

p_{ts} the prices of the dismantled part of the recycled ELV
b the government subsidy for the third-party recycler

Problem Description and Model Assumption

In this paper, the closed-loop supply chain is composed of one supplier, one automobile manufacturer, one retailer, one third-party recycler and one government, as showed in Fig. 1. In this system, the third-party recycler can sold the reusable parts that can be re-used by the automobile manufacturer, and sold the rest dismantled parts to the suppliers, i.e. the third-party recycler has an ability of decomposition, and the recycled parts are partially and directly reused. And in order to improve the utilization rate of non-renewable resources, reduce the production cost of enterprise, the government can give a one-off subsidy to the third-party recycler, i.e. the third-party recycler will get a subsidy when it carry out its ELV recycling business and decompose the recycled ELV as the reusable parts and the rest dismantled parts.

Therefore, in this case, the price of the automobiles in the market, recycling price of the third-party recycler, the prices of the directly reused part of the recycled scrap automobile, the prices of the dismantled part of the recycled scrap automobile, the price of the automobile parts of the automobile parts sup-plier and the subsidy of the government should be analyzed to increase the profit of the node enterprises of this supply chain system.

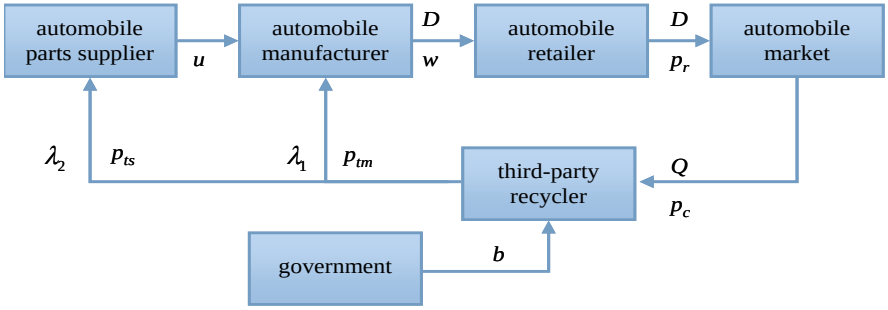

FIGURE 1. GREEN SUPPLY CHAIN COORDINATION IN ELV RECYCLING SYSTEM WITH GOVERNMENT SUBSIDY FOR THE THIRD-PARTY RECYCLER

In order to simplify the analysis, it is assumed that the recycled parts from the third-party recycler have the priority of being selected for reusing, and the unit production cost of the automobile parts made from the dismantled part of the recycled scrap automobile and newly produced are not equal.

Then the demand function of the market is addressed as $D=\alpha p_r+\beta$. The quantity function of the recycled ELV from the market is assumed as $Q=\gamma p_c+q$, the quantity of the dismantled parts and the quantity of the dismantled parts of the recycled ELV can be noted as $\lambda_1 Q$ and $\lambda_2 Q$ respectively. The ELV recycling price for the sale from third-party recycler to automobile manufacturers and the automobile parts supplier can be assumed as $p_{tm}=\delta_1 p_c$ and $p_{ts}=\delta_2 p_c$, respectively.

Under above hypothesis and analysis, for a given recycling prices value p_c, the profits of the automobile parts supplier, the automobile manufacturer, the automobile retailer, the third-party recycler, and total profit of the closed-loop supply chain system can be addressed as follows.

The profit of automobile parts supplier can be expressed as:

$$\pi_s=\left[\alpha p_r+\beta-\lambda_1(\gamma p_c+q)\right]u-\lambda_2(\gamma p_c+q)\delta_2 p_c-c_{s2}\lambda_2(\gamma p_c+q)-c_{s1}\left[\alpha p_r+\beta-\lambda_1(\gamma p_c+q)-\lambda_2(\gamma p_c+q)\right] \tag{1}$$

The automobile manufacturer's profit can be expressed as:

$$\pi_m=(\alpha p_r+\beta)w-\left[\alpha p_r+\beta-\lambda_1(\gamma p_c+q)\right]u-\lambda_1(\gamma p_c+q)\delta_1 p_c-c_{m2}\lambda_1(\gamma p_c+q)-c_{m1}\left[\alpha p_r+\beta-\lambda_1(\gamma p_c+q)\right] \tag{2}$$

The automobile retailer's profit can be expressed as:

$$\pi_r=(\alpha p_r+\beta)p_r-(\alpha p_r+\beta)w-(\alpha p_r+\beta)c_r \tag{3}$$

The third-party recycler's profit can be expressed as:

$$\pi_t = \lambda_1(\gamma p_c + q)\delta_1 p_c + \lambda_2(\gamma p_c + q)\delta_2 p_c - (\gamma p_c + q)p_c - (\gamma p_c + q)c_t \tag{4}$$

And the total system profit of the closed-loop supply chain can be noted as:

$$\pi^{**} = \pi_s + \pi_m + \pi_r + \pi_t \tag{5}$$

Model Formulation and Analysis

Joint Decision Scenario

Under the joint decision situations situation, the total profits of the closed-loop supply chain system can be expressed as:

$$\begin{aligned}\pi^{**} &= \pi_s + \pi_m + \pi_r + \pi_t \\ &= -\gamma p_c^{\,2} + \left(\lambda_1\gamma c_{s1} + \lambda_2\gamma c_{s1} + \lambda_1\gamma c_{m1} - \lambda_2\gamma c_{s2} - \lambda_2\gamma c_{m2} - \gamma c_t - q\right)p_c + \alpha p_r^{\,2} \\ &\quad + \left(\beta - \alpha c_{s1} - \alpha c_{m1} - \alpha c_r\right)p_r + q\left(\lambda_1 c_{s1} + \lambda_2 c_{s1} + \lambda_1 c_{m1} - \lambda_2 c_{s2} - \lambda_1 c_{m2} - c_t\right) - \beta\left(c_{s1} + c_{m1} + c_r\right)\end{aligned} \tag{6}$$

To make the closed-loop supply chain system get the maximum total profit, it can be seen as the dual function of p_c and p_r, so the optimal condition of the first order can be addressed as following.

$$\begin{cases}\dfrac{\partial \pi^*}{\partial p_c} = -2\gamma p_c + \lambda_1\gamma\left(c_{s1} + c_{m1}\right) + \lambda_2\gamma(c_{s1} - c_{s2} - c_{m2}) - \gamma c_t - q = 0 \\ \dfrac{\partial \pi^*}{\partial p_r} = 2\alpha p_r + \left(\beta - \alpha c_{s1} - \alpha c_{m1} - \alpha c_r\right) = 0\end{cases} \tag{7}$$

Then the solution of Eq.(1), i.e. p_c^* and p_r^*, can be concluded as:

$$\begin{cases}p_c^* = \dfrac{\left(\lambda_1\gamma c_{s1} + \lambda_2\gamma c_{s1} + \lambda_1\gamma c_{m1} - \lambda_2\gamma c_{s2} - \lambda_2\gamma c_{m2} - \gamma c_t - q\right)}{2\gamma} \\ p_r^* = \dfrac{c_{s1} + c_{m1} + c_r}{2} - \dfrac{\beta}{2\alpha}\end{cases} \tag{8}$$

And, finally, the total profits of the closed-loop supply chain system in joint decision scenario can be noted as:

$$\begin{aligned}\pi^* = &\frac{\left(\lambda_1\gamma c_{s1} + \lambda_2\gamma c_{s1} + \lambda_1\gamma c_{m1} - \lambda_2\gamma c_{s2} - \lambda_2\gamma c_{m2} - \gamma c_t - q\right)^2}{4\gamma} - \frac{\left(\alpha c_{s1} + \alpha c_{m1} + \alpha c_r - \beta\right)^2}{4\alpha} \\ &+ b + q\left(\lambda_1 c_{s1} + \lambda_2 c_{s1} + \lambda_1 c_{m1} - \lambda_2 c_{s2} - \lambda_1 c_{m2} - c_t\right) - \beta\left(c_{s1} + c_{m1} + c_r\right)\end{aligned} \tag{9}$$

Independent Decision Scenario

In an independent decision-making situation, it is supposed that the automobile manufacturer acts as the leading factor, under the condition of complete information symmetry, after the automobile retailer and the third-party automobile recyclers have learnt the decision of the manufacturer, and then make their own pricing decisions of the retail price and the recycling price. As for the automobile retailer, to maximize its revenue, the optimal condition is:

$$\frac{\partial \pi_r}{\partial p_r} = 2\alpha p_r + \beta - \alpha c_r - \alpha w = 0 \tag{10}$$

As for third-party scrap car recycling, to maximize its revenue, the optimal condition is:

$$\frac{\partial \pi_t}{\partial p_c} = 2\left(\lambda_1\gamma\delta_1 + \lambda_2\gamma\delta_2 - \gamma\right)p_c + b + \left(\lambda_1 q\delta_1 + \lambda_2 q\delta_2 - \gamma c_t - q\right) = 0 \tag{11}$$

Then it can get the following results:

$$p_r^{**} = \frac{\alpha c_r + \alpha w - \beta}{2\alpha} \tag{12}$$

$$p_c^{**} = \frac{\gamma c_t + q - \lambda_1 q\delta_1 - \lambda_2 q\delta_2 - b}{2\left(\lambda_1\gamma\delta_1 + \lambda_2\gamma\delta_2 - \gamma\right)} \tag{13}$$

Eq.(13) means that with the given wholesale price w of the manufacturer, the retailer will set the wholesale prices as the p_c^{**} in Eq.(13), and can be seen as the reactions of the retailer to the manufacturer's wholesale price strategy, i.e. the retailer's reaction function.

Bring the Eq.(12) and Eq.(13) into Eq.(1), then the profit function of the automobile parts supplier, in the independent decision, can be obtained as:

$$\pi_s = \frac{\alpha}{2}w^2 + \left(\frac{\alpha c_r + \beta - q}{2} - \frac{\gamma c_t + b}{2(\lambda_1\delta_1 + \lambda_2\delta_2 - 1)}\right)u - \frac{\alpha c_{s1}}{2}w + B_2 \tag{14}$$

where $B_1 = \frac{1}{2}\left[c_{s1}(\lambda_1 + \lambda_2) - \lambda_1(\delta_2 p_c^* + c_{s2})\right]\left[q + \frac{\gamma c_t + b}{\lambda_1\delta_1 + \lambda_2\delta_2 - 1}\right]$, $B_2 = B_1 + \frac{1}{2}\left[\alpha w(u-w) - c_{s1}(\alpha c_r - \beta)\right]$.

Bring the Eq.(12) and Eq.(13) into Eq.(2), then the profit function of the automobile manufacturer, in the independent decision, can be obtained as:

$$\pi_m = \frac{\alpha}{2}w^2 + \frac{\alpha c_r + \beta - \alpha c_{m1}}{2}w - \frac{\alpha}{2}wu - \left(\frac{\alpha c_r + \beta - q\lambda_1}{2} - \frac{(\gamma c_t + b)\lambda_1}{2(\lambda_1\delta_1 + \lambda_2\delta_2 - 1)}\right)u + C_2 \tag{15}$$

where $C_1 = \frac{1}{2}\lambda_1\left(c_{m1} - c_{m2} - \delta_1 p_c^*\right)\left[q + \frac{\lambda c_t + b}{\lambda_1\delta_1 + \lambda_2\delta_2 - 1}\right]$, $C_2 = C_1 - \frac{1}{2}c_{m1}(\alpha c_r + \beta)$.

It is evident that the automobile parts supplier 's decision variable is the supplier's parts selling price u, the automobile manufacturer's decision variable is the wholesale price w. Therefore, for the automobile parts supplier's maximum profit, the optimal condition of first order can be addressed as following:

$$\begin{cases} \frac{\partial \pi_s}{\partial u} = \frac{\alpha}{2}w + \left(\frac{\alpha c_r + \beta - q}{2} - \frac{\gamma c_t + b}{2(\lambda_1\delta_1 + \lambda_2\delta_2 - 1)}\right) = 0 \\ \frac{\partial \pi_m}{\partial w} = \alpha w - \frac{\alpha c_r + \beta - \alpha c_{m1}}{2} - \frac{\alpha}{2}u = 0 \end{cases} \tag{16}$$

So get the following formula:

$$w^{**} = \frac{\gamma c_t + b}{\alpha(\lambda_1\delta_1 + \lambda_2\delta_2 - 1)} - \frac{\alpha c_r + \beta - q}{\alpha} \tag{17}$$

$$u^{**} = 2w - \frac{\alpha c_r + \beta - \alpha c_{m1}}{\alpha} \tag{18}$$

Eq.(18) represent that given the wholesale price of manufacturers, i.e. w^{**}, the supplier will set its optimal decision with the price of u^{**}. Then bring the Eq.(17) into Eq.(18), it can obtain the supplier and the manufacturer's optimal pricing in the independent decision-making, leading by manufacturer. That is:

$$\begin{cases} w^* = \frac{\gamma c_t + b}{\alpha(\lambda_1\delta_1 + \lambda_2\delta_2 - 1)} - \frac{\alpha c_r + \beta - q}{\alpha} \\ u^* = \frac{2\gamma c_t}{\alpha(\lambda_1\delta_1 + \lambda_2\delta_2 - 1)} - \frac{3\alpha c_r + 3\beta - 2q - \alpha c_{m1}}{\alpha} \end{cases} \tag{19}$$

Bring the Eq.(12) and Eq.(13) into Eq.(5) , it can obtain the system profit under the closed-loop supply chain, which is in the independent decision leaded by automotive manufacturers.

$$\pi^{**} = -\frac{\gamma}{4}\left[\frac{\gamma c_t + 2q(1 - \lambda_1\delta_1 - \lambda_2\delta_2) - p_b}{\gamma(\lambda_1\delta_1 + \lambda_2\delta_2 - 1)} - \lambda_1\Delta_2 - \lambda_2\Delta_1 - c_t\right]^2 + \alpha\left(\frac{c_r + w - \Delta_2 - c_r}{2}\right)^2 + b$$
$$+ \frac{\left[\lambda_1\gamma\Delta_2 + \lambda_2\gamma\Delta_1 - \gamma c_t - q\right]^2}{4\gamma} - \frac{(\alpha\Delta_2 + \alpha c_r - \beta)^2}{4\alpha} + q\lambda_1(\Delta_2 - c_{m2}) + q\lambda_2(c_{s1} - c_{s2}) - qc_t - \beta(\Delta_2 + c_r) \tag{20}$$

where $\Delta_1 = c_{s1} - c_{s2} - c_{m2}$, $\Delta_2 = c_{s1} + c_{m1}$.

Comparing the system profit of joint decision system and independent decision, i.e. Eq.(9) and Eq.(20), the following inequation can be obtained.

$$\pi^{*} > \pi^{**}$$

By the above comparison, it is evident that the system profit of the independent decision is lower than the profit of the joint decision system. And it is evident that there is no impact of the government subsidy for the third-party recycler on the relation of π^{*} and π^{*}, because the subsidy for the third-party recycler is not a function of the quantity of the ELV recycled from the automobile market, so this kind of subsidy has no effect on the coordination of the green supply chain coordination in ELV recycling system.

Conclusion

In this paper, the coordination of the green supply chain coordination in ELV recycling system with government subsidy for the third-party recycler is analyzed with the method of game theory and the related mathematical methods. Though the analysis of the independent decision scenario and the joint decision scenario, it is found that the total system profit is higher in the joint decision scenario than that in the independent decision scenario, and the subsidy strategy design in this paper has no effect on the coordination of the green supply chain coordination in ELV recycling system. Therefore, each enterprise in the closed-loop supply chain system should try their best to cooperate and work together, then set the price strategy together, and the government needs to design more effective strategy to involved in the coordination of green supply chain.

ACKNOWLEDGEMENT

This work is supported by the National Natural Science Foundation of China (71403245), the Key Foundation of Philosophy and Social Science of Zhejiang Province (14NDJC139YB), and the Zhejiang Provincial Natural Science Foundation of China (LQ12G01006).

REFERENCES

[1] China Automotive Technology and Research Center, China Association of Automobile Manufactures. *China Automotive Industry Yearbook*, 8 (2011).

[2] S. Shinichi, Y. Hideto, H. Jiro, et al., An international comparative study of end-of-life vehicle (ELV) recycling systems, *Journal of Material Cycles & Waste Management* **16**, 1 (2014).

[3] Y. Kun, Comparative analysis of scrap car recycling management policies. *Procedia Environmental Sciences* **16**, 44-50(2012).

[4] K. Devika, B. L. Ana and J. C. Charbel, Selecting green suppliers based on GSCM practices: Using fuzzy TOPSIS applied to a Brazilian electronics company, *European Journal of Operational Research* **233**, 432 (2014).

[5] M. Sreekanth and F. L. Herbert, Energy technology allocation for distributed energy resources: a strategic technology-policy framework, *Energy* **72**, 783 (2014).

[6] X. Xu and A. Ruan, The Construction of Shapley Value in Cooperative Game and its Application on Enterprise Alliance, *Physics Procedia* **24**, 1377 (2012).

[7] X. Dai and L. Cheng, The effect of public subsidies on corporate R&D investment: an application of the generalized propensity score. *Technological Forecasting & Social Change* **90**, 419 (2015).

Crystalline Phase and Size-controlled Synthesis of Nickel Phosphide Nanocrystals

Yuan Pan, Yunqi Liu*

State Key Laboratory of Heavy Oil Processing, Key Laboratory of Catalysis, China University of Petroleum, 66 West Road, Qingdao, Shandong 266580, P. R. China

panyuan6690366@126.com; *linypy@126.com

Abstract

Nanostructured nickel phosphides were synthesized via a thermal decomposition approach. The effect of synthetic conditions such as P:Ni precursor mole ratio, reaction temperature, reaction time, reductant oleylamine quantity and species of additive on the crystalline phase and size of the as-synthesized nickel phosphides was discussed systematically. The results show that lower P:Ni precursor mole ratio, higher reaction temperature, shorter reaction time and the addition of oleic acid were beneficial to form Ni12P5 phase with large size. In contrast, higher P:Ni precursor mole ratio, lower reaction temperature, longer reaction time and the addition of octadecene were beneficial to form Ni2P phase with small size. The variety of oleylamine quantity cannot realize the phase-controlled synthesis, but the size can be controlled. These synthetic method also can be used to synthesize others transition metal phosphides.

Keywords

Initials in Capitals; Separate with Semicolons

Introduction

The controllable synthesis of transition metal phosphides has been regarded as a hot topic because their many properties are connected with different nanostructures, such as crystalline phase, size and morphology[1], especially nanostructured nickel phosphides, which have more comprehensive application in catalysis field[2]. For example, Li et al.[3] synthesized and compared electrocatalytic activity of Ni_2P nanorods and nanoparticles. Ni et al.[4] synthesized nickel phosphide nanocrystals (NCs) with two different phase (Ni_2P and $Ni_{12}P_5$) and compared their photocatalytic degradation ability. Layan Savithra et al.[5] reported the size-dependent catalytic activity of Ni_2P NCs for hydrodesulfurization (HDS). Therefore, it is necessary to synthesize nanostructured nickel phosphides with different phase, size and morphology. However, trioctylphosphine (TOP) often used as phosphorus source to synthesize nickel phosphides in published reports, the large scale application is limited due to the high price.

In this work, we report the controllable synthesis of nickel phosphides by using low-cost triphenylphosphine (TPP) as phosphorus source. The influence of reaction conditions including P:Ni precursor mole ratio, reaction temperature, reaction time, reductant oleylamine (OAm) quantity and species of additive on phase and size of nickel phosphides were investigated systematically. These synthetic method also can be used to synthesize others transition metal phosphides. By comparing our results with already published reports, in our study, not only the TPP with low cost was used as P source, but also the controllable synthesis can be achieved easily.

Expeimental

Synthesis of Nickel Phosphide Nanocrystals

In a typical synthesis, $Ni(acac)_2$ (0.256 g, 1 mmol), OAm (5-20 mL, 15.2-60.8 mmol) and TPP (0.5-4 g) were placed in a flask and stirred magnetically under a flow of argon. The mixture was raised to 280-340^{o}C by a heating jacket and kept at this temperature for 10-120 min. After cooling down to room temperature, the product was collected, centrifuged, washed with a mixture of hexane and ethanol, and finally dried in vacuum at 60^{o}C for 24 h. The crystalline phase and size of nickel phosphides can be controlled by changing reaction condition, including P:Ni

2226-4523/16/01 072-5 © 2016 DEStech Publications, Inc.
doi:10.12783/ijmsci.2016.0601.08

precursor mole ratio, reaction temperature, reaction time, reductant OAm quantity and species of additive.

Characterization

X-ray diffraction (XRD) was carried out on a Rigaku D/max-IIA diffractometer with Cu Kα radiation at 45 kV and 40 mA. Transmission electron microscopy (TEM) was conducted on a JEM-2100 UHR microscope (JEOL, Japan) performed at 200 kV.

Results and Discussion

In our reaction system, $Ni(acac)_2$ as Ni source, TPP as P source and OAm as reductant, the nickel phosphide NPs can be synthesized by thermal decomposition of the above mixed solution under Ar. By changing the reaction conditions, including the P:Ni precursor mole ratio, reaction temperature and time, reductant OAm quantity and the addition of different additive, different crystalline phase and size of nickel phosphides were obtained easily. Therefore, we tried a variety of single factor experiments, as shown in Table 1. The obtained products were characterized by XRD and TEM.

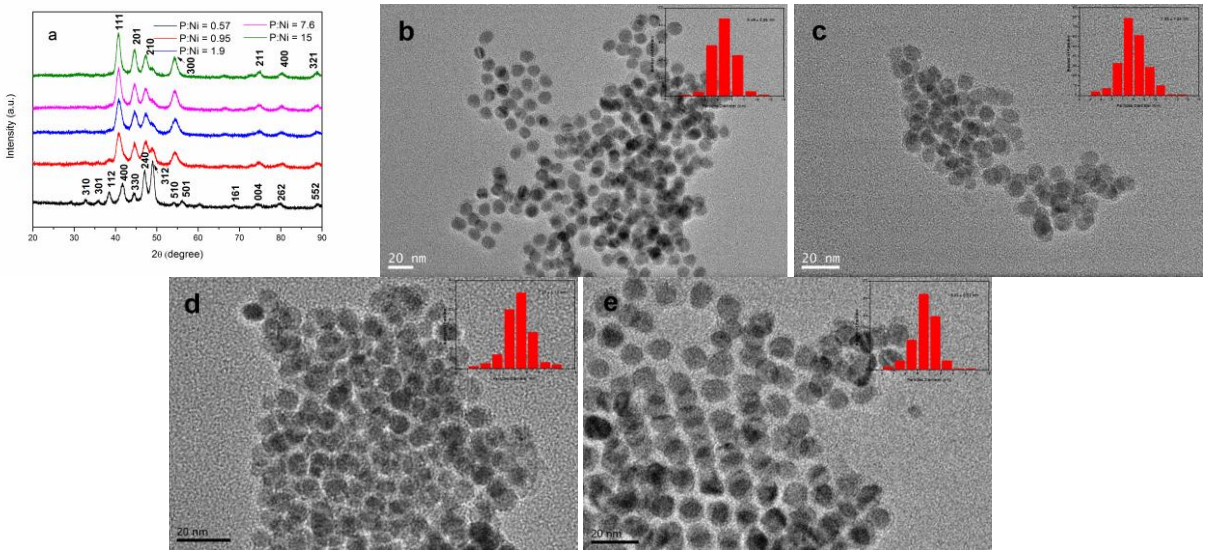

FIGURE 1. XRD PATTERNS (a) AND TEM IMAGES OF THE PRODUCT AT DIFFERENT P:Ni PRECURSOR MOLE RATIO FOR (b) P:Ni = 0.57 (c) P:Ni = 0.95 (d) P:Ni = 7.6 (e) P:Ni = 15.

The XRD pattern and TEM images of the as-synthesized product at different P:Ni precursor mole ratio (from 0.57 to 15) are shown in Fig. 1. We found that an interesting phenomenon occurs. The crystalline phase of the product was changed with the increase of P:Ni precursor mole ratio (Fig. 1a). When the ratio was 0.57, the product was pure $Ni_{12}P_5$ (PDF # 03-065-1623). The peaks at 32.8 °, 35.7 °, 38.4 °, 41.7 °, 44.4 °, 46.9 °, 49 °, 53.9 °, 56.1 °, 68.9 °, 74.2 °, 79.8 ° and 88.7 ° can be attributed to the (310), (301), (112), (400), (330), (240), (312), (510), (501), (161), (004), (262) and (552) crystalline faces. TEM image indicates the as-synthesized $Ni_{12}P_5$ exhibits solid spherical nanoparticles morphology (Fig. 1b). The size distribution histogram indicates the average size of nanoparticles was 9.49 ± 0.86 nm (inset in Fig. 1b). Increasing the ratio led to the variation of crystalline phase. When the ratio was increased to 0.95, the product was the mixture phase of Ni_2P (major) and $Ni_{12}P_5$ (minor). The peaks at 38.6 ° and 49 ° belong to the (112) and (312) crystalline face of $Ni_{12}P_5$. Similarly, TEM image also displays the solid spherical morphology (Fig. 1c), but the size was decreased to 7.95 ± 1.24 nm (inset in Fig. 1c). Further increasing the ratio to 1.9, the peak at 38.6° disappeared, and the peak intensity of 49° was weakened. Until the ratio was 7.6, the product was pure Ni_2P (PDF # 03-065-3544). The peaks at 40.8 °, 44.5 °, 47.4 °, 54.3 °, 75.1 °, 80.2 ° and 88.9 ° can be assigned to the (111), (201), (210), (300), (211), (400) and (321) crystalline faces. The average size of Ni_2P NPs was 7.27 ± 1.13 nm at this point (inset in Fig. 1d). When we further change the ratio to 15, the phase was not changed, but the average size was decreased to 6.63 ± 0.98 nm (inset in Fig. 1e). This is due to TPP not only acted as a P source, but also a surfactant, which can adsorb on the surface of NPs and restrain the growth and aggregation of NPs.

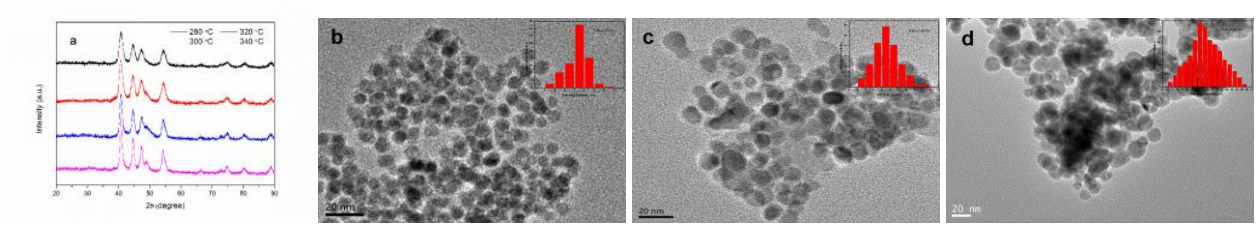

FIGURE 2. XRD PATTERNS (a) AND TEM IMAGE AT DIFFERENT TEMPERATURE OF (b) 280°C (c) 320°C (d) 340°C.

TABLE 1 DETAILED SYNTHETIC CONDITIONS OF THE SINGLE-FACTOR EXPERIMENT

	P: Ni	T/℃	t/min	OAm/mL	Additive	Product
A	0.57	300	120	5	-	$Ni_{12}P_5$
	0.95	300	120	5	-	$Ni_{12}P_5$+Ni_2P
	1.9	300	120	5	-	$Ni_{12}P_5$+Ni_2P
	7.6	300	120	5	-	Ni_2P
	15	300	120	5	-	Ni_2P
B	7.6	280	120	5	-	Ni_2P
	7.6	300	120	5	-	Ni_2P
	7.6	320	120	5	-	$Ni_{12}P_5$+NiP
	7.6	340	120	5	-	$Ni_{12}P_5$+NiP
C	7.6	300	10	5	-	$Ni_{12}P_5$+NiP
	7.6	300	30	5	-	$Ni_{12}P_5$+NiP
	7.6	300	60	5	-	$Ni_{12}P_5$+NiP
D	7.6	300	300	5	-	Ni_2P
	7.6	300	120	5	-	Ni_2P
	7.6	300	120	10	-	Ni_2P
	7.6	300	120	20	-	Ni_2P
E	7.6	300	120	5	OA	$Ni_{12}P_5$
	7.6	300	120	5	ODE	Ni_2P

We further study the effect of reaction temperature from 280 to 340°C, the corresponding XRD and TEM results were shown in Fig. 2. From Fig. 2a, it can be concluded that the crystalline phase is pure Ni_2P at the low temperature (≤300 °C). When further increasing the temperature, a weak peak appeared at 49 °, which can be assigned to the (312) crystalline face of $Ni_{12}P_5$. This reason can be attributed to the loss of P source at high temperature. TEM images (Fig. 2b-d) display that the as-obtained NPs were monodisperse at low temperature. When the temperature was 340°C, the NPs were agglomerate. In addition, the size distribution histogram also indicates that the size can be controlled from 6.36 ± 1.01 nm to 17.6 ± 3.28 nm.

Generally, the reaction time was used to study the growth mechanism of nanocrystal. But in our experimental process, we found that the time was also a key factor to influence the crystalline phase of the product. Fig. 3a shows the XRD patterns of the product at different time. The product was the mixture of Ni_2P and $Ni_{12}P_5$ at low reaction time, and the pure Ni_2P can be obtained until the reaction time reached 2 h, which indicates that longer reaction time was beneficial to the phosphorization process, thus, Ni_2P phase was formed. However, TEM images (Fig. 3b) and size distribution (inset in Fig. 3b-d) show that the average size of NPs nearly no changed, which indicates that the size of NPs could not be controlled by changing reaction time. However, we also can be found that the dispersity of nickel phosphide NPs was poor with the increase of reaction time.

Because the reductant can influence the nucleation rate of nanocluster, therefore, we tried to control this reaction by changing the reductant quantity. From the XRD patterns (Fig. 4a), it can be seen that the variation of OAm quantity cannot change the phase of the product. All the products at different OAm quantity were Ni_2P phase, which suggests that the phase cannot be controlled by changing the OAm quantity. TEM results (Fig. 4b-c) suggest that the size of the Ni_2P NPs decreased from 8.03 ± 1.08 to 6.91 ± 0.86 nm with the increase of OAm quantity from 10 to 20 mL. The excess OAm in reaction system was beneficial to the nucleation process, and limited the aggregation of Ni_2P NPs. However, because of the strong intermolecular forces and high surface energy of nanoparticles in solution, the Ni_2P NPs were aggregated at low OAm quantity, the large size NPs obtained.

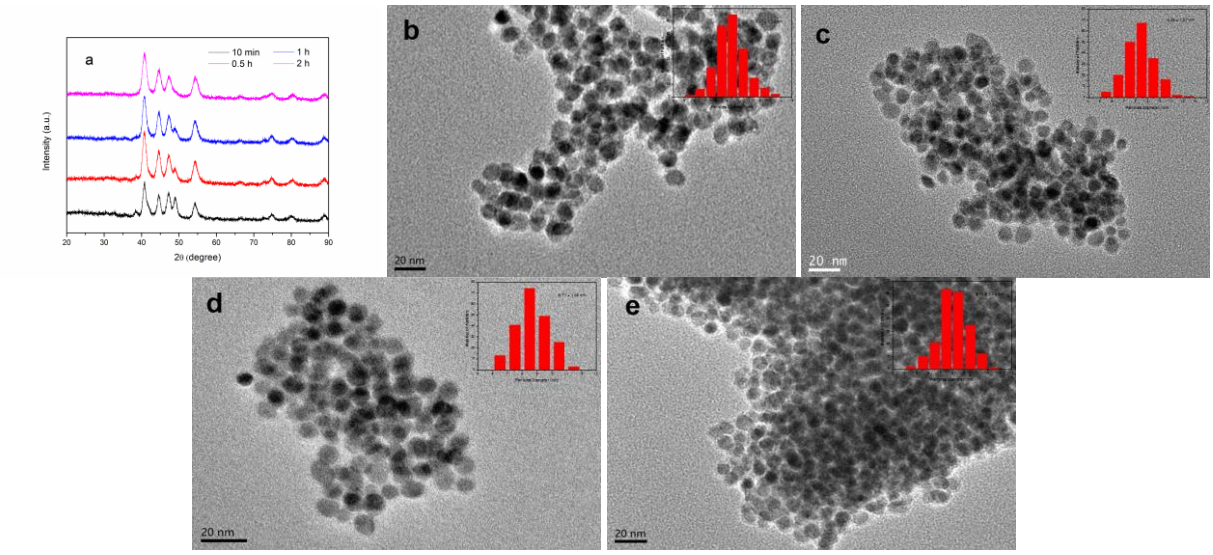

FIGURE 3. XRD PATTERNS (a) AND TEM IMAGES OF THE AS-SYNTHESIZED PRODUCT AT DIFFERENT REACTION TIME FOR (b) t= 10 min (c) t = 30 min (d) t= 60 min (e) t=300 min.

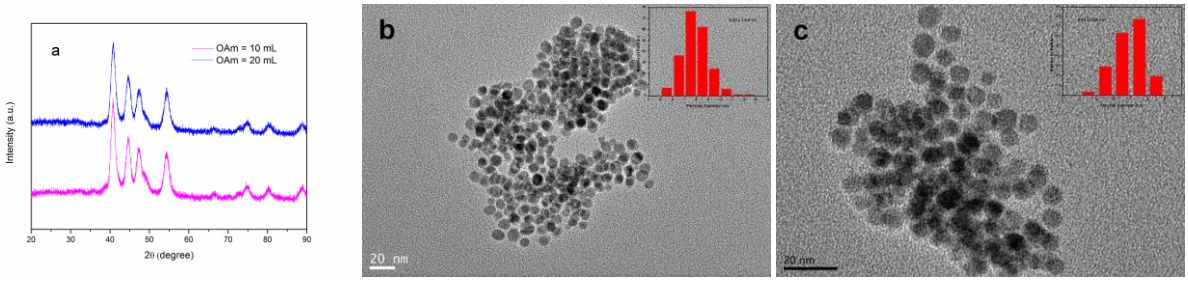

FIGURE 4. XRD PATTERNS (a) AND TEM IMAGES AT DIFFERENT OAm QUANTITY FOR (b) 10 mL (c) 20 mL.

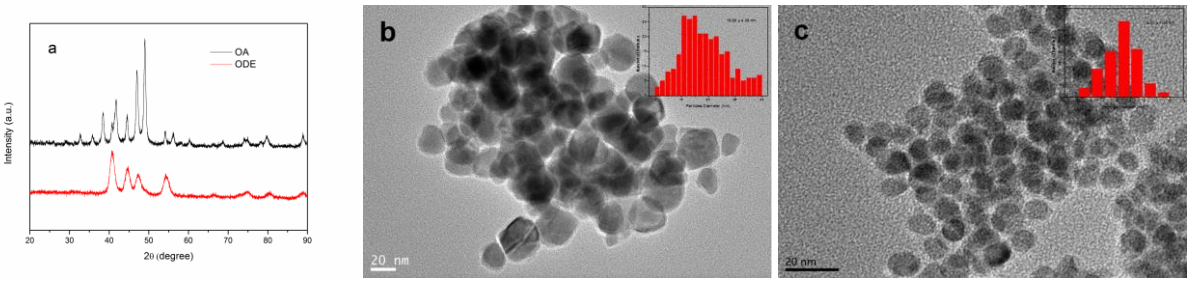

FIGURE 5. XRD PATTERNS (a) AND TEM IMAGES AT DIFFERENT SPECIES OF ADDITIVE FOR (b) OA (c) ODE.

We further study the effect of the species of additive. Fig. 5a shows the XRD patterns of the product at different additive, including oleic acid (OA) and octadecene (ODE). It can be easily found that the crystalline phase was changed. When the additive was OA, the product was $Ni_{12}P_5$, which also exhibits solid sphere-like morphology but with large average size of 19.28 ± 4.36 nm (Fig. 5b). When the additive was replaced using ODE, the product was Ni_2P, which exhibits small average size NPs of 8.27 ± 1.26 nm. Results suggest that OA was not beneficial to the phosphorization of TPP.

Conclusions

In summary, lower P:Ni precursor mole ratio, higher reaction temperature, shorter reaction time and the addition of OA were beneficial to form $Ni_{12}P_5$ phase with large size. In contrast, higher P:Ni precursor mole ratio, lower reaction temperature, longer reaction time and the addition of ODE were beneficial to form Ni_2P phase with small size. However, the variety of OAm quantity cannot realize the phase-controlled synthesis, the product of each variety was Ni_2P phase, but the size can be controlled. The small size NPs can be obtained at lower OAm quantity. These synthetic method also can be expanded to synthesize others transition metal phosphides.

REFERENCES

[1] Yuan Pan, Wenhui Hu, Dapeng Liu, Yunqi Liu, Chenguang Liu. "Carbon nanotube decorated with nickel phosphide nanoparticles as efficient nanohybrid electrocatalyst for hydrogen evolution." Journal of Materials Chemistry A 3 (2015): 13087-13094.

[2] Ara Cho, Hosoo Kim, Ayako Iino, Atsushi Takagaki, S. Ted Oyama. "Kinetic studies of hydrodeoxygenation of 2-methyltetrahydrofuran on a Ni_2P/SiO_2 catalyst at medium pressure." Journal of Catalysis 311 (2014) 17-27.

[3] Hua Li, Wenzhong Wang, Zhaoyuan Gong, Yanmin Yu, lijin Piao, Huiying Chen, Jianxin Xia. "Shape-controlled synthesis of nickel phosphide nanocrystals and their application as hydrogen evolution reaction catalyst." Journal of Physics and Chemistry of Solids 80 (2015) 22-25.

[4] Yonghong Ni, Lina Jin, Jianming Hong. "Phase-controllable synthesis of nanosized nickel phosphides and comparison of photocatalytic degradation ability." Nanoscale 3 (2011) 196-200.

[5] Galbokka H. Layan Savithra, Elayaraja Muthuswamy, Richard H. Bowker, Bo A. Carrillo, Mark E. Bussell, and Stephanie L. Brock. "Rational design of nickel phosphide hydrodesulfurization catalysts: controlling particle size and preventing sintering."Chemistry of Materials 25 (2013) 825-833.

Yuan Pan is currently a Ph.D. candidate at China University of Petroleum (UPC). His currently scientific interests focus on controlled synthesis and catalytic applications of nanocatalysts.

Prof. Yunqi Liu is currently associate director of State Key Laboratory of Heavy Oil Processing in China University of Petroleum (UPC). He received his Ph.D. in Applied Chemistry at CUP in 2000. His research interests focus on the development of heterogeneous catalysts for petroleum refining and the design of novel catalysis materials. He has been in charge of and taken part in several relevant projects (e.g. *the National Natural Science Foundation of China, 973 programs of China and the Science and Technology Development Project of CNPC*). He has published over 150 papers in peer-reviewed journals (e.g. *J. Mater. Chem. A, J. Power Sources, Fuel, Energy & Fuel, Appl. Catal. A: Gen., Micropor. Mesopor. Mat.*) and applied over 22 patents.